

|   |  |   |   |
|---|--|---|---|
| <p>The EUMETSAT<br/>Network of<br/>Satellite Application<br/>Facilities</p> |  <p><b>NWP SAF</b><br/>Numerical Weather Prediction</p> | <p>RTTOV-12 Science and<br/>Validation Report</p> | <p>Doc ID : NWPSAF-MO-TV-41<br/>Version : 1.0<br/>Date : 16/02/2017</p> |
|---|--|---|---|

# RTTOV-12

## SCIENCE AND VALIDATION REPORT

***Roger Saunders<sup>1</sup>, James Hocking<sup>1</sup>, David Rundle<sup>1</sup>, Peter Rayer<sup>1</sup>,  
Stephan Havemann<sup>1</sup>, Marco Matricardi<sup>2</sup>, Alan Geer<sup>2</sup>,  
Cristina Lupu<sup>2</sup>, Pascal Brunel<sup>3</sup>, Jérôme Vidot<sup>3</sup>***

**Affiliations:**

**<sup>1</sup>Met Office, U.K.**

**<sup>2</sup>European Centre for Medium Range Weather Forecasts**

**<sup>3</sup>MétéoFrance**

This documentation was developed within the context of the EUMETSAT Satellite Application Facility on Numerical Weather Prediction (NWP SAF), under the Cooperation Agreement dated 1 December, 2006, between EUMETSAT and the Met Office, UK, by one or more partners within the NWP SAF. The partners in the NWP SAF are the Met Office, ECMWF, KNMI and Météo France.

Copyright 2017, EUMETSAT, All Rights Reserved.

| Change record |            |                     |  |
|---------------|------------|---------------------|--|
| Version       | Date       | Author / changed by | Remarks  |
| 0.1           | 17/06/2016 | R W Saunders        | First draft version requesting input from developers |
| 0.3           |            | R W Saunders        | First complete draft for comment                     |
| 0.4           | 06/02/17   | R W Saunders        | Draft for comment                                    |
| 1.0           | 16/02/17   | R W Saunders        | Final version for release                            |

## Table of contents

|   |          |
|---|----------|
| <b>TABLE OF CONTENTS .....</b>  | <b>2</b> |
| <b>1. INTRODUCTION .....</b>  | <b>4</b> |
| <b>2. SCIENTIFIC CHANGES FROM RTTOV-11 TO RTTOV-12 .....</b>                  | <b>5</b> |
| 2.1 REFINEMENTS IN THE LINE-BY-LINE TRANSMITTANCE DATABASES AND MODELS.....   | 6        |
| 2.1.1 Use of new profile datasets.....  | 6        |
| 2.1.2 Updates to Visible and Infrared Line by Line Models and HITRAN.....     | 10       |
| 2.1.3 Microwave Line by Line Model.....                                       | 13       |
| 2.2 ADDITION OF SO <sub>2</sub> AS A VARIABLE GAS .....                       | 16       |
| 2.3 SPECIFICATION OF CLOUD/AEROSOL UNITS .....                                | 18       |
| 2.4 DISCRETE ORDINATES SCATTERING.....  | 20       |
| 2.5 ICE CLOUD SCATTERING .....  | 23       |
| 2.6 INFRARED SURFACE EMISSIVITY .....   | 26       |
| 2.6.1 Over ocean .....  | 26       |
| 2.6.2 Improved treatment of sea surface reflectance for solar radiation ..... | 32       |
| 2.6.3 Updated land surface atlas .....  | 34       |
| 2.7 MICROWAVE OCEAN AND LAND SURFACE EMISSIVITY.....                          | 38       |
| 2.7.1 FASTEM-6 update .....   | 38       |
| 2.7.2 TESSEM2 .....   | 41       |
| 2.7.3 TELSEM2.....  | 42       |
| 2.7.4 CNRM Atlas .....  | 44       |
| 2.8 PC-RTTOV UPDATES .....  | 45       |

|           |  |           |
|-----------|--|-----------|
| 2.9       | ADDITION OF HT-FRTC .....  | 45        |
| 2.10      | UPDATED NON-LTE FORMULATION.....   | 47        |
| 2.11      | COEFFICIENTS FOR ZEEMAN-AFFECTED CHANNELS .....  | 52        |
| 2.12      | COEFFICIENTS FOR THE PMR PRESSURE MODULATOR RADIOMETER.....                                  | 54        |
| 2.13      | ADDITIONAL CHANGES TO INTERNAL CALCULATIONS WHICH AFFECT RTTOV<br>RADIANCE CALCULATIONS..... | 56        |
| 2.14      | OTHER CHANGES TO RTTOV BEHAVIOUR WHICH AFFECTS OUTPUTS .....                                 | 57        |
| <b>3.</b> | <b>TESTING AND VALIDATION OF RTTOV-12.....</b>   | <b>58</b> |
| 3.1       | VALIDATION OF TOP OF ATMOSPHERE RADIANCES.....   | 58        |
| 3.1.1     | Comparison of simulations.....   | 58        |
| 3.1.2     | Comparison with observations .....   | 64        |
| 3.2       | COMPARISON OF JACOBIANS .....  | 70        |
| <b>4.</b> | <b>SUMMARY .....</b>   | <b>71</b> |
| <b>5.</b> | <b>ACKNOWLEDGEMENTS.....</b>   | <b>73</b> |
| <b>6.</b> | <b>REFERENCES .....</b>  | <b>74</b> |

|   |   |   |   |
|---|---|---|---|
| <p>The EUMETSAT<br/>Network of<br/>Satellite Application<br/>Facilities</p> |  | <p>RTTOV-12 Science and<br/>Validation Report</p> | <p>Doc ID : NWPSAF-MO-TV-41<br/>Version : 1.0<br/>Date : 16/02/2017</p> |
|---|---|---|---|

## 1. Introduction

The purpose of this report is to document the scientific aspects of the latest version of the NWP SAF fast radiative transfer model, referred to hereafter as RTTOV-12, which are different from the previous model RTTOV-11 and present the results of the validation tests comparing the two versions of RTTOV which have been carried out. The enhancements to this version, released in Feb 2017, have been made under the auspices of the EUMETSAT [NWP-SAF](#).

The RTTOV-12 software is available at no charge to users on request from the new NWP SAF [web site](#). Note the licence agreement first has to be completed on the web site by clicking on 'Software Downloads' and 'Software Preferences'. RTTOV-12 documentation, including the latest version of this document can be viewed on the NWP SAF web site at: <http://nwpsaf.eu/site/software/rttov/documentation/> which may be updated from time to time. Technical documentation about the software and how to run it can be found in the RTTOV-12 user's guide which can also be downloaded from the link above and is provided as part of the distribution file to users.

The baseline document for the original version of RTTOV is available from ECWMF as Eyre (1991) and the basis of the original model is described in Eyre and Woolf (1988). This was updated for RTTOV-5 (Saunders *et. al.* 1999a, Saunders *et. al.*, 1999b) and for RTTOV-6, RTTOV-7, RTTOV-8, RTTOV-9 (Matricardi *et. al.*, 2004), RTTOV-10 and RTTOV-11 with the respective science and validation reports for each version hereafter referred to as R7REP2002, R8REP2006, R9REP2008, R10REP2010 and R11REP2013, respectively all available from the NWP SAF web site at the link above and the links to the individual reports are given in the references section of this report. The changes described here only relate to the scientific differences from RTTOV-11. A complete list of scientific and technical differences between RTTOV-11 and -12 is given in section 4 of the RTTOV-12 user guide.

This document also describes comparisons and validations of the output values from this new version of the model by comparing with previous versions, other models and observations. In general only aspects related to new and improved science are presented in this report but some results are presented of the overall performance of the new RTTOV package. Many of the details of the new science are given in other papers/reports which are referenced in this document and so only a summary is presented here in order to keep this document manageable in size. Section 2 describes the individual scientific changes in RTTOV-12 and the changes they make to simulations. Section 3 describes the overall performance of the new model for a limited number of satellite radiometers. Section 4 gives a brief summary.

|   |   |   |   |
|---|---|---|---|
| <p>The EUMETSAT<br/>Network of<br/>Satellite Application<br/>Facilities</p> |  | <p>RTTOV-12 Science and<br/>Validation Report</p> | <p>Doc ID : NWPSAF-MO-TV-41<br/>Version : 1.0<br/>Date : 16/02/2017</p> |
|---|---|---|---|

## 2. Scientific Changes from RTTOV-11 to RTTOV-12

The main scientific changes from RTTOV-11 to RTTOV-12 are listed here:

- Improvements to infrared and microwave line-by-line models and associated spectroscopic datasets from which the RTTOV coefficients are computed
- Inclusion of a new more accurate discrete ordinates scattering option for visible/near-infrared and infrared wavelengths
- Improvements to ice cloud scattering
- New infrared surface emissivity model over the ocean and updated atlas over land
- New microwave surface emissivity model over ocean and updated atlases over land. The TELSEM2 atlas now includes snow and sea-ice and extends the frequency range to 700GHz.
- Addition of SO<sub>2</sub> as a new variable gas
- Allow user to specify cloud/aerosol concentration units for input
- Improved model for non-LTE effects for advanced IR sounders
- Improved treatment of Zeeman effect for high peaking SSMIS channels
- Capability to simulate the pressure modulator radiometer
- Updates to the PC-RTTOV model
- Addition of capability to call the HT-FRTC model
- Other minor changes which affect the computed radiances

Each sub-section below gives more details on each of these components and references as required for all the details.

|   |   |   |   |
|---|---|---|---|
| <p>The EUMETSAT<br/>Network of<br/>Satellite Application<br/>Facilities</p> |  | <p>RTTOV-12 Science and<br/>Validation Report</p> | <p>Doc ID : NWPSAF-MO-TV-41<br/>Version : 1.0<br/>Date : 16/02/2017</p> |
|---|---|---|---|

## 2.1 Refinements in the Line-by-Line transmittance databases and models

### 2.1.1 Use of new profile datasets

The training set of atmospheric profiles for the previous RTTOV version was based on the work by Matricardi (2008) for AIRS and IASI noting the IASI coefficient file has now been trained with a more recent data-set.

The first sounders of the meteorological satellite era appeared in the 1970's with instruments such as VTPR and IRIS on board NOAA and NIMBUS satellites. RTTOV should be able to simulate radiances with the gas concentrations that were valid at that time. In the 2008 profile data-set the gas concentrations for CO<sub>2</sub>, N<sub>2</sub>O, CO and CH<sub>4</sub> were not diverse enough to cover the 1970's and 1980's. The new profile set described here has been constructed to cover the variability observed since the 1970's taking into account the fact that the mean profile should be also representative of the current state of the atmosphere.

SO<sub>2</sub> has been introduced as a new variable gas for simulating volcanic gas affected radiances. The pressure and temperature levels as well as the water vapour and ozone concentrations have not been modified.

#### Fixed gases

The line-by-line simulations are performed with some minor constituents that do not vary with profiles; these are named "fixed gases". The number of fixed gases has been increased in RTTOV-12. The new list of fixed gases are NH<sub>3</sub>, OH, HF, HCl, HBr, HI, ClO, H<sub>2</sub>CO, HOCl, HCN, CH<sub>3</sub>Cl, H<sub>2</sub>O<sub>2</sub>, C<sub>2</sub>H<sub>2</sub>, C<sub>2</sub>H<sub>6</sub>, and PH<sub>3</sub>. The profile concentrations are from the US76 standard atmosphere (US Standard Atmosphere, 1976) and shown in figure 1. The other fixed gases are O<sub>2</sub>, NO, NO<sub>2</sub>, SO<sub>2</sub> (see below), HNO<sub>3</sub>, OCS and N<sub>2</sub>. They are the same as in the 2008 profile data-set.

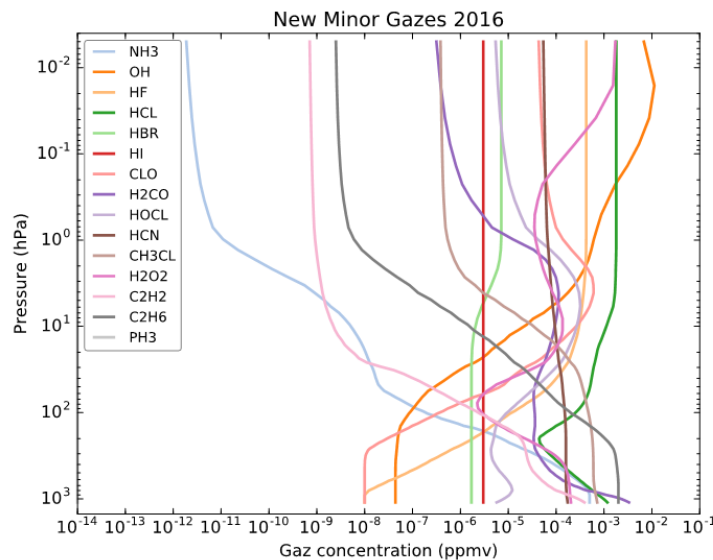


Figure 1: New fixed gas concentrations in ppmv over dry air for 2016 profile data-set.

Depending on the RTTOV predictor set used, the CO<sub>2</sub>, N<sub>2</sub>O, CO, CH<sub>4</sub> and SO<sub>2</sub> could be fixed for the training:

- Predictors v7: H<sub>2</sub>O and O<sub>3</sub> variable, all other gases fixed
- Predictors v8: predictors v7 + CO<sub>2</sub> variable
- Predictors v9: predictors v8 + N<sub>2</sub>O, CO, CH<sub>4</sub>, SO<sub>2</sub> variables (note that predictors v9 could be used with CO<sub>2</sub>, N<sub>2</sub>O, CO, CH<sub>4</sub>, SO<sub>2</sub> as fixed gases)

When those gases are considered as fixed, the profile is the mean of the variable dataset except for SO<sub>2</sub> where a “clean” background profile is used. It is worth mentioning that for v12 all IR coefficients (except SSU and PMR) are now available for both v7 and v8 predictors (previously only a small selection of v8 predictor coefficients were created). The main reason is that users may want to modify the CO<sub>2</sub> profile, particularly for older sensors since the background values are contemporary.

All v9 predictor visible+IR non-high resolution sounder coefficients have variable O<sub>3</sub>+CO<sub>2</sub> (instead of O<sub>3</sub>-only). This is for the same reason as above. The RTTOV vs LBL statistics were neutral or better in all channels across all sensors for the O<sub>3</sub>+CO<sub>2</sub> files vs the O<sub>3</sub>-only files. The only exception is SEVIRI ch04 which is degraded so there are also O<sub>3</sub>-only SEVIRI coefficients in the package.

#### The 2016 CO<sub>2</sub> profile dataset

The 2008 profile dataset for CO<sub>2</sub> is considered as valid for its variability within its respective limits. The method used for stretching these profiles is described in Matricardi and MacNally (2014). The stretching coefficients are 0.22 and -0.10 for CO<sub>2</sub> which gives a

minimum value of 335 ppmv, maximum of 486 ppmv and a mean of 401 ppmv. Figure 2 shows the 2016 CO<sub>2</sub> profiles dataset where the minimum and maximum profiles concentration are in blue and the mean CO<sub>2</sub> profile is in black. The 2008 minimum, maximum and mean CO<sub>2</sub> profiles are plotted in dashed lines.

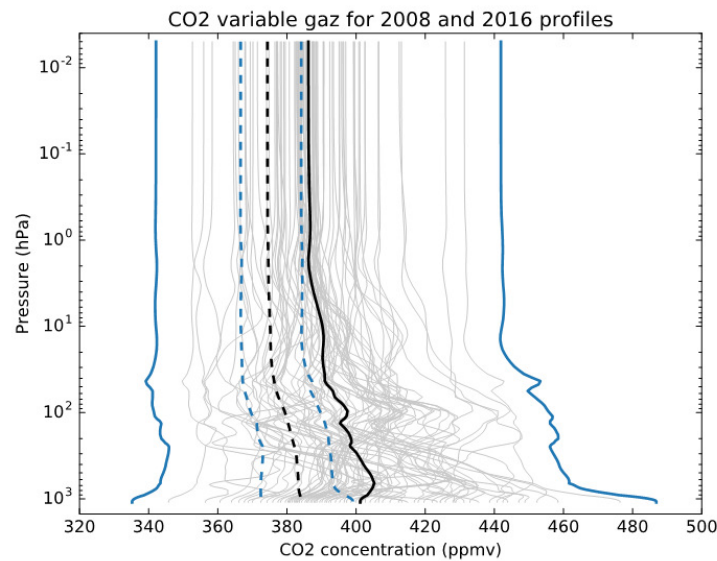


Figure 2: The 83 concentration profiles for CO<sub>2</sub> in the 2016 profiles dataset, average profile (83) in black continuous line, minimum (profile 81) and maximum (profile 82) envelopes in blue. The corresponding average and envelope for 2008 data-set are in dashed lines. Units are ppmv over dry air.

#### The 2016 N<sub>2</sub>O and CH<sub>4</sub> profiles data-set

The method for stretching the N<sub>2</sub>O and CH<sub>4</sub> concentration profiles is simpler than for CO<sub>2</sub> and is described in Matricardi and McNally (2014) for gases other than CO<sub>2</sub>. One starts to calculate the minimum and maximum profiles by applying an offset to the 2008 min/max profiles; then for all other profiles keep the ratio between the old min/max and apply to the new min/max. The old maximum has been increased by 8% for N<sub>2</sub>O and 18% for CH<sub>4</sub>. The old minimum has been decreased by 4% for N<sub>2</sub>O and 8% for CH<sub>4</sub>. New mean values at the lower level are 0.3298 ppmv for N<sub>2</sub>O and 1.852 ppmv for CH<sub>4</sub>. Figures 3 and 4 show a similar picture to Figure 2 but for N<sub>2</sub>O and CH<sub>4</sub>, respectively.

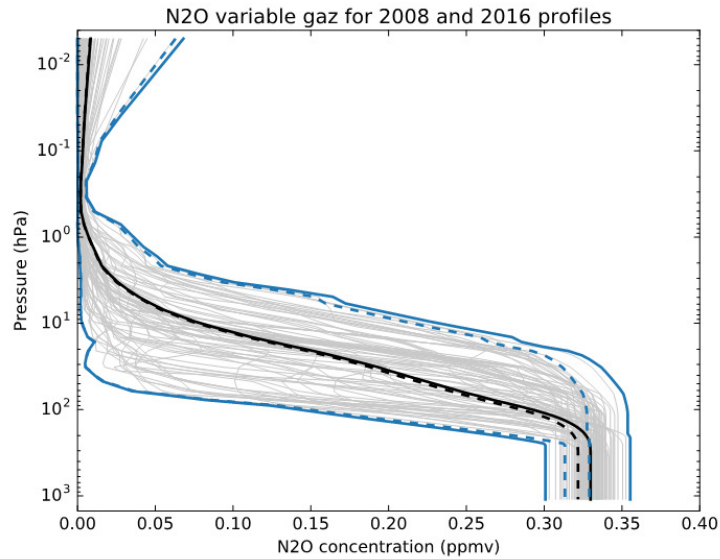


Figure 3: As figure 2 for  $N_2O$ .

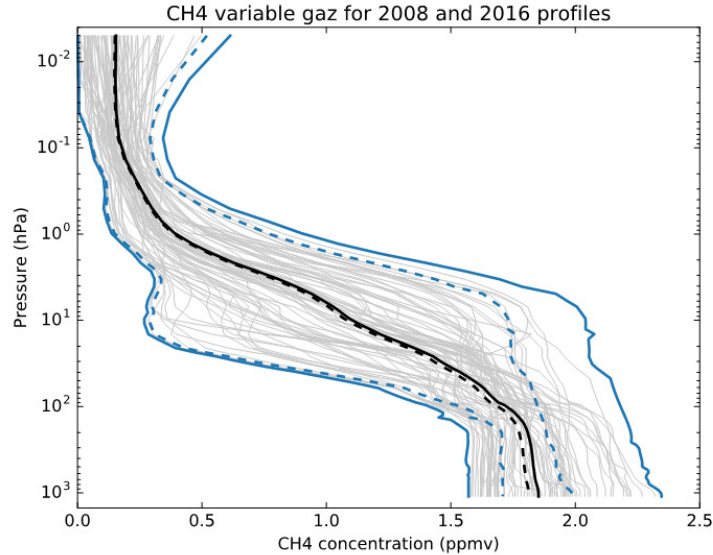


Figure 4: As figure 2 for  $CH_4$ .

### The 2016 $SO_2$ profiles data-set

To enable RTTOV simulations for variable  $SO_2$  (i.e. from a volcanic eruption) it was necessary to build a training profile dataset for this new gas in RTTOV. It has been chosen to create 59 volcanic  $SO_2$  synthetic profiles with different  $SO_2$  plumes in intensity and altitude. The dataset is completed with 29 profiles for normal background  $SO_2$ . Figure 5

shows the 2016 SO<sub>2</sub> profiles dataset where the full black lines represent the mean volcanic SO<sub>2</sub> profile and the dashed black lines the mean background SO<sub>2</sub> profile.

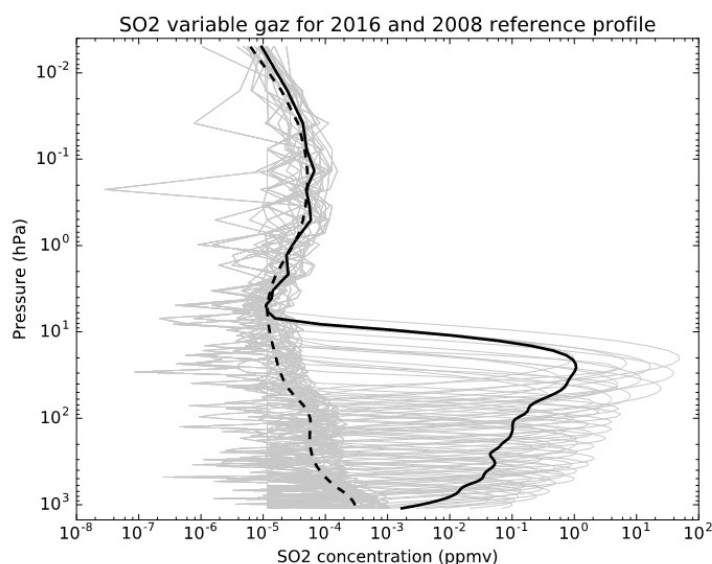


Figure 5: The 83 concentration profiles for SO<sub>2</sub> in the 2016 dataset, average profile (83) in black continuous line. The corresponding fixed profile for 2008 data-set is in dashed line. Units ppmv over dry air.

### 2.1.2 Updates to Visible and Infrared Line by Line Models and HITRAN

In order to evaluate the 2016 profile data-set, we compared the Line by Line (LBL) total transmittance used for predictor calculations between RTTOV-11 and RTTOV-12. The LBL model between RTTOV-11 and RTTOV-12 did not change. It is LBLRTM v12.2 with AER v3.2 molecular database and MT-CKD2.5.2 for continuum absorption (see R11REP2013 for a full description). The RTTOV-11 LBL calculations were obtained from the 2008 profile dataset and the RTTOV 12 LBL calculations were obtained with the new 2016 profile dataset. We do expect some differences in CO<sub>2</sub>, CH<sub>4</sub> and N<sub>2</sub>O due to the stretching of the profile datasets. Furthermore the addition of the new minor gases was evaluated.

On the top 3 panels of Figure 6 is represented, the infrared transmittance at the bottom of the atmosphere (BOA) for profile 83 for each RTTOV gases (except water vapour for clarity). The three plots are separated based on the range of transmittances. Some gases are not represented because their minimum transmittances are greater than 0.998 (HOCl, OH, HI, HBr, ClO and PH<sub>3</sub>). Gases represented in a grey box are the new minor gases. On the bottom plot of the panel is represented the BOA transmittance difference (RTTOV12 minus RTTOV11) for profile 83 for all gases combined. The maximum difference is -0.07 close to 3000 cm<sup>-1</sup> which is explained by the addition of C<sub>2</sub>H<sub>6</sub>. We can also see the spectral feature of HCL between 2800 and 3000 cm<sup>-1</sup>. The other smaller

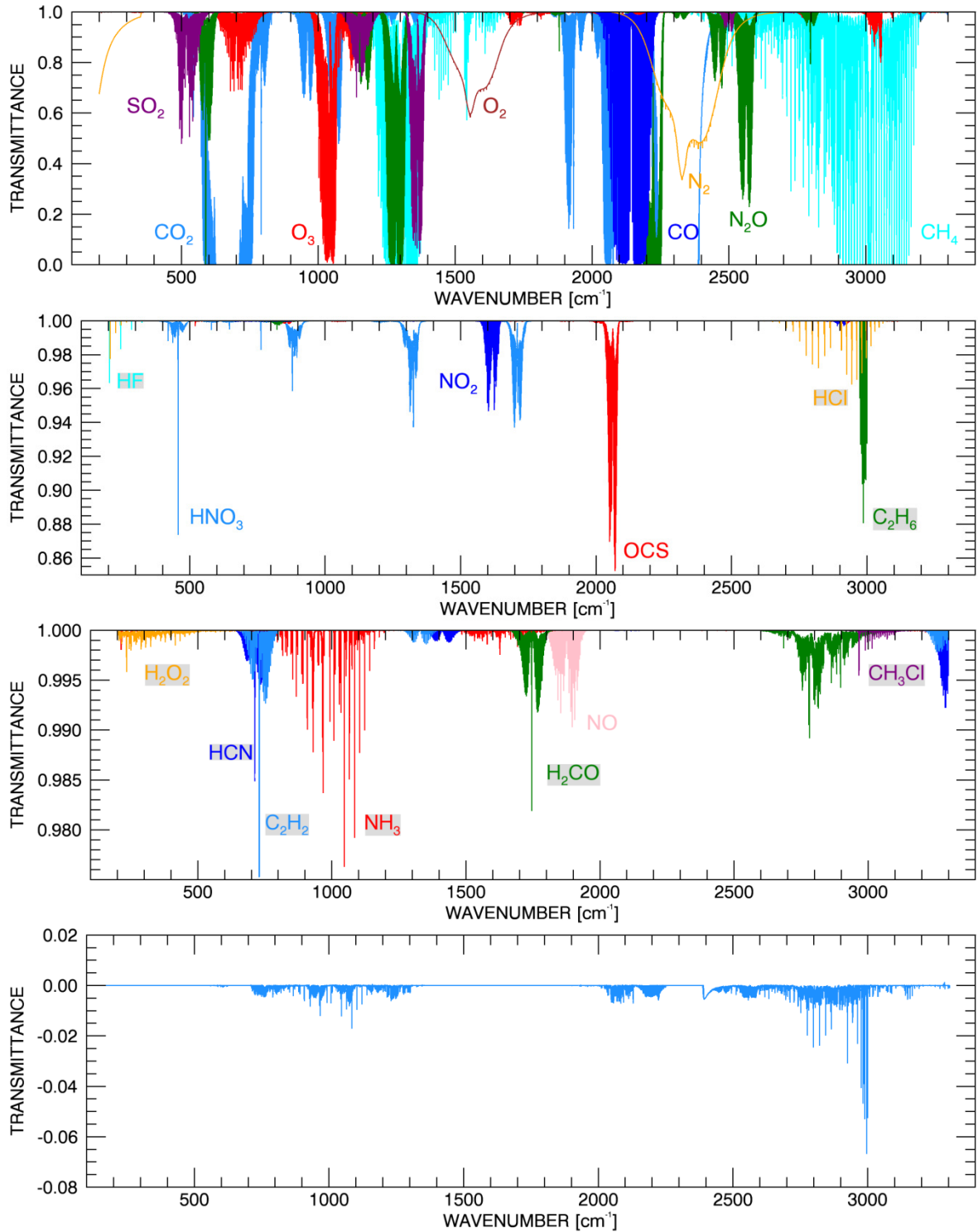


Figure 6: BOA IR transmittance for profile 83 for each RTTOV gas and difference between LBL transmittance for all gas between RTTOV-11 and RTTOV-12 (bottom spectra).

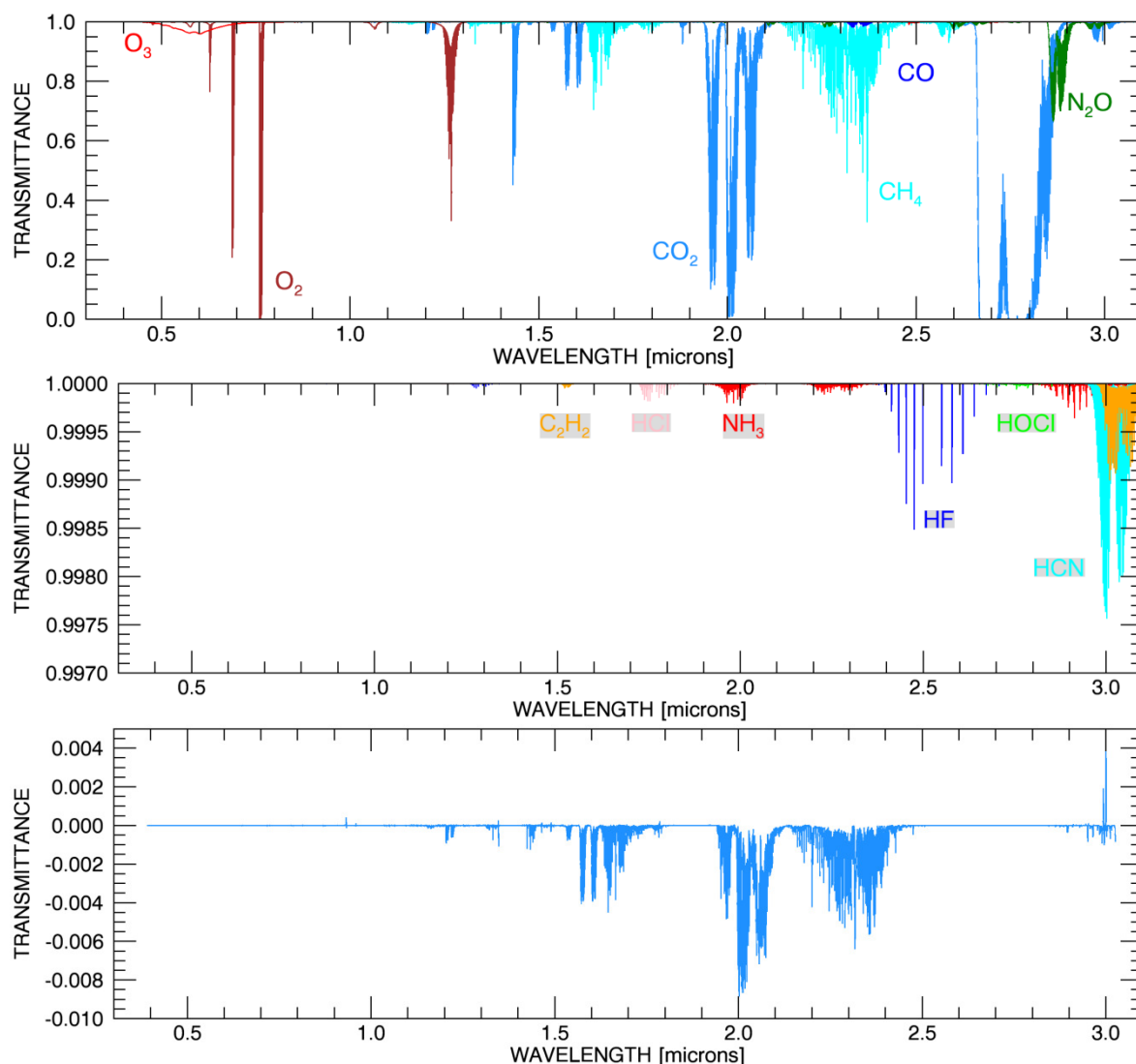


Figure 7: BOA VIS/NIR transmittance for profile 83 for each RTTOV gas and difference between LBL transmittance for all gas between RTTOV-11 and RTTOV-12 (bottom spectra).

difference (below -0.02) can be attributed to new minor gases but also in the difference profile dataset as for CO<sub>2</sub> close to 2400 cm<sup>-1</sup>.

On the panel of Figure 7 is a similar plot for the VIS/NIR spectral region. Some new minor gases are not represented due to their very low effects (i.e. OH, HBr, HI, ClO, H<sub>2</sub>CO, CH<sub>3</sub>Cl, H<sub>2</sub>O<sub>2</sub>, C<sub>2</sub>H<sub>6</sub>, PH<sub>3</sub>). The maximum difference of -0.008 between RTTOV-11 and RTTOV-12 is smaller for the VIS/NIR than for the IR. The differences are mainly explained by the different profile dataset for CO<sub>2</sub> and CH<sub>4</sub>.

### 2.1.3 Microwave Line by Line Model

Since the release of RTTOV-11v1 a major review of the microwave LbL code, `AMSUTRAN`, has been undertaken for RTTOV-12. Gas abundances in the user profile are now expected in ppmv with respect to *dry* air, in line with their definition in the training profiles used for RTTOV coefficients. New values for the half width of the 183 GHz water vapour line, and its temperature dependency, have been introduced from those recommended in Payne *et al.* (2008). The oxygen line parameters, previously taken from Liebe *et al.* (1992) were updated to those from Tretyakov *et al.* (2005).

An initialisation bug was corrected in the original line-by-line model code that will affect those sensors that have channels influenced by the 184 GHz ozone line, but is not confined to that region. Sensors such as ATMS, MTVZAGY, GMI, ICI, MWHS-2, MWI, MWS and SSMIS should use the latest coefficients from the corrected model to avoid this. For a given sensor, the effect is not easy to predict, since it arises from the way certain arrays were initialised in the code, and not from a systematic physical issue.

The differences from the previous version of the coefficients for ATMS are shown in Figure 8. Small differences in the channels, around 183 GHz, reflect the introduction of the new temperature dependency of the 183 GHz halfwidth, but some of the other channels, between the 22 GHz water vapour line and the oxygen band, show RMS differences of more than 0.5K, and these are due to the correction of the ozone error.

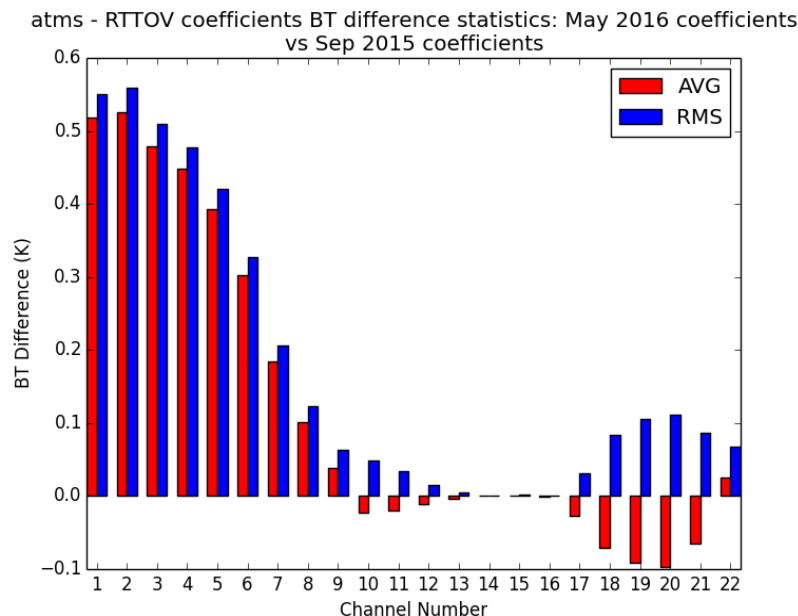


Figure 8. Differences for ATMS, bias (red) and RMSE (blue) over the training profiles in respect of the 184 GHz ozone error.

The differences for SSMIS are shown in Figure 9. The small differences in channels 9-11, around 183 GHz, reflect the new temperature dependency of the line halfwidth, but, as for ATMS, it is the lower frequency channels (here 12-16) that show the larger RMS differences due to the correction of the ozone error.

The differences for GMI are shown in Figure 10, and here the pattern is not the same. The differences in channel 10 and 11 reflect the previous omission of ozone absorption in the 165 GHz line, now rectified, and the differences for channels 12-13, around 183 GHz, reflect, as before, the introduction of the new temperature dependency of the line halfwidth. All other channels are only slightly affected. There are more plots for each MW sensor affected on the RTTOV web site.

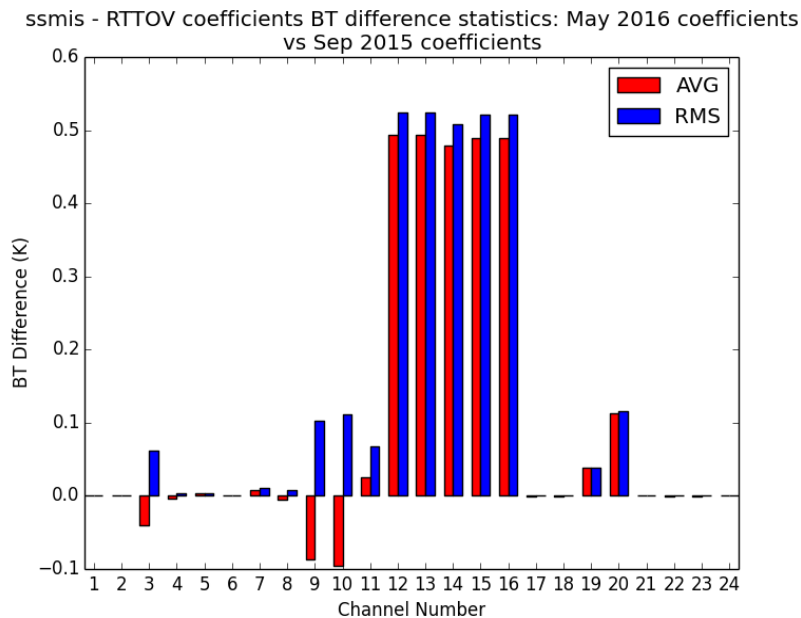


Figure 9. Differences for SSMIS, bias (red) and RMSE (blue) over the training profiles in respect of the 184 GHz ozone error.

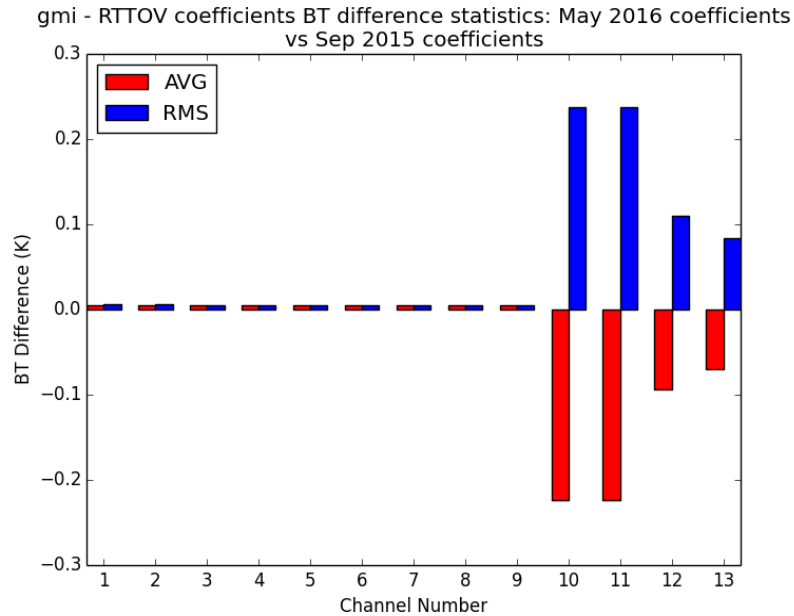


Figure 10. Differences for GMI, bias (red) and RMSE (blue) over the training profiles in respect of the 184 GHz ozone error.

A sensitivity study has also been conducted of the spectral resolution used for each sensor channel, and the channel passband frequencies are now calculated at run-time from the same filter file as is used in coefficient generation. A version of the code (see section 2.11) adapted exclusively for channels significantly affected by the Zeeman splitting of oxygen lines has now been amalgamated with the standard version of the model as an option.

In this updated version, a new interface allows the `AMSUTRAN` user to choose, for oxygen, between the usual MPM absorption routine and two routines closely based on the Rosenkranz model that allow for Zeeman splitting and the propagation of polarised Zeeman components. This model is essentially that described in Rosenkranz and Staelin (1988) but with a more sophisticated line shape that incorporates Doppler broadening. It uses the 'coherency matrix' formalism rather than the equivalent approach using Stokes vectors adopted by some microwave models.

As coded, exact transmittances may be obtained from `AMSUTRAN` for Zeeman channels that detect circularly polarised radiation (e.g. SSMIS), but the same approach for linear polarisation would, in the case where, off-nadir, a mixture of horizontal and vertical polarisations are detected (e.g. AMSU-A), require RTTOV to predict more than one transmittance for each Zeeman channel. To avoid this in such cases, an approximate

|   |   |   |   |
|---|---|---|---|
| <p>The EUMETSAT<br/>Network of<br/>Satellite Application<br/>Facilities</p> |  | <p>RTTOV-12 Science and<br/>Validation Report</p> | <p>Doc ID : NWPSAF-MO-TV-41<br/>Version : 1.0<br/>Date : 16/02/2017</p> |
|---|---|---|---|

scheme has been retained from earlier work (Han 2007) for RTTOV-9 that averages the transmittances for the two linear polarisations.

## 2.2 Addition of SO<sub>2</sub> as a variable gas

In RTTOV-12, new optical depth coefficient files have been introduced that allow for an additional variable gas, SO<sub>2</sub>, for the advanced IR sounders. If no user SO<sub>2</sub> profile is supplied, a reference climatological SO<sub>2</sub> profile for a “clean” (i.e. non-volcanic) atmosphere is used by default. The variable-SO<sub>2</sub> coefficients are trained using the 2016 extended diverse 83 profile set (see section 2.1) combined with 59 SO<sub>2</sub> profiles representing volcanic plumes. These volcanic profiles, 23 SO<sub>2</sub> profiles representing the natural variability of SO<sub>2</sub> in a clean atmosphere, the clean profiles, and the final SO<sub>2</sub> profile being the mean of these 82 profiles.

The plots below show statistical comparisons between RTTOV simulated radiances and radiances from line-by-line calculations, in terms of brightness temperatures for the variable-SO<sub>2</sub> IASI coefficients.

The simulations are run for all zenith angles used in the coefficient training and include contributions from atmospheric emission and emission from a surface with unit emissivity located at the bottom level of the coefficient pressure profile. The LBL radiances are calculated using the LBL channel-integrated optical depths, and so comparisons with RTTOV radiances give an indication of the error resulting from the optical depth regression scheme. The plots in Figure 11 show the average (mean), RMS and maximum absolute difference between the RTTOV and LBL radiances calculated over all zenith angles and either the subset of 23 profiles for the clean atmospheres or the subset of 59 profiles associated with volcanic profiles. For the clean profiles the rms differences are all below 0.5 K but for the volcanic case the rms differences can be up to 1 K. More work is planned on improving the predictor sets for future versions of RTTOV.

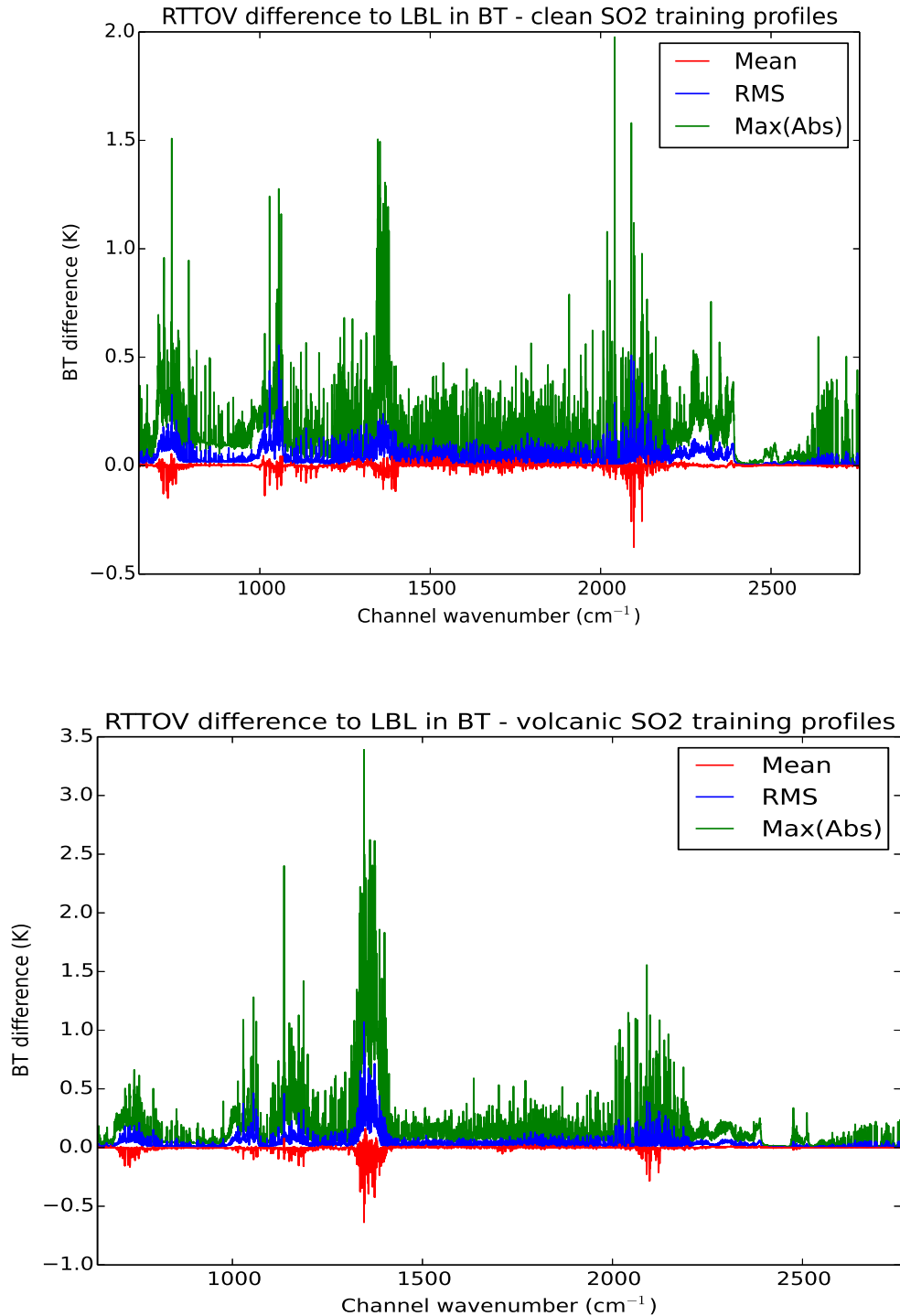


Figure 11. Top panel is the RTTOV – LBL model difference for climatological SO<sub>2</sub> values. Bottom panel is for volcanic plume profiles.

|   |   |   |   |
|---|---|---|---|
| <p>The EUMETSAT<br/>Network of<br/>Satellite Application<br/>Facilities</p> |  | <p>RTTOV-12 Science and<br/>Validation Report</p> | <p>Doc ID : NWPSAF-MO-TV-41<br/>Version : 1.0<br/>Date : 16/02/2017</p> |
|---|---|---|---|

### 2.3 Specification of cloud/aerosol units

The conversion of clouds/aerosols from mass mixing ratio to RTTOV input units (LWC/IWC for clouds and number concentration for aerosols) is described here. The conversion is implemented in RTTOV-12 as an option for users. Care must be taken as the cloud/aerosols units for conversion are for mass mixing ratio relative to moist air.

#### The unit's conversion for clouds

The optical properties of ice and water clouds in RTTOV are parameterized from ice water content (IWC) and liquid water content (LWC) in  $\text{g.m}^{-3}$ , respectively. However, NWP models provide cloud information in units of mass mixing ratio (or specific cloud ice or liquid water content) in  $\text{kg.kg}^{-1}$ , i.e. ratio between the mass of ice/liquid water and the mass of moist air. If we consider that the air follows the perfect gas law, then the conversion for ice cloud is:

$$IWC = MMR_{ice} \frac{P}{R_{ma}T} \quad (2.3.1)$$

where  $MMR_{ice}$  is the mass mixing ratio for ice cloud,  $P$  is the atmospheric pressure in Pa,  $T$  is the atmospheric temperature in K and  $R_{ma}$  is the moist air gas constant (in  $\text{m}^3.\text{Pa.K}^{-1}.\text{mol}^{-1}$ ) given by:

$$R_{ma} = R_{da} \left(1 + \frac{1-\varepsilon}{\varepsilon} q\right) \quad (2.3.2)$$

where  $R_{da}$  is the gas constant for dry air and  $q$  is the specific humidity (given as the ratio between the mass of water vapor and the mass of moist air). The equation is demonstrated in Jacobson (2005, equation 2.31). The coefficient  $\varepsilon$  is given by:

$$\varepsilon = \frac{M_{wv}}{M_{da}} \quad (2.3.3)$$

where  $M_{wv}$  and  $M_{da}$  are the molecular weight for water vapor and for dry air in  $\text{g.mol}^{-1}$ , respectively. They are named `mh2o` and `mair` in `rttov_const.F90`.

The gas constant for dry air is given by:

$$R_{da} = \frac{R}{M_{da}} \quad (2.3.4)$$

where  $R$  is the universal gas constant (named `rgc` in `rttov_const.F90` in  $\text{J.mol}^{-1}.\text{K}^{-1}$  that is equivalent to  $\text{m}^3.\text{Pa.K}^{-1}.\text{mol}^{-1}$ ). For liquid clouds, same equations can be used.

#### The unit's conversion for aerosol

The optical properties of aerosols in RTTOV are pre calculated for one particle per  $\text{cm}^{-3}$ . To calculate the total optical properties within each aerosol layer, the pre calculated optical properties have to be multiplied by the aerosol number concentration. As clouds, NWP

models such as MACC/CAMS provide aerosol information in units of mass mixing ratio in  $\text{kg.kg}^{-1}$  (ratio between the aerosol mass and the mass of moist air). For aerosols the unit conversion is more complex than for clouds since the RTTOV aerosol unit is in number concentration instead of mass concentration. Fortunately, for RTTOV aerosol types based on OPAC (Hess *et al.*, 1998), the conversion term between mass concentration and number concentration, called  $M^*$  [in  $\text{g.m}^{-3}/\text{part.cm}^{-3}$ ], is provided for each OPAC aerosol types (number 1 to 10 in RTTOV) in Table 1c of Hess et al (1998). The conversion of the mass mixing ratio ( $MMR_i$ ) of aerosol type  $i$  in number concentration ( $N_i$ ) is given by:

$$N_i = MMR_i \frac{P}{R_{ma} T M_i^*} \quad (2.3.5)$$

where  $MMR_i$  is the mass mixing ratio for RTTOV aerosol type  $i$ ,  $P$  is the atmospheric pressure in Pascal,  $T$  is the atmospheric temperature in Kelvin and  $R_{ma}$  is given by equation (2.3.5). The terms  $M_i^*$  are given in Table 1 for each RTTOV aerosol model.

| Type | RTTOV Number | $M_i^*$  |
|------|--------------|----------|
| INSO | 1            | 2.37E-5  |
| WASO | 2            | 1.34E-9  |
| SOOT | 3            | 5.99E-11 |
| SSAM | 4            | 8.02E-7  |
| SSCM | 5            | 2.24E-4  |
| MINM | 6            | 2.78E-8  |
| MIAM | 7            | 5.53E-6  |
| MICM | 8            | 3.24E-4  |
| MITR | 9            | 1.59E-5  |
| SUSO | 10           | 2.28E-8  |
| VOLA | 11           | 39.258   |
| VAPO | 12           | 13.431   |
| ASDU | 13           | 1.473E-4 |

Table 1. Terms  $M_i^*$  of Eq. (2.3.5) for RTTOV aerosol types.

For other aerosol types not based on OPAC (number 11: volcanic ash or VOLA; number 12: new volcanic ash or VAPO; and number 13: Asian dust or ASDU), the conversion term  $M_i^*$  is calculated from the particle size distribution using the same assumptions as for OPAC. If we assume that the aerosol is spherical then:

$$M_i^* = \int_{r_{min}}^{r_{max}} \frac{4}{3} \pi r^3 \rho_i n_i(r) dr \quad (2.3.6)$$

where  $r_{min}$  and  $r_{max}$  are the minimum and maximum radius of the particle size distribution  $n_i(r)$  and  $\rho_i$  is the particle density of type  $i$ . In Hess et al. (1998),  $r_{max}$  is fixed to 7.5  $\mu\text{m}$ . For the two volcanic ash types (VOLA and VAPO) the density is assumed to be 2.6  $\text{g/cm}^3$  which is appropriate for andesite (the refractive indices selected for the VAPO particle type

|   |   |   |   |
|---|---|---|---|
| <p>The EUMETSAT<br/>Network of<br/>Satellite Application<br/>Facilities</p> |  | <p>RTTOV-12 Science and<br/>Validation Report</p> | <p>Doc ID : NWPSAF-MO-TV-41<br/>Version : 1.0<br/>Date : 16/02/2017</p> |
|---|---|---|---|

introduced in RTTOVv11.1 are for andesite) and the conversion factors were then calculated from the respective size distributions of the ash types.

For the volcanic ash aerosol model of RTTOV (named VOLA), the particle size distribution is a modified Gamma size distribution, given by:

$$n_i(r) = N_i a r^\alpha \exp\left[-\frac{\alpha}{\gamma} \left(\frac{r}{r_{mod,i}}\right)^\gamma\right] \quad (2.3.7)$$

where the different coefficients are  $a = 5461$ ,  $\alpha = 1$ ,  $\gamma = 0.5$  and  $r_{mod,i} = 0.0156 \mu\text{m}$ . For the integration of Eq. (6), we used  $r_{min} = 0.005 \mu\text{m}$  and  $r_{max} = 20 \mu\text{m}$  (Matricardi, 2005). By considering that the calculation is relative to 1 particle per  $\text{cm}^{-3}$  (i.e.,  $N_i = 1$ ), then the value of  $M^*$  is given in Table 1.

For the new volcanic ash aerosol model (named VAPO), a log-normal distribution is used, i.e.:

$$n_i(r) = \frac{N_i}{\sqrt{2\pi r \log(\sigma_i) \ln(10)}} \exp\left[-\frac{1}{2} \left(\frac{\log(r) - \log(r_{mod,i})}{\log(\sigma_i)}\right)^2\right] \quad (2.3.8)$$

with  $r_{mod,i} = 0.610482 \mu\text{m}$  and  $\sigma_i = 1.85$ . Again, by considering  $r_{min} = 0.005 \mu\text{m}$ ,  $r_{max} = 7.5 \mu\text{m}$  and that the calculation is relative to 1 particle per  $\text{cm}^{-3}$  (i.e.,  $N_i = 1$ ), then the value of  $M^*$  is also given in Table 1.

For the Asian dust aerosol model (named ASDU), the particle size distribution is given by a linear combination of log-normal PSDs (Eq. 8) for mineral nucleated, accumulated and coalesced types and with relative weights of 0.862, 0.136 and  $0.217 \times 10^{-2}$ , respectively. The parameters of the PSDs are given in Table 2 of Matricardi (2005). Again, by considering that the calculation is relative to 1 particle per  $\text{cm}^{-3}$  (i.e.,  $N_i = 1$ ) and by integrating between 0.005 and 7.5  $\mu\text{m}$ , the value of  $M^*$  is also given in Table 1.

## 2.4 Discrete ordinates scattering

The Discrete Ordinates Method or DOM (Chandrasekhar, 1960) has been implemented in RTTOV as an option for treating solar radiation and thermal emission for visible/near-IR and IR channels. The choice of solver for the thermal emission and solar source terms can be selected independently: for thermal emission the choice is between the existing ‘‘Chou-scaling’’ parameterisation and DOM. For solar radiation the choice is between the existing single-scattering and DOM.

RTTOV-9 introduced the ‘‘Chou-scaling’’ parameterisation for multiple scattering by clouds and aerosols in the IR and a single-scattering calculation for solar radiation in the short-wave IR (Matricardi, 2005). RTTOV-11 introduced the capability to simulate visible/near-IR channels and the single-scattering calculation was applied to these wavelengths for cloud and aerosol simulations. The single-scattering calculation is very poor, particularly in

|   |   |   |   |
|---|---|---|---|
| <p>The EUMETSAT<br/>Network of<br/>Satellite Application<br/>Facilities</p> |  | <h2 style="text-align: center;">RTTOV-12 Science and<br/>Validation Report</h2> | <p>Doc ID : NWPSAF-MO-TV-41<br/>Version : 1.0<br/>Date : 16/02/2017</p> |
|---|---|---|---|

cases where scattering dominates absorption, and so a multiple scattering model has been developed within RTTOV.

RTTOV-12 introduces the option to use the Discrete Ordinates Method or DOM (Chandrasekhar, 1960) to account for multiple scattering in the visible and IR due to aerosols and clouds. The implementation is very similar to that in the DISORT model (Stamnes *et. al.*, 1988) such that the radiances from RTTOV-12 agree to at least 4 significant figures with those from DISORT when equivalent inputs are used. The mathematical details of the DOM algorithm are not repeated here since they are widely available in the literature. A more comprehensive description of the implementation is given in Hocking (2015) which also provides an indication of the errors which result from applying the monochromatic DOM solver channels of finite spectral width.

There is one significant difference between the RTTOV and DISORT implementations of DOM: for solar simulations RTTOV takes the full phase functions as input and directly interpolates them at the scattering angle where required. In contrast DISORT reconstructs the phase function from the full Legendre expansion: this is not a practical solution for some phase functions at visible wavelengths which may require many thousands of Legendre terms in order to be accurately reconstructed. RTTOV-12 therefore only requires as many Legendre coefficients as there are Discrete Ordinates (or “streams”) in the calculation.

The DOM implementation treats thermally emitted (IR) and solar radiation separately for reasons of efficiency. The scattering models used in the IR and the visible/near-IR may be selected independently. By default Chou-scaling is used in the IR and DOM is used for solar radiation.

The DOM algorithm currently treats the surface as strictly Lambertian. For IR calculations the surface albedo is calculated as  $(1-emissivity)$ . For solar calculations the surface albedo is calculated as  $(\pi*BRDF)$  and this value is capped at one to prevent unphysical albedo values being used.

The standard DOM algorithm requires a strictly plane-parallel atmosphere. Therefore whenever DOM calculations are selected (for IR and/or visible channels) RTTOV enforces this by turning off the usual geometry calculations which account for the curvature of the Earth and, optionally, for atmospheric refraction. A switch has been added in the options so that users can choose to enforce the plane-parallel option themselves: this is primarily intended to allow comparisons of the alternative scattering models with DOM.

The inputs to the RTTOV DOM algorithm for each layer are the absorption and scattering coefficients, the Legendre coefficients corresponding to the phase function, and, for solar channels, the phase function itself. The cloud and aerosol coefficient files include these properties for the same aerosol and water cloud particle types as in RTTOV-11. For ice cloud the Hexagonal and Aggregate ice shape properties have been replaced with

|   |   |   |   |
|---|---|---|---|
| <p>The EUMETSAT<br/>Network of<br/>Satellite Application<br/>Facilities</p> |  | <h2 style="text-align: center;">RTTOV-12 Science and<br/>Validation Report</h2> | <p>Doc ID : NWPSAF-MO-TV-41<br/>Version : 1.0<br/>Date : 16/02/2017</p> |
|---|---|---|---|

properties taken from the SSEC ice dataset (Baum *et. al.*, 2011). The parameterisation of the Baran ice property database introduced in RTTOV-11 has been extended to visible wavelengths (described in section 2.5) which provides an alternative treatment for ice clouds.

As noted above RTTOV requires the same number of Legendre coefficients as DOM streams: the user selects the number of streams in the options structure. The aerosol and cloud coefficient files include up to 128 Legendre coefficients for each channel: there may be fewer for phase functions where the coefficients grow sufficiently small in magnitude (less than  $10^{-6}$ ). This places an upper limit of 128 on the number of Discrete Ordinates which may be selected when using optical properties from the coefficient files. As in RTTOV-11 users have the option of providing the optical properties explicitly in which case there is no fixed upper limit.

DOM is a solver for monochromatic radiances. However, RTTOV simulates radiances with a finite spectral bandwidth and the standard RTTOV gas absorption optical depths are used as inputs to the DOM algorithm. The errors which result from this are investigated in a separate report (Hocking, 2015). In summary, for the test cases the errors resulting specifically from applying DOM to polychromatic quantities were of the order of 1-2% in radiance for visible/near-IR channels and the errors are dominated by variability in optical properties (especially the phase function) across the channel. In the infrared the errors are dominated by the variability of gas absorption across the channel and as the amount of scattering material in the atmosphere increases the errors decrease because the optical properties of clouds/aerosols vary relatively slowly across the sensor channels and this begins to dominate over the gas absorption. The study did not indicate any obvious problems with the application of the monochromatic DOM solver to channels of finite spectral bandwidth.

The DOM algorithm is relatively slow and so RTTOV-12 employs some techniques to speed up the calculation. Where possible results are re-used internally: this can result in significant reductions in run-time when dealing with the multiple cloud columns generated by the cloud overlap assumptions. In addition the treatment of “clear” layers in the algorithm (i.e. those containing no scattering material) is relatively rapid: this applies particularly to visible/near-IR channels.

Finally it should be noted that the DOM algorithm in RTTOV does not currently treat atmospheric Rayleigh scattering. It would be very expensive to do so as it would imply the presence of scattering particles in (almost) every layer which slows the algorithm significantly. It is also the case that currently the LBLRTM simulations used to train RTTOV include extinction due to Rayleigh scattering and as such the optical depth coefficients would have to be recomputed with this option turned off. This in turn would require an additional parameterisation of the Rayleigh extinction to be developed for clear-sky visible/near-IR simulations. The existing Rayleigh single-scattering calculation is included as an “additive” effect alongside DOM: there is no interaction between the

Rayleigh scattered radiation and the clouds/aerosols except for increased extinction by Rayleigh scattering (included in the gaseous optical depths used in DOM) and by clouds/aerosols (included in the Rayleigh single-scattering calculation). This leads to an underestimation of the top-of-atmosphere reflectances as the optical thickness of the scattering layers increases and as the wavelength decreases (Scheck, 2016). Improvements to the treatment of Rayleigh scattering will be investigated for a future version of RTTOV.

## 2.5 Ice cloud scattering

A new ice cloud optical properties parameterization has been included in RTTOV-12 for the visible and the near infrared spectral ranges. The parameterization follows the methodology developed for the infrared (Vidot *et. al.*, 2015) by using a large database of optical properties of ice clouds provided by Anthony Baran from the Met Office. The Self-Consistent Scattering Model (SCSM) database consists of 20662 particle size distributions described in Baran *et. al.* (2014) using different in-situ measured temperature (T) and estimated ice water content (IWC) observations, and their distribution is shown in Figure 12. It shows that the SCSM database covers a large range of both IWC and temperature values. For each couple of IWC and T, the database contains the extinction coefficient ( $\beta_{ext}$ ), the single scattering albedo ( $\omega_0$ ) and the asymmetry parameter ( $g$ ) at 33 wavelengths between 0.2 and 3.3 microns.

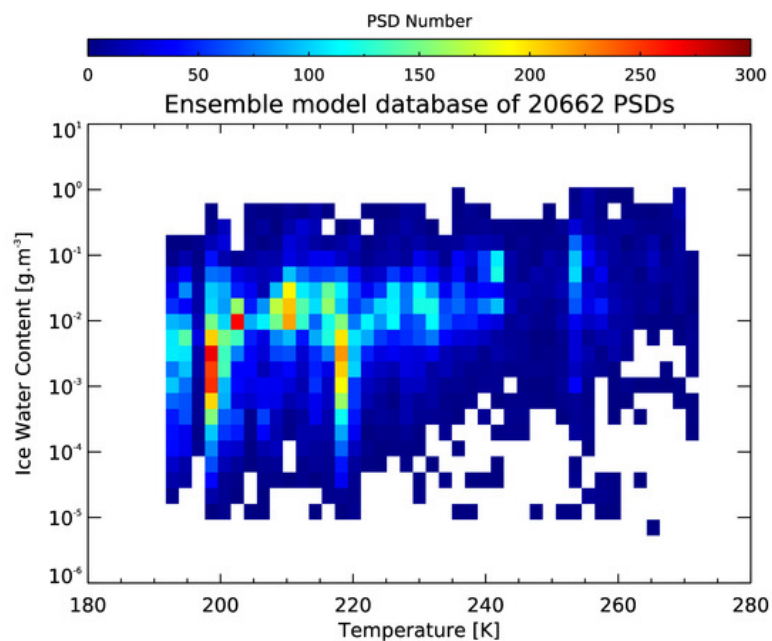


Figure 12. A 2-dimensional histogram of ice water content (in  $g.m^{-3}$ ) versus temperature (in K) of the 20662 PSD database.

To make use of the VIS/NIR scattering model of RTTOV (DOM), the phase function is calculated from the asymmetry parameter following Baran *et. al.* (2001) and the Legendre expansion of the phase function is calculated internally in RTTOV. The VIS/NIR parameterisation that has been implemented into RTTOV-12 is given by the following equations:

$$\log_{10}[\beta_{ext}(\lambda, T, IWC)] = A_{\beta}(\lambda) + B_{\beta}(\lambda)T + C_{\beta}(\lambda)\log_{10}(IWC) + D_{\beta}(\lambda)T^2 + E_{\beta}(\lambda)(\log_{10}(IWC))^2 + F_{\beta}(\lambda)T\log_{10}(IWC) \quad (2.5.1)$$

$$\varpi_0(\lambda, T, IWC) = A_{\varpi_0}(\lambda) + B_{\varpi_0}(\lambda)T + C_{\varpi_0}(\lambda)\log_{10}(IWC) \quad (2.5.2)$$

$$g(\lambda, T, IWC) = A_g(\lambda) + B_g(\lambda)T + C_g(\lambda)\log_{10}(IWC) \quad (2.5.3)$$

The parameterisation coefficients A to F of  $\beta_{ext}$ ,  $\varpi_0$  and  $g$  were calculated by using a non-linear least squares fitting procedure over the SCSM database, and are also functions of wavelength. In order to validate the parameterization, we have compared the parameterization to the database by splitting the database into 5 IWC bins (IWC > 10<sup>-1</sup> g.m<sup>-3</sup>, IWC between 10<sup>-2</sup> and 10<sup>-1</sup> g.m<sup>-3</sup>, IWC between 10<sup>-3</sup> and 10<sup>-2</sup> g.m<sup>-3</sup>, IWC between 10<sup>-4</sup> and 10<sup>-3</sup> g.m<sup>-3</sup> and IWC < 10<sup>-4</sup> g.m<sup>-3</sup>). Overall, the difference for the 3 parameters shown in Figures 13-15 is below 5% and is lower than 3% for larger IWC (in blue, red and green lines).

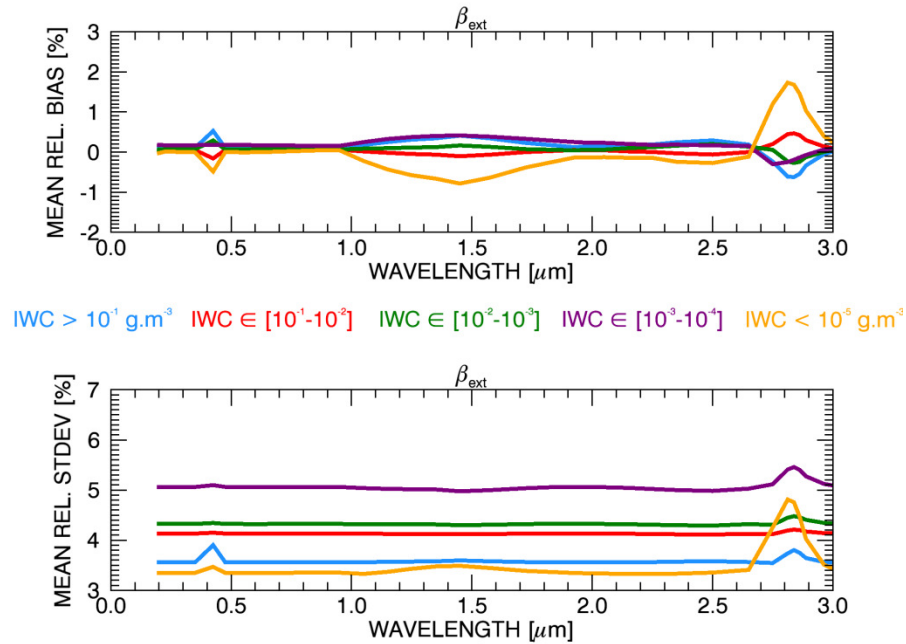


Figure 13: Mean relative bias (top) and relative standard deviation (bottom) of the difference between parameterized and database extinction coefficient versus wavelength. The different IWC groups are represented in different colours.

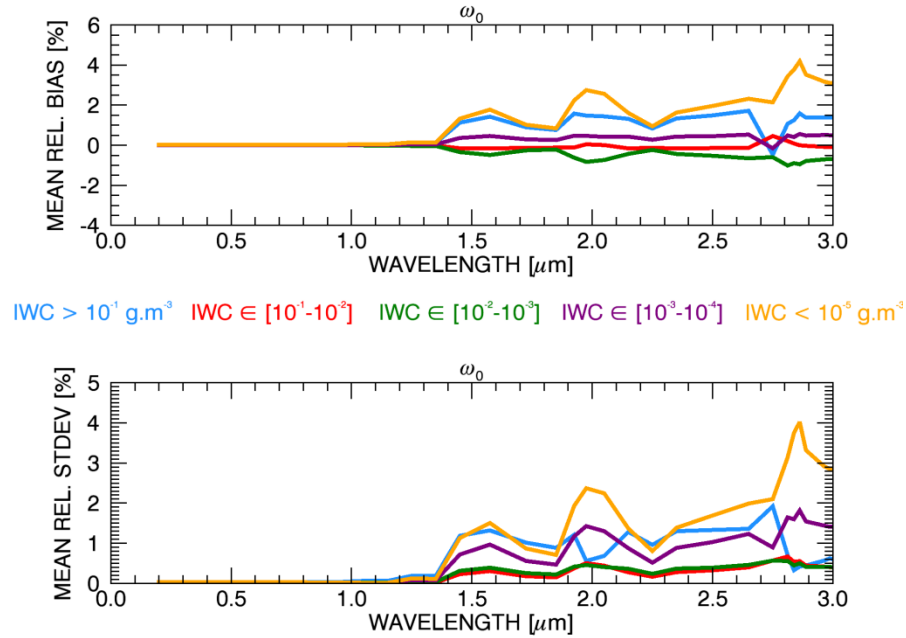


Figure 14: Same as Fig. 13 for the single scattering coefficient.

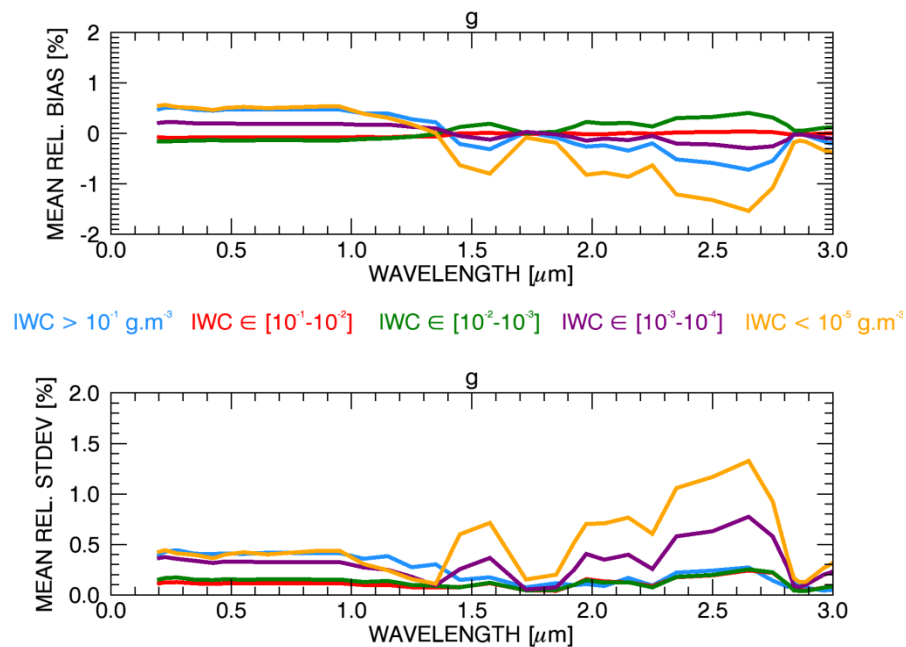


Figure 15: Same as Fig. 13 for the asymmetry parameter.

|   |   |   |   |
|---|---|---|---|
| <p>The EUMETSAT<br/>Network of<br/>Satellite Application<br/>Facilities</p> |  | <h2 style="text-align: center;">RTTOV-12 Science and<br/>Validation Report</h2> | <p>Doc ID : NWPSAF-MO-TV-41<br/>Version : 1.0<br/>Date : 16/02/2017</p> |
|---|---|---|---|

## 2.6 Infrared surface emissivity

### 2.6.1 Over ocean

The IR sea surface emissivity model ISEM (Sherlock, 1999) has been the only option available for IR sensors in RTTOV since version 6. This model parameterises emissivity only in terms of zenith angle. PC-RTTOV uses a more physically-based emissivity model which additionally includes a wind-speed dependence (Matricardi, 2010). A new emissivity model has been developed for use with IR sensors. This is similar to the PC-RTTOV emissivity model, but also includes skin temperature-dependent refractive indices in the 10-12 $\mu$ m window (Newman *et. al.*, 2005). The model was validated through comparisons against SEVIRI, AATSR and IASI observations alongside ISEM and the PC-RTTOV model. The largest differences (generally improvements) to ISEM are observed at wind speeds above  $\sim$ 12m/s, zenith angles above 60 $^{\circ}$  (the new model is explicitly trained up to higher zenith angles for GEO sensors) and (for some instruments) at skin temperatures below  $\sim$ 300K. ISEM remains as an option for RTTOV-12 to maintain backward compatibility. In the future the new model will be used to train PC-RTTOV coefficients.

Two IR sea surface emissivity models are implemented in RTTOV v9-v11:

- For “standard” simulations the ISEM model (Sherlock, 1999) is used in which emissivity is parameterised in terms of zenith angle. ISEM is based on the Masuda (1988) model which calculates the emissivity from a rough sea surface with the Cox and Munk (1954) isotropic wave slope statistics. ISEM uses emissivities calculated for a wind speed of zero. Refractive indices are from Hale and Querry (1973) with the Friedman (1969) salinity correction.
- The PC-RTTOV emissivity model (Matricardi, 2010) parameterises emissivity in terms of zenith angle and wind speed. This is also based on the Masuda model, but includes the first order surface-emitted surface-reflected (SESR) term from Wu and Smith (1997) and the refractive indices are again from Hale and Querry, but the Pinkley and Williams (1976) salinity correction is applied.

RTTOV-12 retains ISEM as an option and introduces a new sea surface emissivity model, referred to as “IREMIS”. The new model is the default for standard RTTOV simulations. Currently PC-RTTOV still uses the model described above, but eventually the new model will replace this. The new model has the following characteristics:

- Emissivity is parameterised in terms of zenith angle, wind speed and skin temperature.
- Refractive indices are from the Hale and Querry dataset with the Pinkley and Williams salinity correction. However in the 10-12 $\mu$ m window the Newman *et. al.* (2005) dataset is used which introduces a linear dependence of refractive index on skin temperature. At each end of the spectral range covered by the Newman *et. al.*

|   |   |   |   |
|---|---|---|---|
| <p>The EUMETSAT<br/>Network of<br/>Satellite Application<br/>Facilities</p> |  | <h2 style="text-align: center;">RTTOV-12 Science and<br/>Validation Report</h2> | <p>Doc ID : NWPSAF-MO-TV-41<br/>Version : 1.0<br/>Date : 16/02/2017</p> |
|---|---|---|---|

data the Newman *et. al.* and Hale and Query datasets are linearly merged into one another to create a smooth transition between them. Outside the Newman *et. al.* spectral range there is no skin temperature dependence.

- The wave slope model is based on Masuda (2006) which in turn is a development of the Masuda (1988) model. In IREMIS only the first order SESR term is considered. The wave slope statistics are taken from Ebuchi and Kizu (2002) rather than Cox and Munk.

A database of emissivities is calculated off-line covering zenith angles of 0-75° in steps of 2.5°, wind speeds of 0-20 ms<sup>-1</sup> in steps of 1 ms<sup>-1</sup>, and in steps of 1cm<sup>-1</sup> wavenumbers across the spectral range covered by RTTOV IR simulations. In addition, for the spectral region where refractive indices vary with skin temperature the emissivities are calculated at two skin temperatures which is sufficient to capture the nominally linear relationship between skin temperature and emissivity.

During the RTTOV coefficient file generation process the emissivities from the database are averaged over each channel spectral response function for broadband radiometers or for hyperspectral sounders the emissivities are interpolated to the channel wavenumbers. The resulting emissivities,  $\varepsilon$ , for each channel are parameterised by fitting a function of the following form:

$$\begin{aligned}
 A &= c_1 + c_2 w + c_3 w^2 \\
 B &= c_4 + c_5 w + c_6 w^2 \\
 \varepsilon &= A + (B - A) \exp\left(\frac{(c_9 - \theta_{\max})^2 - (\theta - c_9)^2}{c_7 + c_8 w}\right) + (T - T_0) \left[ d_1 + \exp\left(\frac{d_2 \theta^2}{\theta_{\max}^2}\right) \right]
 \end{aligned} \tag{2.6.1}$$

where  $w$  is the wind speed,  $\theta$  is the zenith angle,  $T$  is the skin temperature,  $\theta_{\max}$  is the largest zenith angle used in training (either 60° or 75°, see below),  $T_0$  is a reference skin temperature (301.2K), and  $c_1 - c_9, d_1, d_2$  are coefficients derived by least-squares minimisation over emissivities. Coefficients  $c_1 - c_3$  are determined by fitting emissivities  $A$  over all wind speeds at zenith angle 0° for the reference skin temperature; coefficients  $c_4 - c_6$  are determined by fitting emissivities  $B$  over all wind speeds at a zenith angle  $\theta_{\max}$  for the reference skin temperature;  $c_7 - c_9$  are determined using  $c_1 - c_6$  and fitting emissivities over all wind speeds and zenith angles for the reference skin temperature; and finally, for channels within the range of the skin temperature-dependent emissivities, coefficients  $d_1$  and  $d_2$  are determined by fitting all emissivities at the second (non-reference) skin temperature. The first part of the parameterisation (for  $c_1 - c_9$ ) is the same

as that in the PC-RTTOV emissivity model. The coefficients  $c_1 - c_9, d_1, d_2$  are then stored in the optical depth coefficient file.

For instruments in low Earth orbits  $\theta_{\max}$  is set to  $60^\circ$  since zenith angles above this are not usually observed (note that  $\theta_{\max} = 60^\circ$  for the PC-RTTOV model). For sensors in geostationary orbits  $\theta_{\max}$  is set to  $75^\circ$ : this was selected as it gives reasonably small errors in the parameterisation over zenith angles in the range  $0-85^\circ$  without compromising the accuracy too much in the range  $0-60^\circ$ . When  $\theta_{\max}$  was set to  $85^\circ$  the errors at lower zenith angles were larger. Figure 16 shows the errors in the parameterisation. For LEO sensors (zenith angles of  $0-60^\circ$ ) the fit of IREMIS parameterisation is of similar quality to that of the PC-RTTOV model.

Figures 17-19 show comparisons of observed SEVIRI brightness temperatures for the 3.9, 8.7, 10.8 and  $12.0\mu\text{m}$  channels and corresponding RTTOV simulated brightness temperatures using ISEM, the PC-RTTOV emissivity model and the new IREMIS model. The statistics were gathered for clear pixels over 10 slots taken from different days. Differences greater than 2K were excluded from the statistics on the grounds that such differences cannot be due to errors in surface emissivity alone and instead are likely to be a result of errors in cloud screening or in the NWP model background fields used for the simulations.

The plots indicate there is not a very large difference between the models in practice although ISEM exhibits larger standard deviations at higher wind speeds which is not surprising since ISEM does not take wind speed into account.

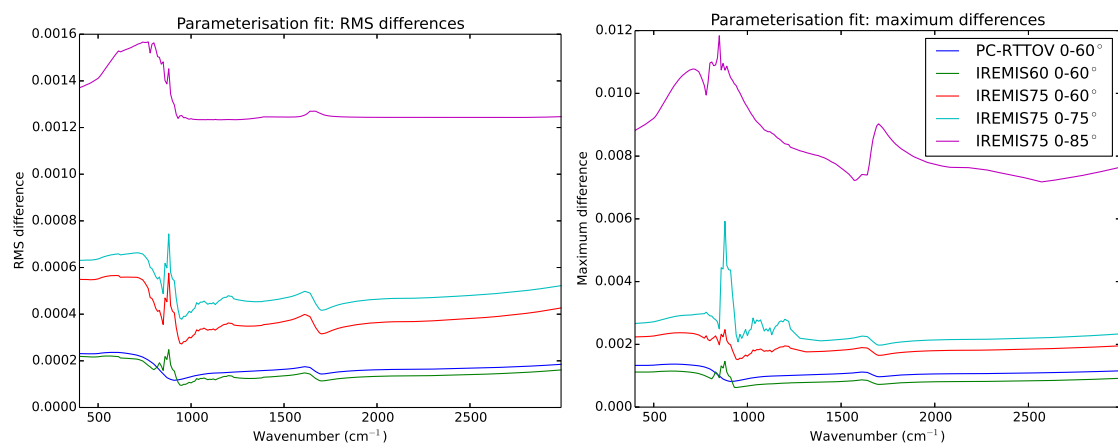


Figure 16: Showing the RMS and maximum differences between the parameterised and database emissivity values over all wind speeds and (where relevant) skin temperature values and over the ranges of zenith angles specified in the legend ( $0-60^\circ$ ,  $0-75^\circ$  and  $0-85^\circ$ ). The PC-RTTOV model is trained for angles in the range  $0-60^\circ$ . The IREMIS60 and IREMIS75 statistics are for the IREMIS model trained for angles in the range  $0-60^\circ$  and  $0-75^\circ$  respectively.

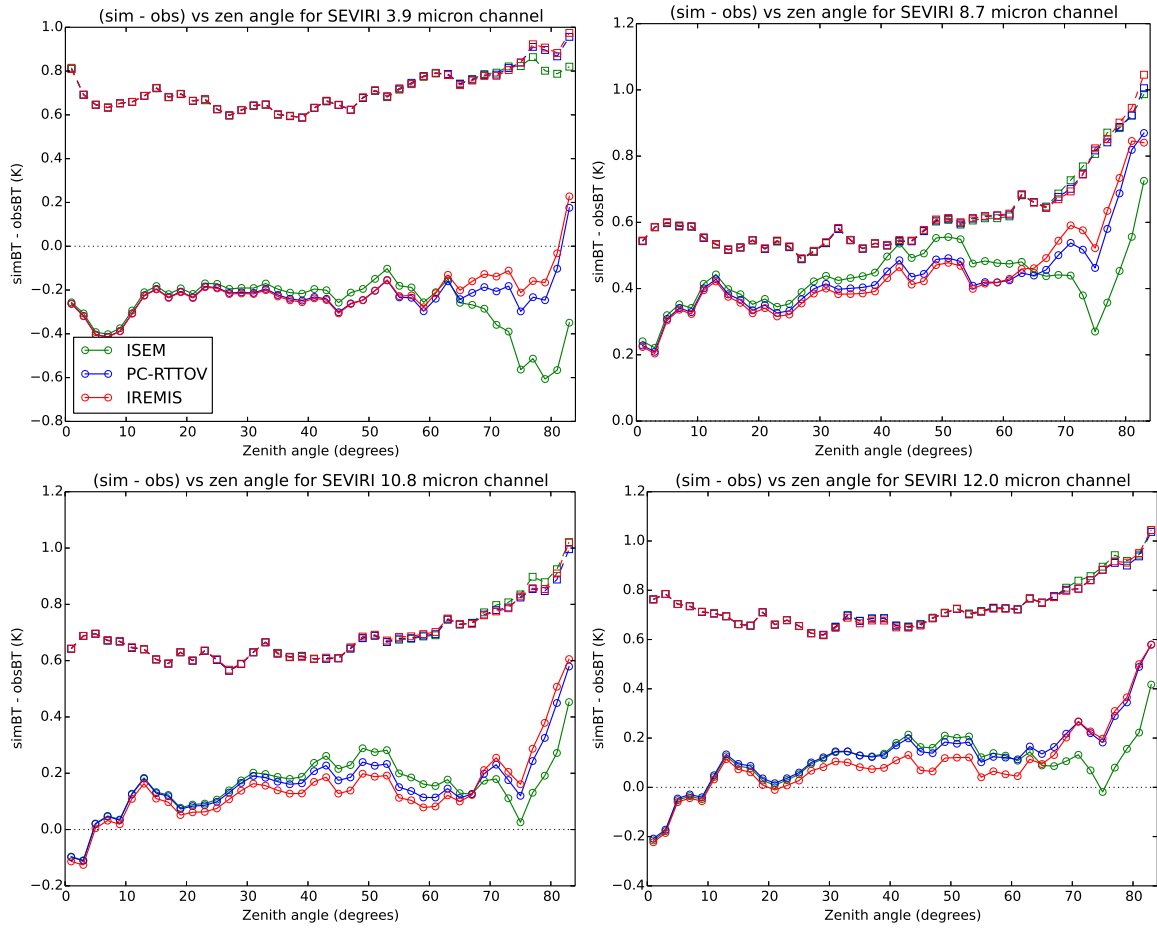


Figure 17: Showing the mean (solid) and standard deviation (dashed) of simulated minus observed brightness temperatures against zenith angle for ISEM, the PC-RTTOV emissivity model and IREMIS.

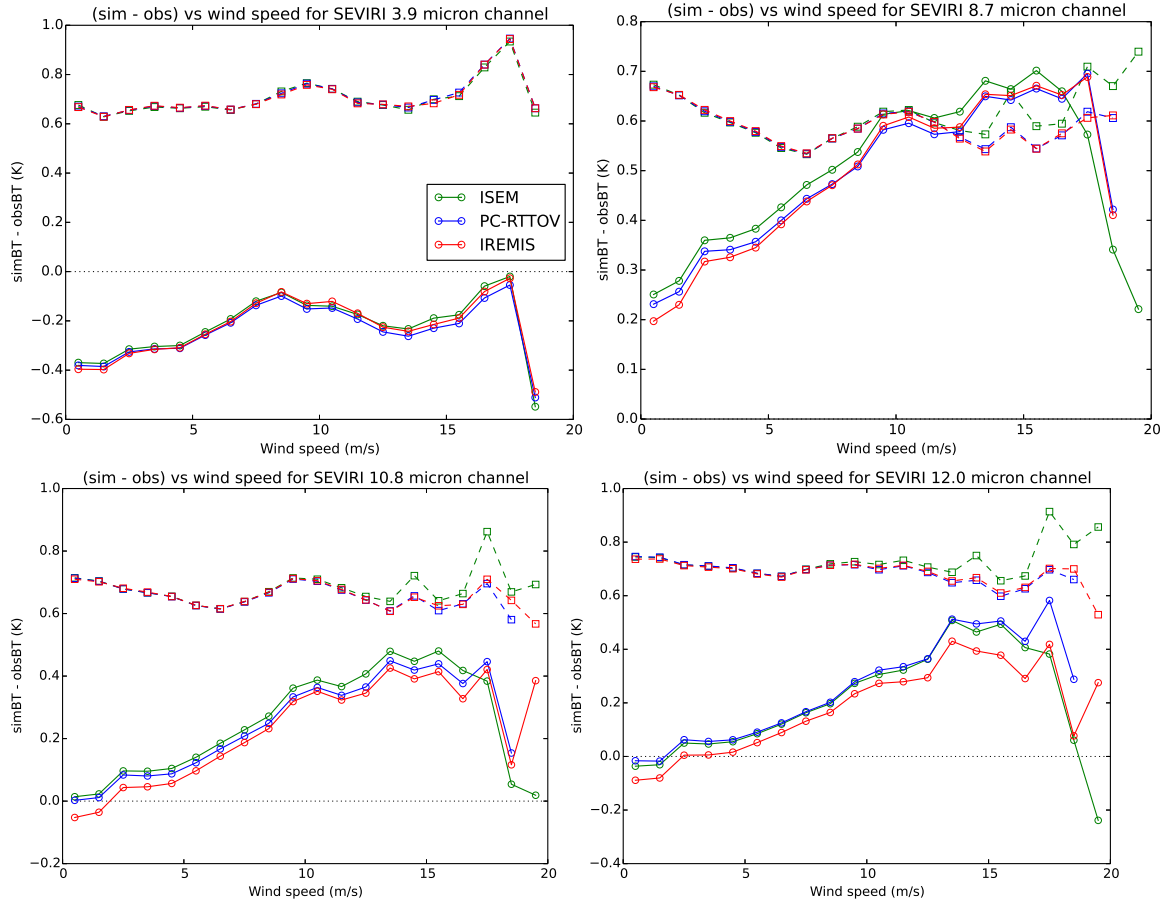


Figure 18: Showing the mean (solid) and standard deviation (dashed) of simulated minus observed brightness temperatures against wind speed for ISEM, the PC-RTTOV emissivity model and IREMIS.

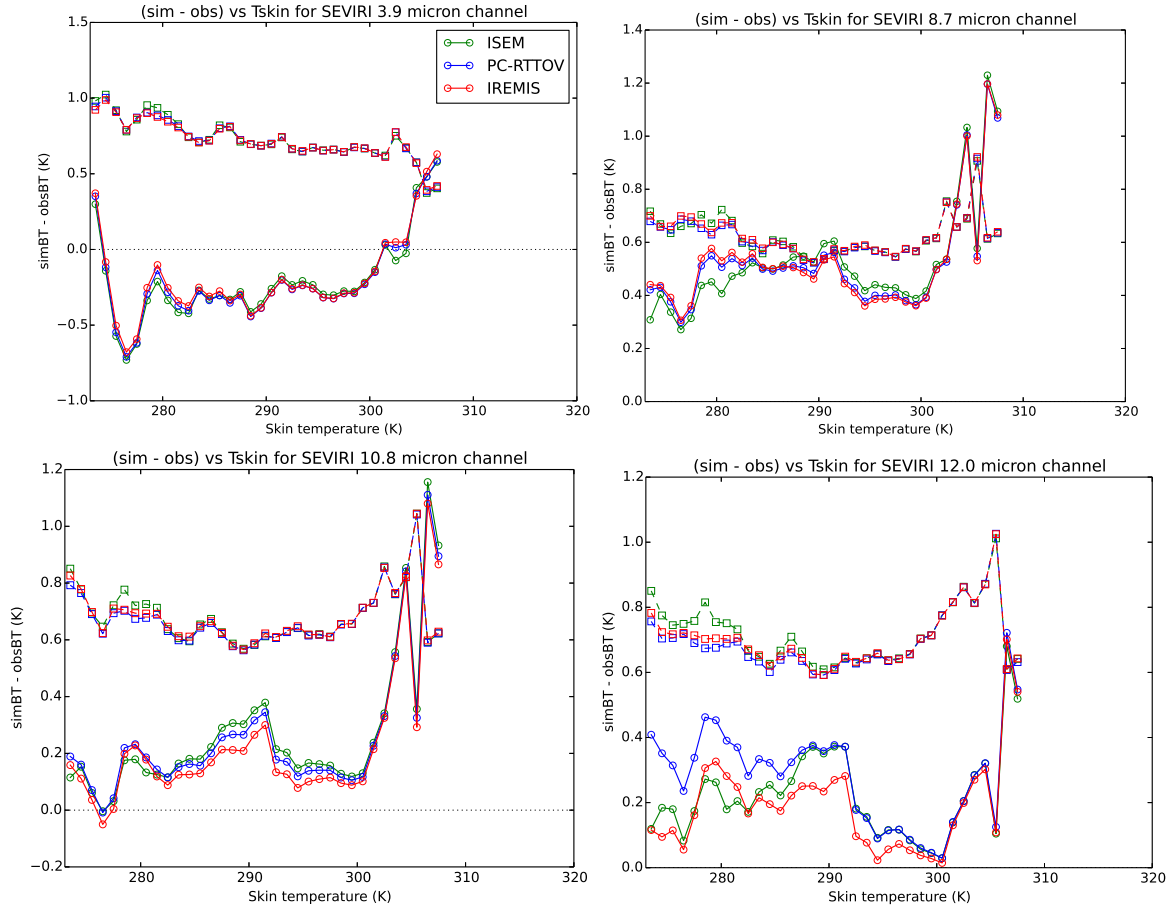


Figure 19: Showing the mean (solid) and standard deviation (dashed) of simulated minus observed brightness temperatures against skin temperature for ISEM, the PC-RTTOV emissivity model and IREMIS.

|   |   |   |   |
|---|---|---|---|
| <p>The EUMETSAT<br/>Network of<br/>Satellite Application<br/>Facilities</p> |  | <p>RTTOV-12 Science and<br/>Validation Report</p> | <p>Doc ID : NWPSAF-MO-TV-41<br/>Version : 1.0<br/>Date : 16/02/2017</p> |
|---|---|---|---|

## 2.6.2 Improved treatment of sea surface reflectance for solar radiation

RTTOV-9 introduced a sun-glint model for calculating the BRDF for the direct solar beam reflected by a wind-roughened water surface (Matricardi, 2003). Originally this was used to treat solar radiation in short-wave IR (SWIR) channels and in RTTOV-9 and 10 this model is used to provide the BRDF for the direct surface-reflected solar beam while for downward-scattered radiation (the single-scattering contribution due to aerosols and/or clouds) the surface BRDF was taken as  $(1-emissivity)/\pi$  which is consistent with the treatment of the downwelling atmospheric emission.

RTTOV-11 introduced the capability to simulate visible and near-IR channels and the sun-glint model was applied to these channels for the direct surface-reflected solar beam. In the absence of better information, the same sun-glint BRDF was used for the downward-scattered radiation (due to Rayleigh scattering and/or the single-scattering treatment of clouds/aerosols). The BRDF for downward-scattered SWIR radiation was changed (in error) to also use the sun-glint BRDF.

One problem with this treatment of sea-surface reflectance is that the sun-glint model gives BRDF values very close to zero away from sun-glint which results in an underestimation of the top-of-atmosphere reflectance. The RTTOV BRDF atlas includes fixed reflectance spectra for ocean and fresh water taken from the USGS spectral reflectance library (Clark *et. al.*, 2007). Users have requested that RTTOV make use of these spectra alongside the sun-glint model in order to improve the surface BRDFs used away from sun-glint-affected regions.

RTTOV-12 makes the following changes to the treatment of sea surface reflectance for solar radiation:

- BRDFs derived from the USGS reflectance spectra interpolated to the channel central wavenumber are added to the BRDFs returned by the sun-glint model: these BRDFs are used for the direct surface-reflected solar beam in all solar-affected channels.
- In SWIR channels the surface BRDF used for downward-scattered radiation by aerosols/clouds is calculated as  $(1-emissivity)/\pi$  as in RTTOV v9 and v10. This applies to the single-scattering calculation.
- In visible/near-IR channels the BRDF used for downward-scattered radiation is taken from the USGS spectra for fresh or ocean water. This applies to the single-scattering calculations for Rayleigh scattering and aerosols/clouds.
- As described in section 2.4 the new DOM scattering algorithm treats the surface as strictly Lambertian. In this case the same reflectance is used for both the direct solar beam and downward-scattered solar radiation.

The treatment for land and sea-ice surfaces and for channels where the user provides an input BRDF remains the same as in RTTOV-11: the same BRDF is used for the direct solar beam and for the downward-scattered radiation. Where RTTOV is requested to provide the BRDF it uses fixed values for visible/near-IR channels while for SWIR channels the BRDF is calculated as  $(1-emissivity)/\pi$ .

Figure 20 illustrates the impact of these modifications through comparisons of simulated and observed top-of-atmosphere (ToA) reflectances over a selection of 7 SEVIRI images at different times of day ranging between 6UTC and 18UTC: it shows histograms of the reflectance differences resulting from using the old RTTOV-11 sea BRDFs and the new v12 sea BRDFs. The differences are for clear-sky pixels over sea. Table 2 summarises the statistics for these plots: there is a reduction in bias by a factor of approximately 2-3 in all three channels and only small increases in standard deviation.

If the comparison is restricted to pixels within the sun-glint region there is an increase in the bias: simulated reflectances are too large on average with both models in all three channels and the bias increases by a factor of approximately 2-3 (not shown) with the v12 model. This is similar to the relative decrease in the bias when all pixels are considered. The standard deviations decrease very slightly with the v12 model. Improving the sea surface BRDF model is a candidate for future development in RTTOV.

| Channel                     | Mean v11 | Mean v12 | Std dev v11 | Std dev v12 |
|-----------------------------|----------|----------|-------------|-------------|
| <b>0.6<math>\mu</math>m</b> | -0.0272  | -0.0130  | 0.0405      | 0.0411      |
| <b>0.8<math>\mu</math>m</b> | -0.0257  | -0.0111  | 0.0428      | 0.0431      |
| <b>1.6<math>\mu</math>m</b> | -0.0216  | -0.0069  | 0.0362      | 0.0363      |

*Table 2: mean and standard deviations for the ToA reflectance differences shown in Figure 20.*

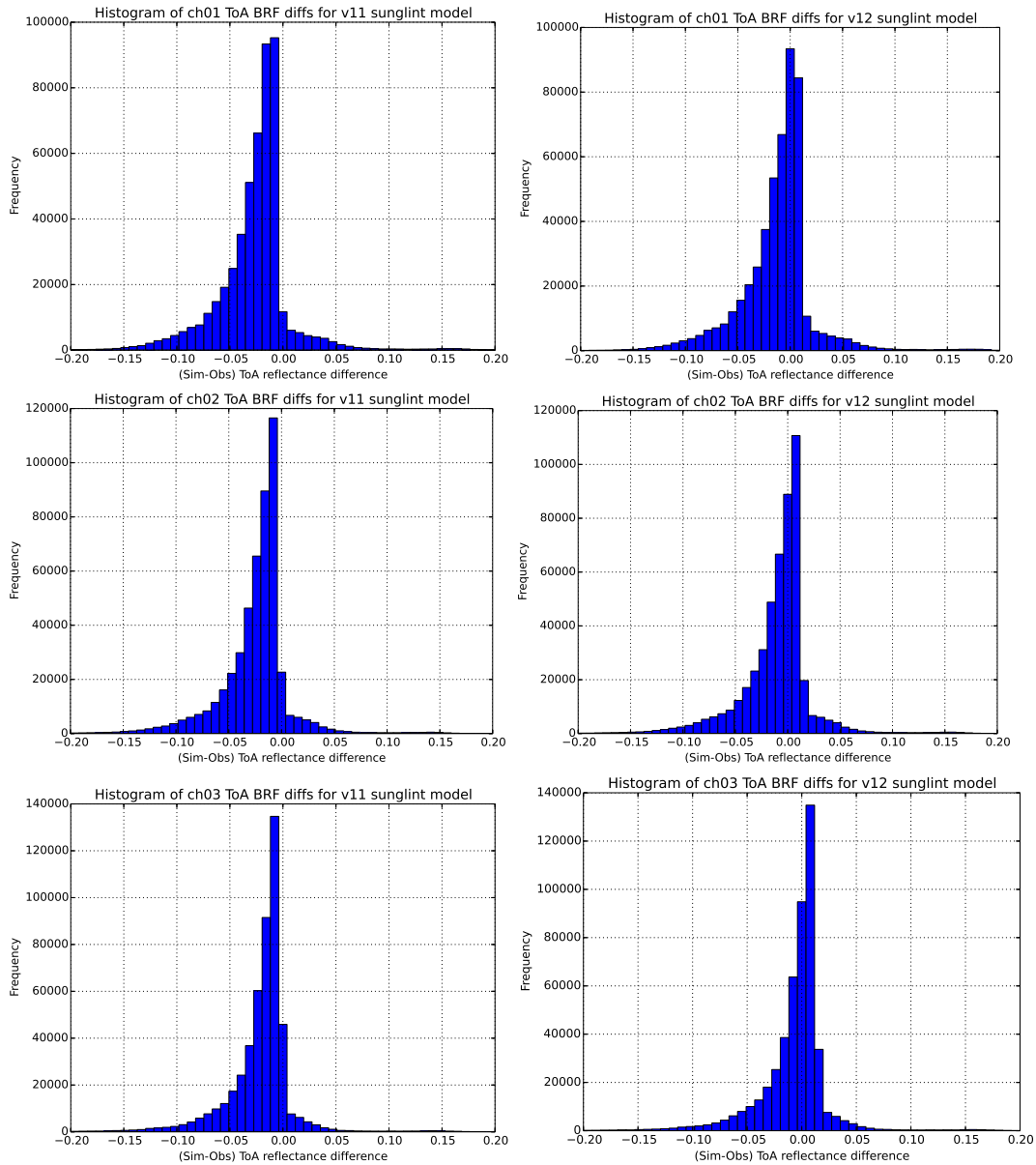


Figure 20: histograms of top-of-atmosphere clear-sky simulated minus observed reflectances for SEVIRI channels 1-3 ( $0.6\mu\text{m}$ ,  $0.8\mu\text{m}$  and  $1.6\mu\text{m}$  respectively). Only pixels over sea are considered. The left hand column shows differences to observations using the RTTOV-11 sea surface BRDFs and the right hand column uses the RTTOV-12 BRDFs (note that RTTOV-12 was used for all simulations: the only difference is in the sea surface BRDF calculation).

### 2.6.3 Updated land surface atlas

In RTTOV-12, the so-called NASA MEaSUREs combined ASTER and MODIS Emissivity over Land (CAMEL) emissivity database (<http://cimss.ssec.wisc.edu/iremisis/>), the updated version of the UWIREMIS database, has been implemented as an option alongside the

|  |  |   |  |
|--|--|---|--|
|  |  | <h2>RTTOV-12 Science and Validation Report</h2> | Doc ID : NWPSAF-MO-TV-41<br>Version : 1.0<br>Date : 16/02/2017 |
|--|--|---|--|

UWIREMIS atlas. The CAMEL database has been created by merging the UW MODIS-based emissivity database (UWIREMIS) developed at the University of Wisconsin-Madison, and the monthly ASTER Global Emissivity Dataset (ASTER GED v4) produced at JPL. The new CAMEL database was integrated to capitalize on the unique strengths of each products' spatial and spectral characteristics in the infrared region.

A limitation of the UWIREMIS database is that the emissivity in the TIR region (8-12  $\mu\text{m}$ ) is not well defined because MODIS only has 3 bands in this region (bands 8.5, 11 and 12  $\mu\text{m}$ ). This results in imperfect thermal IR spectral shape in the two quartz doublet regions at 8.5 and 12  $\mu\text{m}$ . The advantages are its moderate spatial resolution (5km), its uniform temporal coverage (monthly), and the fact that its emissivities span the entire IR region (3.6-12  $\mu\text{m}$ ). A disadvantage of the ASTER-GED dataset is that although there are more bands to more accurately define the spectral shape in the TIR region (5 bands, 8-12  $\mu\text{m}$ ), there are no bands in the mid-wave Infrared (MIR) region around 3.8-4.1  $\mu\text{m}$ , which limits its use in models and other atmospheric retrieval schemes. The advantages are its high spatial resolution (~100m) and high accuracy over arid regions.

The CAMEL database is available globally for the period 2003-2015 at 0.05 degree (~5km) resolution in mean monthly time-steps and for 13 bands from 3.6-14.3 micron. Similar to the concept of the land IR emissivity module of RTTOV-10 and RTTOV-11, the RTTOV-12 IR emissivity module (*mod\_camel\_atlas.F90*) consists of the CAMEL database for only one year, 2007. This year represents the entire data record well and it has the most consistent record of good observations. The IR emissivity module creates a high spectral emissivity on 417 wavenumbers using a Principal Component Analyses (PCA) regression, described in *Borbos and Ruston (2010)* and *Borbos (2014)* but with the following changes: the number of Principal Components (PCs) now vary from 2 to 9, based on the surface scene type and coverage; the original spatial resolution has been kept (0.05 degree grid); three sets of laboratory measurements have been created for the PCA regression based on the surface scene type and coverage (general, arid and snow/ice) (*Borbos et. al., 2017a; Borbas et. al., 2017b*). Table 3 summaries these main differences between the two modules. *Borbos et. al. (2017a)* also contains validation results using IASI observations, other emissivity atlases and in situ measurements.

The geographical locations where improvements can be expected are over snow/ice surfaces, non-vegetated, bare soil, sand and rock surfaces (including quartz and carbonates). As a validation, IASI observed brightness temperatures were compared to the calculated ones using (1) the RTTOV UW IR emissivity module based on the UW BF emissivity database and (2) a new CAMEL module based on the combined NASA MEASUREs CAMEL emissivity database. The de-biased variance over the 3.6-5, 8-9 and 10-13  $\mu\text{m}$  spectral regions are calculated and used as the indicator for a better emissivity estimate. Figures 21A and 21B illustrate a IASI granule at 17:56:56 UTC on 29 Sept 2008, where the CAMEL emissivity improves the brightness temperature calculation over the Arabian Peninsula.

A spatial variance estimate of the IR emissivity is planned for a future version of the CAMEL database for each month for the same 0.5x0.5 degree grid as is in RTTOV-10 and RTTOV-11 and on the full 417 spectral resolution.

|                            | <b>RTTOV10/11<br/>UWIREMIS</b>   | <b>RTTOV12<br/>MEaSURES CAMEL</b>   |
|----------------------------|--|---|
| <b>Inputs:</b>             | MODIS MYD11(6)<br>MODIS-ASTER Lab  | UWIREMIS BF (10)<br>ASTER-GED v4 (5)<br>MODIS-ASTER Lab   |
| <b>Method:</b>             | Baseline Fit Conceptual<br>model<br>PCA Regression                       | Conceptual model<br>PCA Regression  |
| <b>Spatial Resolution:</b> | 0.1°/10km  | 0.05°/5km   |
| <b>Laboratory data:</b>    | 123 selected MODIS-ASTER   | 55 general lab set<br>82 general+carbonates<br>4 ice/snow labset                                      |
| <b>Number of PCs</b>       | 6  | 2,7 or 9, varies by surface types based on the 8.6 μm ASTER emis, ASTER NDVI, and MODIS Snow Fraction |
| <b>Outputs:</b>            | Emissivity spectra on 10 BF hinge point and 417 HSR points (3.6-14.3 μm) | Emissivity spectra on 13 hinge point and 417 HSR points (3.6-14.3μm) NDVI, Snow Fraction              |

*Table 3. Summary of the main differences between the UWIREMIS (RTTOV-11) and the MEASURES CAMEL (RTTOV-12) IR land surface emissivity database.*

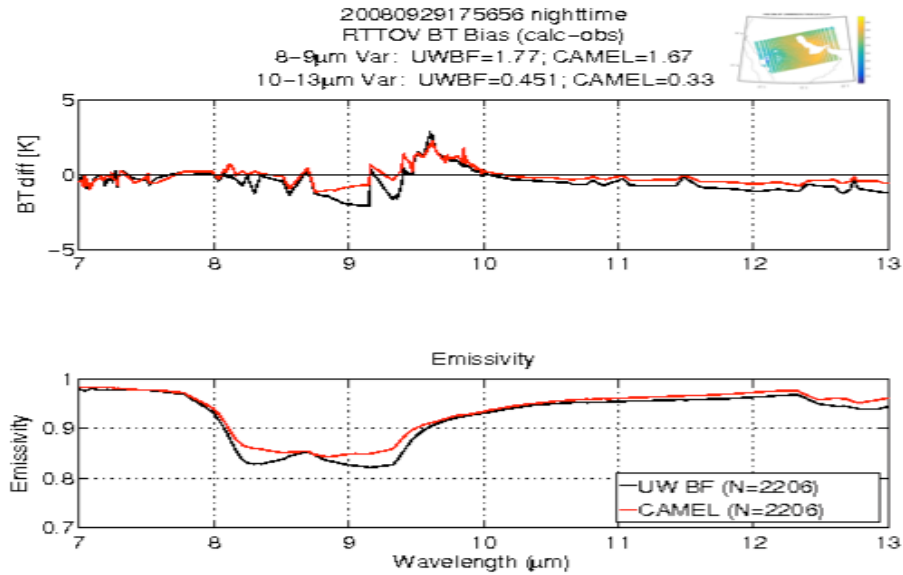


Figure 21A: IASI observed brightness temperatures are compared to the calculated ones using the RTTOV UW IRemis module based on the UW BF emissivity Database (black) and the combined NASA MEASURES CAMEL emissivity database (red) for the granule at 17:56:56 UTC, on Sept 29, 2008. The de-biased Variance over the 8-9 and 10-13  $\mu$ m spectral region are included in the title.

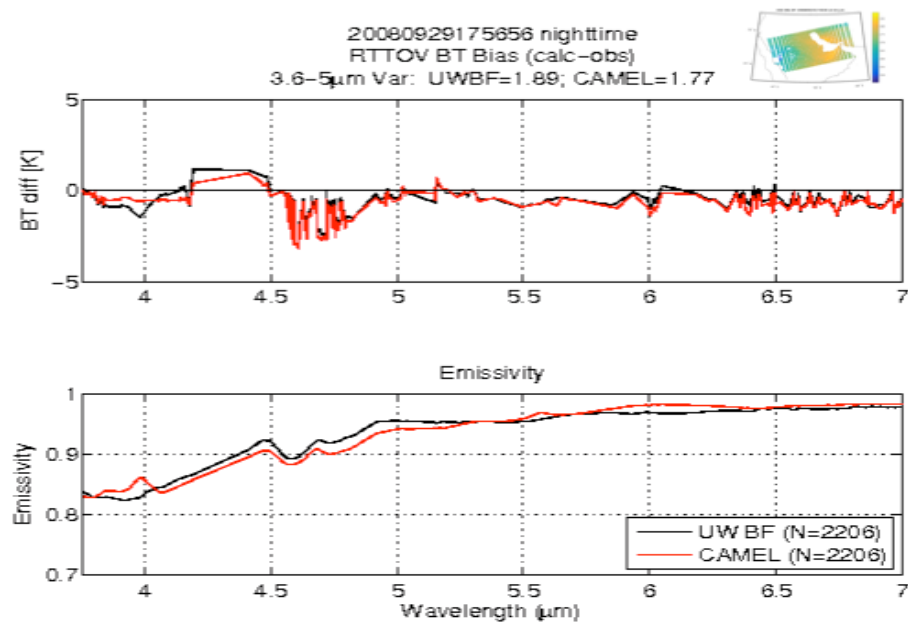


Figure 21B, same as Figure 21A, but for the short IR spectral region (between 3.6 and 7  $\mu$ m).

|   |   |   |   |
|---|---|---|---|
| <p>The EUMETSAT<br/>Network of<br/>Satellite Application<br/>Facilities</p> |  | <p>RTTOV-12 Science and<br/>Validation Report</p> | <p>Doc ID : NWPSAF-MO-TV-41<br/>Version : 1.0<br/>Date : 16/02/2017</p> |
|---|---|---|---|

## 2.7 Microwave ocean and land surface emissivity

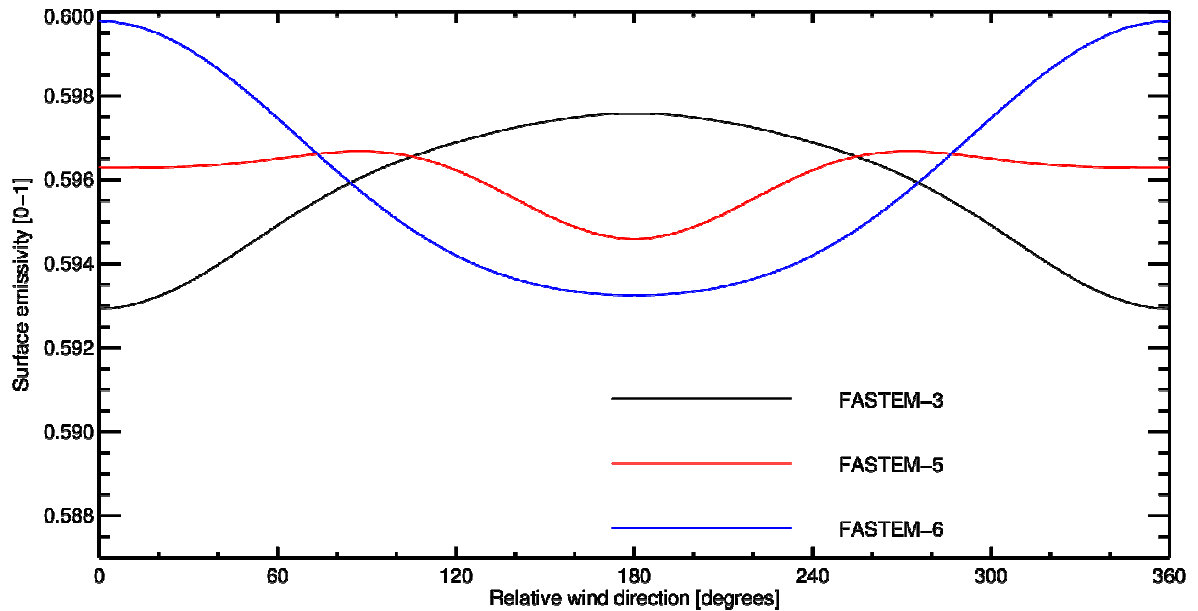
### 2.7.1 FASTEM-6 update

FASTEM-6 has been available in RTTOV since the RTTOV v11.2 release and it will become the default with RTTOV-12. The only change from FASTEM-5 to FASTEM-6 is the relative wind direction (RWD) correction. The other components (e.g. foam and whitecap coverage and large- and small-scale roughness) are the same as in FASTEM-5. FASTEM-6 was developed and tested by Kazumori and English (2015). For frequencies between 6 GHz and 37 GHz they derived the RWD direction correction observationally using matchups between ADEOS-II scatterometer winds and AMSR observations. At 92 GHz they used ECMWF model winds and SSMIS observations. To model the dependence at zenith angles other than AMSR (53.1°), they adopted the incidence angle dependence of Meissner and Wentz (2012). Here we present a summary for RTTOV users and some additional notes on the validity range of FASTEM-6 and previous FASTEM versions.

FASTEM-3 was the first version of FASTEM to introduce a RWD dependence. This was subsequently updated in FASTEM-5 and then again for FASTEM-6. Figure 22 illustrates emissivity values produced by these three models. The RWD dependence is broadly consistent between different versions in the h-polarisation but there are big discrepancies in the v-polarisation. As discussed by Kazumori and English (2015), the relative wind direction definition in FASTEM-3 is 180° different to that in the subsequent models hence, it is no longer correct to use the FASTEM-3 RWD model in the RTTOV framework. This error shows up as a 180° offset in the FASTEM-3 results compared to FASTEM-6. Also, the RWD model of FASTEM-5 does not appear to have been implemented correctly in RTTOV, which is again revealed by the incorrect shape of its RWD dependence in Fig. 22a. Its implementation in CRTM is more correct. Hence, neither FASTEM-3 nor FASTEM-5 should be used in RTTOV unless their RWD dependence is deactivated. A final advantage of FASTEM-6 compared to the other models is that the earlier versions had an unphysical dependence on RWD even at zero wind speed, whereas in FASTEM-6 there is none.

Kazumori and English (2015) showed that moving from FASTEM-5 to FASTEM-6 substantially improved the agreement between ECMWF simulations and observed microwave imager brightness temperatures. They also tested the cross-track sounder AMSU-A for which there was little difference between the two FASTEM versions, showing that the chosen zenith angle dependence works well. However, two areas were not tested in their study: frequencies above 90 GHz, and the polarimetric channels of Windsat. The latter are not supported by FASTEM-6 which means that Windsat users should retain FASTEM-5 despite its issues.

a)



b)

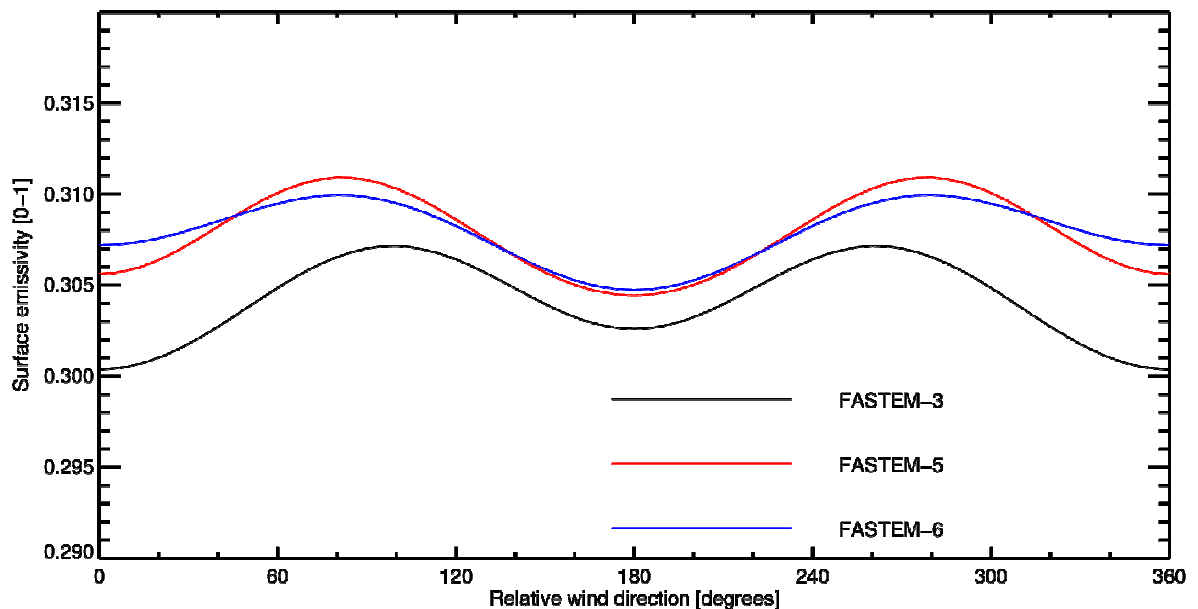


**Figure 22:** 19 GHz emissivity generated by FASTEM versions 3, 5 and 6 in RTTOV version 11.2, for a representative profile with a 10m windspeed of  $10 \text{ ms}^{-1}$  at a typical microwave imager zenith angle of  $53.1^\circ$ : (a) vertical polarisation; (b) horizontal polarisation.

Figure 23 explores the validity at higher frequencies by looking at the first guess departures for all SSMIS h-polarised window channels in recent ECMWF pre-operational

analyses, where FASTEM-6 is used. At lower frequencies these results are consistent with Kazumori and English (2015), showing that FASTEM-6 probably still slightly underestimates the RWD dependence, although this residual error is small compared to the RWD effect itself. At 92 and 150 GHz, FASTEM-6 appears to slightly overestimate the RWD dependence, although any errors are fairly consistent between the two frequencies. This shows that it is acceptable to use the RWD model derived at 92 GHz at higher frequencies. Note that the mean positive departures at these two frequencies are the result of inadequate bias correction and are not related to the RWD model.

In summary, FASTEM-6 is recommended for almost all users. It brings substantial benefits to microwave imager simulations compared to previous versions, and it is valid across the microwave frequency range and for cross-track sounders like AMSU-A. FASTEM-3 and FASTEM-5 should no longer be used unless the RWD dependence is deactivated. The only exceptions are, first, if a user requires the simulation of Windsat polarimetric channels, FASTEM-5 must be used; second, this testing excludes sub-mm frequencies (i.e. above 200 GHz on the future ICI instrument) for which development is still ongoing. The TESSEM2 model can be used for channels above 200GHz (see next section).

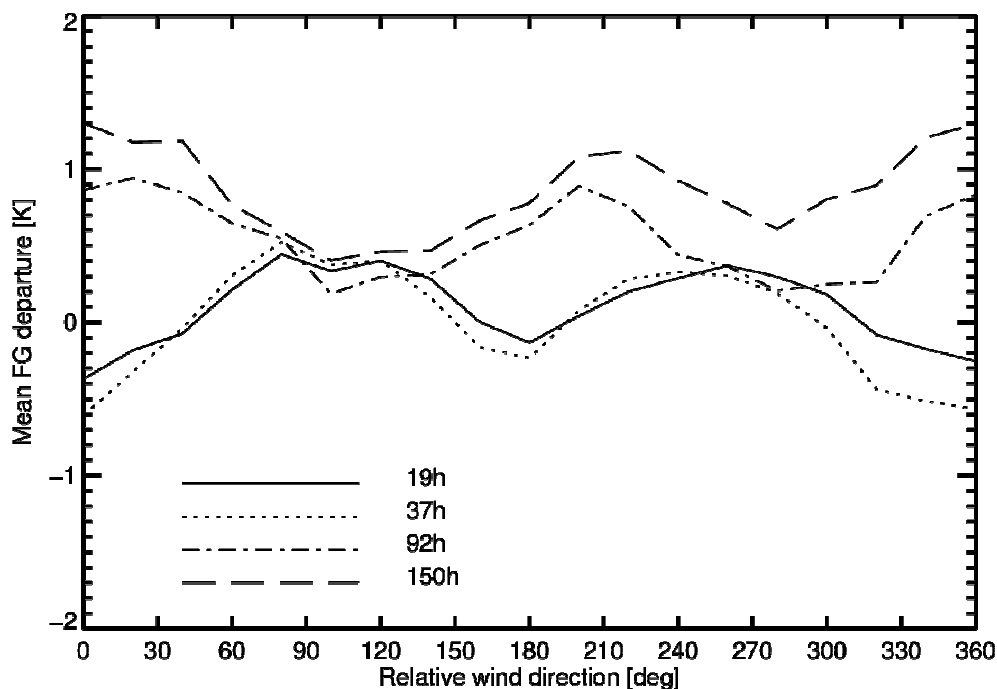


**Figure 23:** First guess departures binned by RWD for SSMIS F-17 h-polarised window channels, based on observations monitored in the ECMWF pre-operational forecast system (esuite) between 10 August and 9 October 2016. Sample is for clear-skies, ocean surfaces only (avoiding sea-ice) and for model wind speeds greater than  $10\text{ms}^{-1}$ .

|   |   |   |   |
|---|---|---|---|
| <p>The EUMETSAT<br/>Network of<br/>Satellite Application<br/>Facilities</p> |  | <p>RTTOV-12 Science and<br/>Validation Report</p> | <p>Doc ID : NWPSAF-MO-TV-41<br/>Version : 1.0<br/>Date : 16/02/2017</p> |
|---|---|---|---|

## 2.7.2 TESSEM2

To provide a fast parameterised model for sea surface emissivity TESSEM2 (Tool to Estimate the Sea Surface Emissivity at Microwaves and Millimeter waves) was developed that fits as close as possible FASTEM-6 in its range of validity (up to 190 GHz and for angles up to 60deg), and that smoothly transitions to the physical model for larger angles and for higher frequencies. The new TESSEM2 model (Prigent *et al*, 2016) extends the range for MW sea surface emissivity calculations up to 700 GHz. In particular it is intended to be useful for the proposed EPS Second Generation ICI instrument. It is based on FASTEM-6 (see above) for frequencies up to 200 GHz and it uses a physical emissivity model at higher frequencies. In RTTOV it is recommended that users select FASTEM-6 for channels below 200 GHz and TESSEM2 for channels above 200 GHz.

Above 200 GHz a physical geometric optics model has been developed, with the sea surface described as a set of flat surfaces with a bi-directional slope distribution, derived from photographic observations of the sun glitter on the sea. The model does not account for the small scale roughness as this is expected to only be significant at low frequencies. The higher the frequency, the more valid the geometric optics approach is making this model suitable for the millimetre to submillimetre frequencies. It uses the FASTEM-6 values for the dielectric properties of sea water, for the foam cover, and for the foam emissivity. The sea water dielectric properties used in FASTEM are based on a large range of measurements of pure and sea water from 1.7 to 410 GHz. Above 410 GHz, the frequency dependence of the water dielectric properties is expected to be smooth, and extrapolation of the model should be realistic.

A neural network parameterisation was adopted to represent the multi-variate and non-linear behaviour of the sea surface emissivity. It has 5 inputs in its input layer corresponding to the model (frequency, incidence angle, wind speed, sea surface temperature, and salinity), 15 neurons in the hidden layer, and 2 outputs, corresponding to the two orthogonal polarizations of the emissivities. Prigent *et. al.*, (2016) give more details of the model and its preliminary validation.

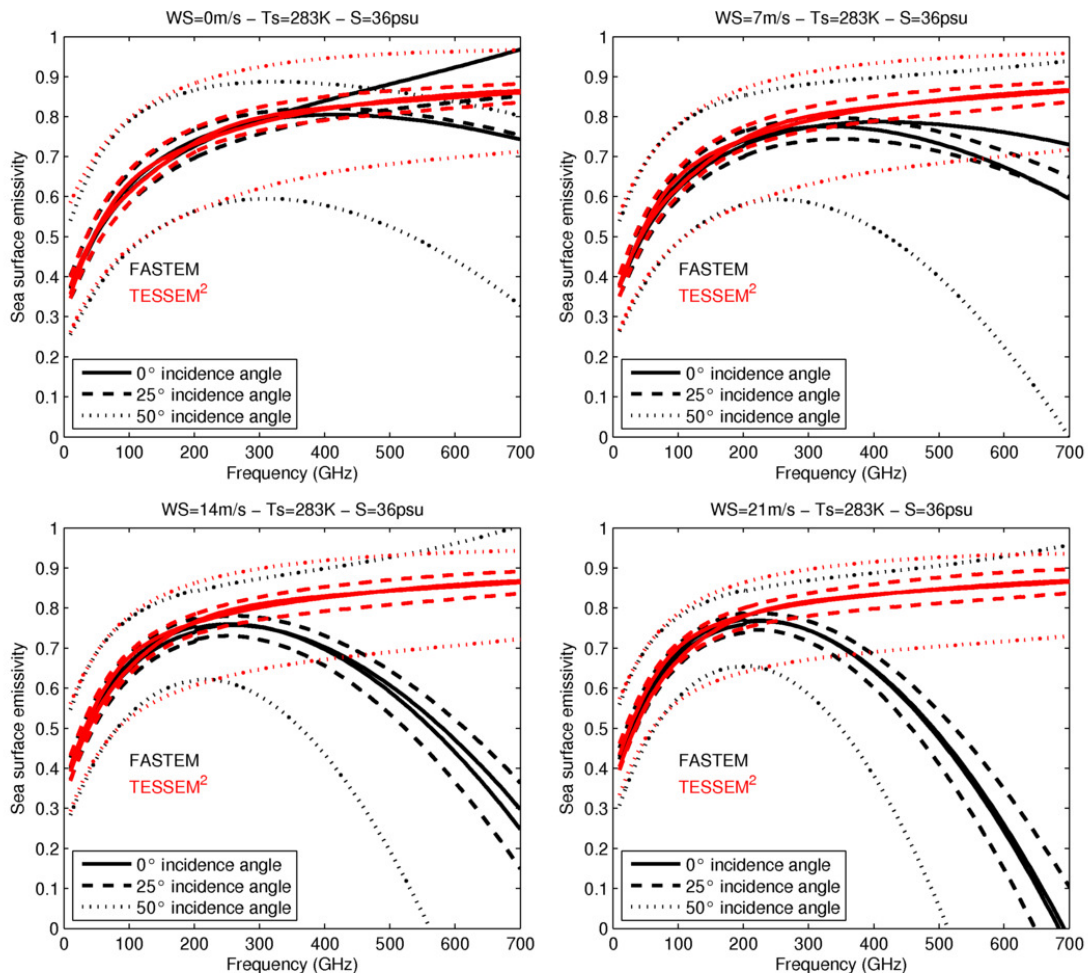


Figure 24. The emissivity frequency dependence for 3 incidence angles (0, 25, 50 deg), for 4 wind speeds with a surface temperature at 283K and a salinity of 36 psu. TESSEM2 in red and FASTEM-6 in black.

A comparison of the TESSEM model with FASTEM-6 is presented in Figure 24 over the frequency range 10-700 GHz for several wind speeds and incidence angles. Below 200 GHz the differences between the two models are very small and so FASTEM-6 can be used. Above 200 GHz the two models diverge especially for high wind speeds and it is recommended TESSEM2 be used at frequencies above 200 GHz.

### 2.7.3 TELSEM2

The TELSEM MW emissivity atlas and interpolator introduced in RTTOV-10 has been updated for RTTOV-12. The new atlas (Wang *et al.*, 2016) gives very similar land surface emissivities to the previous version for channels in the range 10-200GHz, but now includes an improved extrapolation for higher frequencies such that it may be used for channels above 200 GHz (e.g. for the EPS-SG ICI instrument).

|   |   |   |   |
|---|---|---|---|
| <p>The EUMETSAT<br/>Network of<br/>Satellite Application<br/>Facilities</p> |  | <h2 style="text-align: center;">RTTOV-12 Science and<br/>Validation Report</h2> | <p>Doc ID : NWPSAF-MO-TV-41<br/>Version : 1.0<br/>Date : 16/02/2017</p> |
|---|---|---|---|

The frequency dependence of the emissivities above 100 GHz has been analyzed by Wang *et. al*, (2016), based on a joint analysis of the SSM/I TELSEM database, SSMIS and AMSU-B MétéoFrance estimates, and the 143 SSMIS NOAA emissivities from the Microwave Integrated Retrieval System (MIRS). In addition the updated atlas now includes emissivities for climatological sea-ice and continental snow and ice cover. Depending on its type (new ice, first-year ice, or multi-year ice), sea ice exhibits various emissivity behaviours, related to differences in dielectric and scattering properties. With age, the ice thickness increases, its salinity decreases, and the potential snow cover changes. These sea ice emissivities were not included in the first version of TELSEM, and the database is now updated in TELSEM2 to add the sea ice component.

TELSEM2 has been evaluated up to 325 GHz with the observations of the International Sub-Millimeter Airborne Radiometer (ISMAR) and the Microwave Airborne Radiometer Scanning System (MARSS) which were operated on board the Facility for Airborne Atmospheric Measurements (FAAM) aircraft during the COSMICS (Cold-air Outbreak and Sub-Millimeter Ice Cloud Study) campaign over Greenland. Over land the agreement was consistent with measurements from 89-157 GHz but over sea-ice the agreement was less clear.

An example of the TELSEM2 emissivities are shown in the map plots in Figure 25 showing two different frequencies at 85 GHz and 243 GHz for both polar regions for the sea-ice and the land areas.

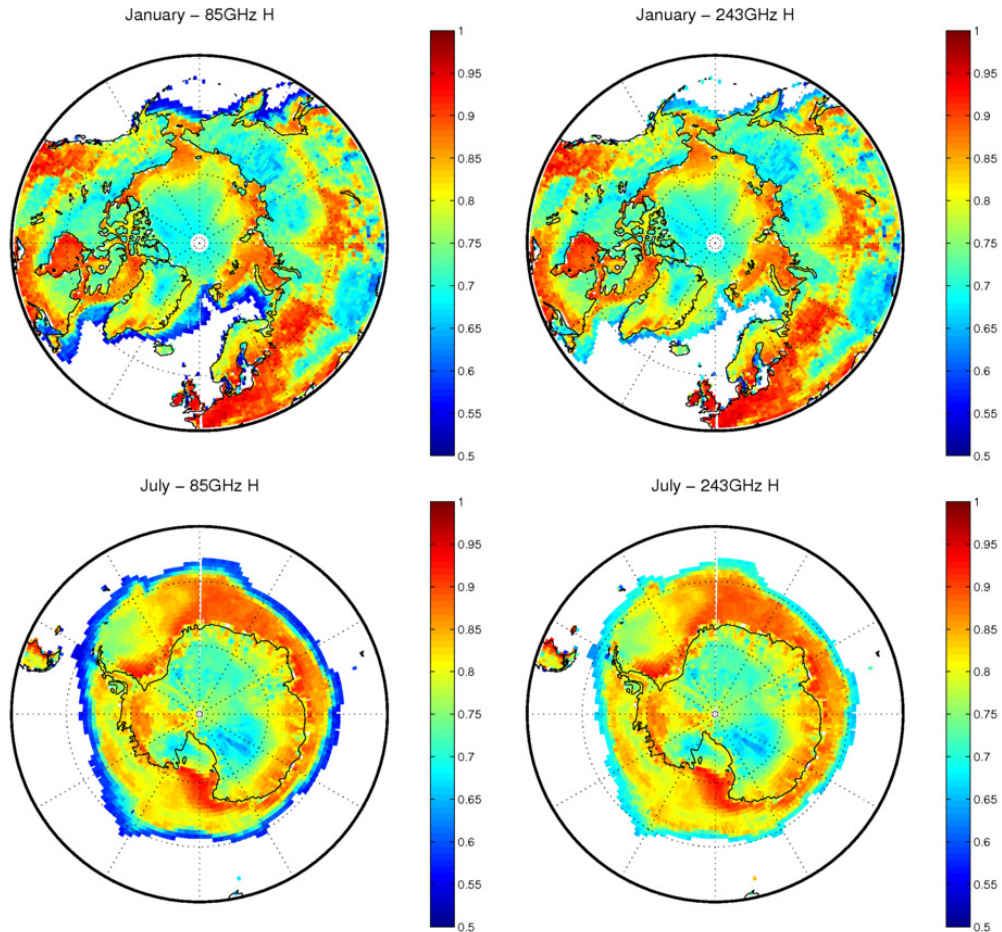


Figure 25. The TELSEM2 emissivities for the Arctic in January (top) and for the Antarctic in July (bottom) at 85 GHz h polarisation (left) and at 243 GHz h polarisation (right). It includes the continents as well as sea-ice.

#### 2.7.4 CNRM Atlas

The CNRM microwave emissivity atlas introduced in RTTOV-10 (Karbou *et. al.* 2006; Karbou *et. al.* 2010) has been updated for RTTOV-12. The new atlas contains emissivity estimates for new frequencies (different observing mode) and can be used for AMSU-A, AMSU-B/MHS, SSMI(S) and ATMS and the data are available for 2014 and 2015. The emissivity is derived using surface temperature and air temperature and humidity short range forecasts from the French global NWP model ARPEGE. The emissivities are provided for surface sensitive channels for AMSU-A (23, 31, 50 and 89 GHz, high and near nadir angles), AMSU-B/MHS (89 and 150/157 GHz, high and near nadir zenith angles), ATMS (23, 31, 50, 51, 89 GHz, high and near nadir zenith angles) and SSMI(S) (19H, 19V, 22V, 37H, 37V, 85V, 85H). The atlases give global coverage and are averaged over each month (from January 2014 to December 2015). No sea ice estimates are included. The spatial grid provided in the HDF5 files is 0.25x0.25 deg; and the ATMS atlas

|   |   |   |   |
|---|---|---|---|
| <p>The EUMETSAT<br/>Network of<br/>Satellite Application<br/>Facilities</p> |  | <p align="center"><b>RTTOV-12 Science and<br/>Validation Report</b></p> | <p>Doc ID : NWPSAF-MO-TV-41<br/>Version : 1.0<br/>Date : 16/02/2017</p> |
|---|---|---|---|

is provided in both 0.25x0.25deg and 0.5x0.5deg grids (the use of 0.5x0.5 deg grid is recommended for ATMS to avoid gaps).

## 2.8 PC-RTTOV updates

PC-RTTOV coefficient files are now available which have been trained over all surface types. Over land, the training has been performed using the University of Wisconsin IR land surface emissivity atlas. In principle, PC-RTTOV calculations should be carried out using emissivities that reflect the configuration used to train the coefficients. However as the new PC-RTTOV training encompasses a wide range of surface emissivities, the use of alternative physically realistic sources for surface emissivity should be acceptable.

PC-RTTOV has been extended to include simulations that can include a non-LTE correction to the TOA radiances (see section 2.10). The NLTE version of PC-RTTOV has been trained over all surface types and can be used to include NLTE effects in the spectral region at 4.3  $\mu\text{m}$  for solar zenith angles between 0 and 90 degrees for the entire viewing geometry of IASI.

## 2.9 Addition of HT-FRTC

A new option included with RTTOV-12 is the Havemann Taylor Fast Radiative Transfer Code (HT-FRTC) which can be used from microwave to ultraviolet wavelengths to calculate transmittance, radiance and radiative flux spectra, as represented by principal components (PCs). The PCs cover the spectrum at a very high spectral resolution, which allows very fast monochromatic, hyper-spectral and broadband simulations for satellite-based, airborne and ground-based sensors. The PCs are derived during a code training phase from monochromatic simulations for a diverse set of atmosphere and surface conditions. They are sensor independent, which means no extra training is required to include additional sensors. HT-FRTC has been trained with all 50 trace gases that are included in the HITRAN database and can be run by specifying vertical profiles for any combination of these gases. It has been trained with a large variety of surface emissivity / reflectance spectra and can be run for any Lambertian or specular surface. Scattering by frozen or liquid cloud and precipitation and also for 12 different aerosol species as well as Rayleigh scattering, which is significant in the short-wave, has been included. The scattering phase function can be fully accounted for by an integrated monochromatic version of the Edwards-Slingo (ES) spherical harmonics radiation code or by calling DISORT. An approximation to scattering using a modification to the extinction (Chou scaling) can also be selected. HT-FRTC uses monochromatic calculations at a small number of frequencies, which are selected by a k-means cluster algorithm during the training phase to predict the principal component scores.

RTTOV-12 provides the option to call the HT-FRTC model through a PC-RTTOV-like interface. Users can download the HT-FRTC package plus any necessary ancillary data files from the NWP SAF website and will then compile HT-FRTC. They can then link

|   |   |   |   |
|---|---|---|---|
| <p>The EUMETSAT<br/>Network of<br/>Satellite Application<br/>Facilities</p> |  | <h2 style="text-align: center;">RTTOV-12 Science and<br/>Validation Report</h2> | <p>Doc ID : NWPSAF-MO-TV-41<br/>Version : 1.0<br/>Date : 16/02/2017</p> |
|---|---|---|---|

RTTOV-12 against the HT-FRTC library when compiling RTTOV. To run the HT-FRTC code, a number of data files in netCDF format are also required as part of the distribution. They contain relevant gaseous optical properties. In this initial distribution, the functionality of HT-FRTC is restricted to the simulation of IASI spectra. As one of the features of the HT-FRTC code is that the code training stage, including the generation of Principal Components is general and does not contain any sensor specific information, it is fairly straight-forward to add additional files for the simulation of more infrared sounders like AIRS, CrIS or the future MTG-IRS. Another possible future addition might be the treatment of clouds and aerosols either with the fast Chou-scaling approximation, which is also used in RTTOV for the infrared part of the spectrum or with a slower, more exact full scattering solution based on a monochromatic version of the ES spherical harmonics code. A possible future addition could be the extension to cover the short-wave, near-infrared, ultraviolet or microwave. The HT-FRTC code does not only simulate satellite radiances, but also ground-based sensors looking up and air-borne sensors at any altitude both looking up and down. For all these potential future extensions to the distribution the required HT-FRTC source code and libraries are already contained in this distribution. What will be required is the extension of the interface routine which couples HT-FRTC with RTTOV. This will then make the additional functionality accessible. It will also require the necessary additional data files to be included in the distribution and made available to the user.

As a fast radiative transfer code based on PCs, HT-FRTC will be faster than classical RTTOV if more than about a 100 channels are calculated and at least as accurate. HT-FRTC and PC-RTTOV both use Principal Components for their calculations. A major difference between the two codes is that the HT-FRTC radiative transfer calculations are monochromatic, while PC-RTTOV (and RTTOV on which it is based) both perform polychromatic radiative transfer calculations for actual sensor channels that are simulated. Both approaches have pros and cons. For instance, if only a small number of relatively broad channels from instruments like AVHRR or HIRS are of interest, then an immediate calculation of the required polychromatic radiance will be the most direct route. In the hyperspectral scenario however, many radiative transfer calculations will be required and the cheaper monochromatic calculations provide a similar degree of information as the more demanding polychromatic calculations when the step from monochromatic radiances to polychromatic radiances is taken care of by the PCs themselves.

The sensor independent formulation of HT-FRTC has two related advantages. Since no sensor specific information enters the training stage, different assumptions regarding the apodisation are also irrelevant at the training stage and changes to the apodisation require very few changes. Also, if a number of infrared hyperspectral sounders are simulated with the same set of training data, then all the assumptions regarding the gaseous optical properties and potentially cloud and aerosol properties will be entirely consistent between all the different sounders. The initial version of HT-FRTC in RTTOV-12 has not been

|   |   |   |  |
|---|---|---|--|
|  |  | <h2>RTTOV-12 Science and Validation Report</h2> | Doc ID : NWPSAF-MO-TV-41<br>Version : 1.0<br>Date : 16/02/2017 |
|---|---|---|--|

optimised for run time however and so it is not recommended to use it for operational applications until the next version is released.

### 2.10 Updated non-LTE formulation

RTTOV is capable of estimating daytime Non-Local Thermodynamic Equilibrium (NLTE) effects in the CO<sub>2</sub> v3 band (around 4.3 μm). Here, local thermodynamic equilibrium breaks down due to the absorption of the strong solar radiation field. The effect can add around 10K to the measured brightness temperatures during the day. NLTE effects are introduced in the RTTOV calculations by adding a correction to the standard LTE RTTOV radiances for affected channels (between 2200 cm<sup>-1</sup> – 2400 cm<sup>-1</sup>) of high resolution IR sounders. The NLTE correction is computed using a predictor-based regression scheme (see Matricardi *et al.*; 2017) for details). The predictors consist of various combinations of the solar zenith angle, the sensor zenith angle, and the average kinetic temperature in two broad atmospheric layers above ~51 hPa. The NLTE algorithm has been trained using a database of accurate vibrational temperatures computed using the GRANADA NLTE population algorithm (Funke *et al.*, 2012).

The NLTE algorithm developed calculates the difference  $\Delta R_i^{NLTE} = R_i^{NLTE} - R_i^{LTE}$  between NLTE and LTE LBL radiances in channel  $i$  through a regression relation in which a set of profile-dependent predictors is governed by a set of channel-dependent coefficients:

$$\Delta R_i^{NLTE} = \sum_{j=1}^n X_{i,j} b_j \quad (2.10.1)$$

In Eq. (2.10.1),  $b_j$  are the predictors and  $X_{i,j}$  are coefficients that have been estimated by fitting Eq. (2.10.1) to a dataset of  $\Delta R_i^{NLTE}$  LBL radiances between 2200 cm<sup>-1</sup> ( $i=6221$ ) and 2400 cm<sup>-1</sup> ( $i=7021$ ). It should be noted that, although Eq. (2.10.1) is similar to the one utilised by DeSouza-Machado *et al.* (2006), in an effort to improve the skill of the model we have selected a different set of predictors, which we have tabulated in Table 4. It can be seen that the predictors consist of various combinations of the solar zenith angle ( $\theta_0$ ), the sensor zenith angle ( $\theta$ ) and the average kinetic temperatures in two broad atmospheric layers above 50 hPa ( $T_1^{av}$  is the average temperature between 0.005 hPa and 0.2 hPa and  $T_2^{av}$  is the average temperature between 0.2 hPa and 50 hPa). The predictors reflect the strong dependence of NLTE effects on solar zenith angle and the fact that deviations of vibrational temperatures from kinetic temperatures start becoming significant in the stratospheric layers above ~ 50 hPa.

| Predictor number | Predictors                        |
|------------------|-----------------------------------|
| 1                | constant                          |
| 2                | $\cos(\theta_0)$                  |
| 3                | $(\cos(\theta_0))^{0.5}$          |
| 4                | $\cos(\theta_0) \sec(\theta)$     |
| 5                | $(\cos(\theta_0) \sec(\theta))^2$ |
| 6                | $\cos(\theta_0) T_1^{av}$         |
| 7                | $\cos(\theta_0) T_2^{av}$         |
| 8                | $\sec(\theta) T_1^{av}$           |
| 9                | $\sec(\theta) T_2^{av}$           |

Table 4: The predictors used in the fast NLTE algorithm

To train the fast NLTE algorithm we have used the database of vibrational temperatures computed by Funke and López-Puertas (2015). The database comprises vibrational temperatures for 48 diverse atmospheric profiles extending from the surface to an altitude of 120 km for 13 different values of the solar zenith angle (i.e. 0°, 10°, 20°, 30°, 40°, 50°, 60°, 70°, 80°, 85°, 87°, 90° and 120°). These vibrational temperatures have been computed using the latest version of the GRANADA NLTE population algorithm (Funke *et al.*, 2012). Note that the GRANADA algorithm used in this paper incorporates collisional rates derived from recent MIPAS spectra (Jurado-Navarro *et al.*, 2015). Having obtained the vibrational temperatures, we have computed a database of high-resolution monochromatic NLTE LBL radiances for each profile, for five different values of the sensor zenith angle (i.e. the angles for which the secant has equally spaced values from 1 to 2) and for 12 solar zenith angles (i.e. those corresponding to daytime conditions). This corresponds to a total number of 2880 NLTE spectra to which we have added 240 LTE spectra to form the  $\Delta R_i^{non-LTE}$  differences used in the regression. For testing purposes, we have computed a supplemental database of NLTE LBL spectra for 24 diverse atmospheric situations independent of those used to train the fast NLTE model (see Funke *et al.*, 2012 for details). The independent dataset of vibrational temperatures has been calculated using the same population algorithm utilised for the computation of the dependent dataset. The independent NLTE LBL database comprises 120 spectra (i.e. 24 profiles and 5 sensor zenith angles). Finally, each monochromatic LBL spectrum has been convolved with

the appropriate instrument spectral response function to obtain the IASI polychromatic radiances in each channel  $i$ .

The expected magnitude of NLTE effects is shown in Figure 26 where we have plotted the mean value of the difference between NLTE and LTE LBL computations for the spectra used to train the NLTE model. Results for the old and new GRANADA model are shown in the upper and middle panel respectively. For consistency, we have selected spectra corresponding to the same solar zenith angles (i.e. the six daytime angles specified in the old GRANADA dataset). It can be seen that NLTE effects interest the spectral region between  $2230\text{ cm}^{-1}$  and  $2387\text{ cm}^{-1}$ . This spectral region corresponds to IASI channels with weighting functions peaking above  $\sim 400\text{ hPa}$ . The maximum deviation from LTE occurs at wave numbers between  $2310\text{ cm}^{-1}$  and  $2320\text{ cm}^{-1}$  (i.e. channels peaking between  $9\text{ hPa}$  and  $50\text{ hPa}$ ). The lower panel of Figure 26 shows that, compared to the new GRANADA model, the old GRANADA model consistently underestimates NLTE effects up to a magnitude of  $1\text{ K}$ . Although not shown in Figure 26, it should be noted that the magnitude of NLTE effects increases with decreasing solar zenith angle.

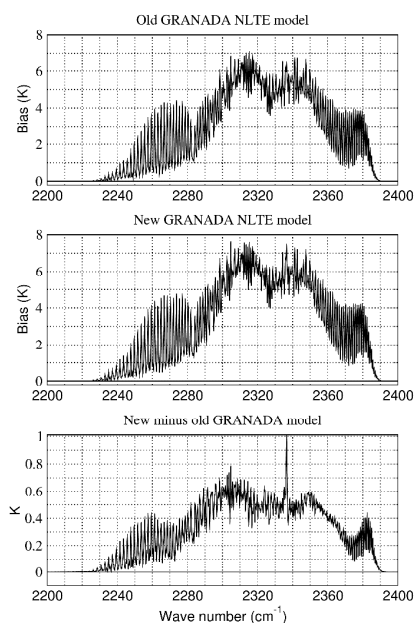


Figure 26. The statistics of the difference between NLTE and LTE LBL computations for the old GRANADA model (upper panel) and the new GRANADA model (middle panel). The lower panel show the difference between results for new and old GRANADA model.

The accuracy of the regression algorithm developed to predict NLTE effects in the IASI short-wave channels can be assessed by comparing the radiances predicted by the model with reference LBL radiances. Firstly, NLTE radiances computed for the atmospheric situations used to train the fast model can be compared with the LBL model equivalents to determine the accuracy of the fast model itself. In the same context, we shall use the set

|   |   |   |   |
|---|---|---|---|
| <p>The EUMETSAT<br/>Network of<br/>Satellite Application<br/>Facilities</p> |  | <h2 style="text-align: center;">RTTOV-12 Science and<br/>Validation Report</h2> | <p>Doc ID : NWPSAF-MO-TV-41<br/>Version : 1.0<br/>Date : 16/02/2017</p> |
|---|---|---|---|

of independent atmospheric situations discussed in section 2 to allow uncertainties from different types of atmospheres to be included. Results for the independent set give a more realistic estimate of the error in that they tell us how good we are in replicating the findings for the training sample in an independent sample from the same population.

The mean value (bias) and the standard deviation of the difference between the NLTE radiances computed by the fast model and the equivalent NLTE radiances computed by the LBL model are shown in the left and right panel of Figure 27 for the dependent and independent set respectively. As expected, the means and standard deviations of the difference statistics in the right panels of Figure 27 are somewhat larger than the corresponding values in the left panels. Results presented in Figure 27 show that in terms of standard deviation, fast-NLTE model errors for the independent set are generally robust. The passage from dependent to independent profiles results in a modest increase of the standard deviation of the error, typically less than 30%. On the other hand, the means do show a substantial increase. Although it is possible that the latter result reflects a difficulty in predicting independent profiles from the population at large, it is more likely that we are seeing the effect of systematic errors introduced by the interpolation of the independent profiles to the vertical grid used for the computation of the training NLTE radiances. To this end, we note that the dependent profiles are specified on a vertical grid that extends up to 120 km whereas the independent profiles are specified on a grid that extends up to 200 km. The latter grid coincides with the former grid for altitudes up to 90 km. To ensure that LBL computations were carried out in a consistent manner, from 90 km to 120 km we interpolated the independent profiles to the slightly coarser grid used for the computation of the training radiances. At these altitudes, vibrational temperatures can be up to 100 K warmer than kinetic temperatures and representativeness errors associated with the vertical interpolation of the temperature profiles are likely to have introduced an inconsistency between kinetic and vibrational temperatures (i.e. in principle vibrational temperatures should have been computed based on the interpolated kinetic temperature profiles). We should note, however, that irrespective of the mechanism responsible for the larger means, fast-NLTE model errors for the independent profiles have still remained acceptable compared to the magnitude of the signal we want to correct (see Figure 26).

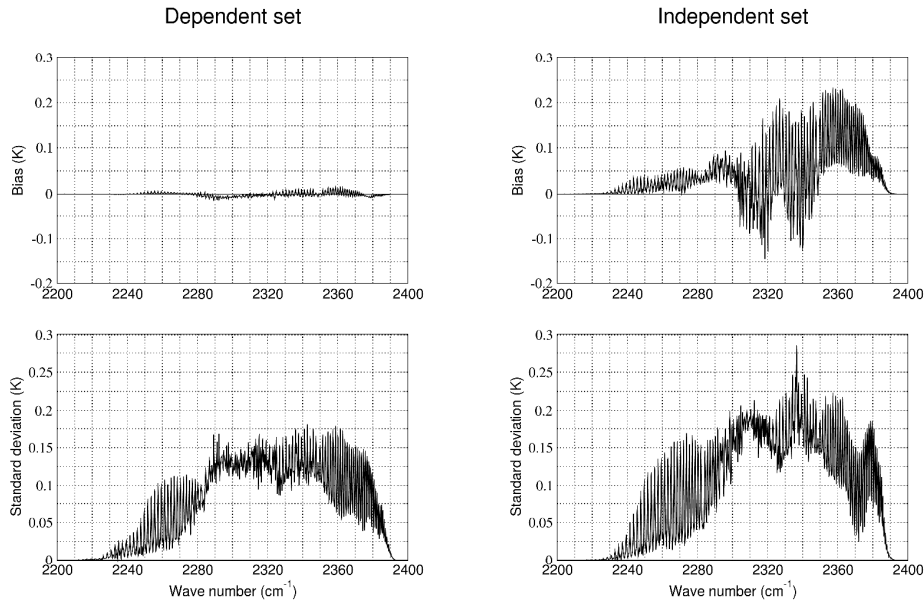


Figure 27. The mean value (upper panels) and the standard deviation (lower panels) of the difference between fast model and LBL model NLTE radiances for the dependent set (left panels) and independent set (right panels).

RTTOV-11 incorporates a simple fast NLTE model (hereafter referred to as the standard NLTE model) described in R11REP2013. For RTTOV-12 a new fast NLTE model (hereafter referred to as the ECMWF NLTE model) has replaced the simple model and has been compared with IASI observations in the spectral region between  $2200 \text{ cm}^{-1}$  and  $2400 \text{ cm}^{-1}$  via RTTOV simulations using both NLTE models. For the simulations we have used global fields of temperature, water vapour and ozone obtained from ECMWF short-range forecasts during the period 10 - 20 November 2014. Only channels detected as clear by the ECMWF cloud detection algorithm have been processed. Since the ECMWF cloud detection algorithm (McNally and Watts, 2003) finds clear channels rather than clear locations, the size of the sample varies with the sensitivity of the channel to clouds. The sample amounts to tens of thousands spectra for the channels peaking at middle and high altitudes to a few thousand spectra for the channels peaking at low altitudes or near the surface.

Daytime results obtained introducing NLTE effects in the RTTOV simulations are shown in the left and right panels of Figure 28 for the standard NLTE model and the ECMWF NLTE model respectively. Note that the dataset utilised to compute that statistic of the differences is the same for both cases. Likewise, simulations have been carried out using the same RTTOV transmittance model. This means that differences between the results are solely due to differences between the two NLTE models. It is evident that the introduction of NLTE effects in the RTTOV simulations greatly reduces the daytime biases and, to an extent, standard deviations. Both NLTE models produce daytime results that

are much closer to the results obtained during night-time. However, residuals from the calculations performed using the standard NLTE model have substantially larger biases. Regarding the regression scheme, the major difference between the standard and the ECMWF NLTE models resides in the number and the form of the predictors. It should be noted that the predictors used in the ECMWF NLTE model allow the computation of global regression coefficients whereas the predictors used in the standard NLTE model only allow the computation of coefficients at discrete points (i.e. for a couple of sensor and solar zenith angles). To compute the NLTE correction for a general value of the sensor and solar zenith angle, the standard NLTE model uses a bilinear interpolation operator.

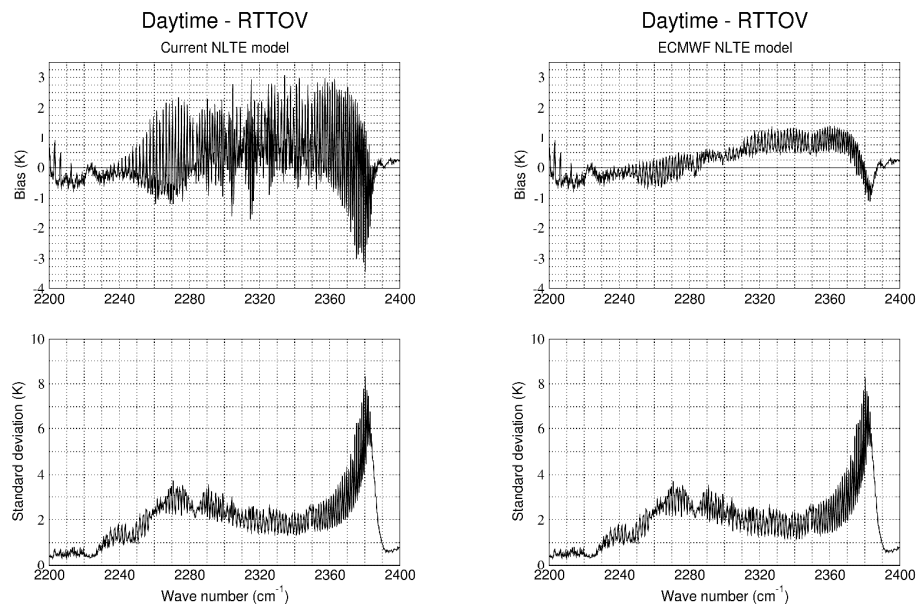


Figure 28. The mean value (bias) (upper panels) and the standard deviation (lower panels) of the difference between observed radiances and radiances computed using RTTOV during daytime. RTTOV simulations include the standard NLTE model (left panels) and the ECMWF NLTE model (right panels).

## 2.11 Coefficients for Zeeman-affected channels

To allow for the Zeeman splitting of oxygen lines, a version of the microwave LbL model AMSUTRAN has been developed (see section 2.1.3) for use when generating RTTOV coefficients for sensors like SSMIS, which have Zeeman-affected channels that sound high in the atmosphere - at lower altitudes the line splitting will be hidden by pressure broadening.

Previously, an original set of coefficients had been generated externally (Han, 2007) for what was to become RTTOV-9, covering just the Zeeman-affected channels of SSMIS, and set on a pressure grid that had virtually no tropospheric representation. To allow the

RTTOV-10 coefficient file to cover all SSMIS channels, a new profile set was constructed from the upper part of the Han set and the lower part of the usual RTTOV-10 training set. This was used to generate RTTOV-10 coefficients for the non-Zeeman channels, which were then augmented by importing the RTTOV-9 coefficients for the four Zeeman channels. These coefficients remained unchanged for RTTOV-11.

The new Zeeman capability of AMSUTRAN has provided the missing step in the end-to-end procedure for generating RTTOV coefficients for instruments like SSMIS, allowing improvements to be made and providing greater flexibility in the choice of profiles, line parameters, line shape, threshold heights, and many other factors.

New LbL calculations have been made for the Zeeman channels of SSMIS, introducing greater precision to the line frequencies so as to properly symmetrise the channel passbands, and using a much smoother pressure grid from the surface to 100 km generated through an analytic formula originally introduced by the AIRS Science Team. For RTTOV-12, the old profiles were interpolated onto the new pressure grid, and new coefficients for SSMIS incorporating the Zeeman effect for channels 19-22 were generated.

| Channel | Bias K  | RMSE K | S.Dev K | B CosBK |
|---------|---------|--------|---------|---------|
| 19      | 0.2704  | 0.3043 | 0.1397  | 0.6 0.0 |
| 19      | 0.4438  | 0.4749 | 0.1690  | 0.2 0.0 |
| 19      | 0.1963  | 0.2326 | 0.1246  | 0.6 1.0 |
| 19      | 0.3465  | 0.3757 | 0.1451  | 0.2 1.0 |
| 20      | 0.1442  | 0.1496 | 0.0398  | 0.6 0.0 |
| 20      | 0.0279  | 0.0386 | 0.0266  | 0.2 0.0 |
| 20      | 0.0765  | 0.0814 | 0.0277  | 0.6 1.0 |
| 20      | -0.1031 | 0.1211 | 0.0635  | 0.2 1.0 |
| 21      | -0.1206 | 0.1375 | 0.0660  | 0.6 0.0 |
| 21      | -0.1338 | 0.1564 | 0.0809  | 0.2 0.0 |
| 21      | -0.1163 | 0.1327 | 0.0639  | 0.6 1.0 |
| 21      | -0.1363 | 0.1590 | 0.0819  | 0.2 1.0 |
| 22      | -0.1335 | 0.1450 | 0.0567  | 0.6 0.0 |
| 22      | -0.1381 | 0.1500 | 0.0587  | 0.2 0.0 |
| 22      | -0.1658 | 0.1784 | 0.0660  | 0.6 1.0 |
| 22      | -0.1412 | 0.1529 | 0.0587  | 0.2 1.0 |

Table 5. Brightness temperature differences (RTTOV-12 - RTTOV-10) for a scan angle of 51° for the four Zeeman-affected mesospheric channels of SSMIS. The last column gives the magnitude of the geomagnetic field (gauss) and the cosine of the angle between the field direction and the viewing path.

In comparison with the imported coefficients, the use of a smoother pressure grid should ensure that the behaviour of derivatives, which depends on the grid spacing, is good in all circumstances. Nevertheless, agreement for the forward calculation should be close, if not exact. Comparison statistics, taken over the training profiles, appear in Table 5 and show

|   |   |   |   |
|---|---|---|---|
| <p>The EUMETSAT<br/>Network of<br/>Satellite Application<br/>Facilities</p> |  | <p>RTTOV-12 Science and<br/>Validation Report</p> | <p>Doc ID : NWPSAF-MO-TV-41<br/>Version : 1.0<br/>Date : 16/02/2017</p> |
|---|---|---|---|

that, although RMS differences for channel 19, mainly bias, amounts to a few tenths of a kelvin, they are, for the other three channels, somewhat smaller.

## 2.12 Coefficients for the PMR pressure modulator radiometer

For RTTOV-12, there has been some work to assist in the reanalysis of historical satellite data funded by the ERA-CLIM2 project. Following on from the provision of updated SSU coefficients for RTTOV-11, coefficients have now also been generated for the Pressure Modulator Radiometer (PMR) on Nimbus-6, which was active from 1975 to 1983. Two aspects of this work are described below, the channel selection and the profile set.

PMR is a pressure modulator radiometer, in that, on its way to the detector, atmospheric radiation passes through either of two small cells holding CO<sub>2</sub> at low pressure (Curtis *et al.*, 1973). The mean pressure of each cell can be varied using a remotely activated sieve device, but they spend virtually all the time between calibration and testing each with the mean pressure at its lowest, most stable, value. This is about 0.62 hPa for both cells. Because of the sieve, no pressure drift correction should be needed - of the sort used for SSU in RTTOV-11.

As for SSU, the cell pressure is made to oscillate by a piston, affecting some parts of all the CO<sub>2</sub> lines in the cell spectrum more than others. This allows the detector electronics to select radiation from that same part of all the atmospheric CO<sub>2</sub> lines, and, therefore, from the layer of the atmospheric column that most contributes to absorption in that part of each line. Simplistically to show the principle, the detected part will be in the near wing for stronger lines, because the gas cell transmittance, and therefore its oscillation over the pressure cycle, will be very small near line centre. The only radiation to be detected must then come from lower altitudes, where the pressure is sufficiently high for wing absorption to be significant. For the weaker lines, however, the detected part will be close to the line centre, since this will still be relatively transparent and oscillations will be large. The only radiation to be detected must then come from higher altitudes, since, that close to the line centre, any that arises further back along the path will be too heavily absorbed. In this way, a characteristic weighting function is defined, aggregating the effect of all lines in the spectrum, strong or weak, and dominated, therefore, by Doppler broadening aloft, where the detector tends to see line centres, and Lorentz broadening lower down, where the detector tends to see line wings.

However, as the along-track scanning cycle sweeps the PMR field of view back and forth, and measurements are taken, the weighting function will be affected differently at each scan angle, because there will be a different a shift in the atmospheric spectral lines through the Doppler effect. Over the PMR scan cycle, through nadir from -15° to +15°, 88 measurements are taken, associated with 88 different weighting functions, though those for adjacent scan angles will be highly correlated. Given that, a set of nine were selected, as shown in Figure 29, presenting PMR to RTTOV as a radiometer with nine channels.

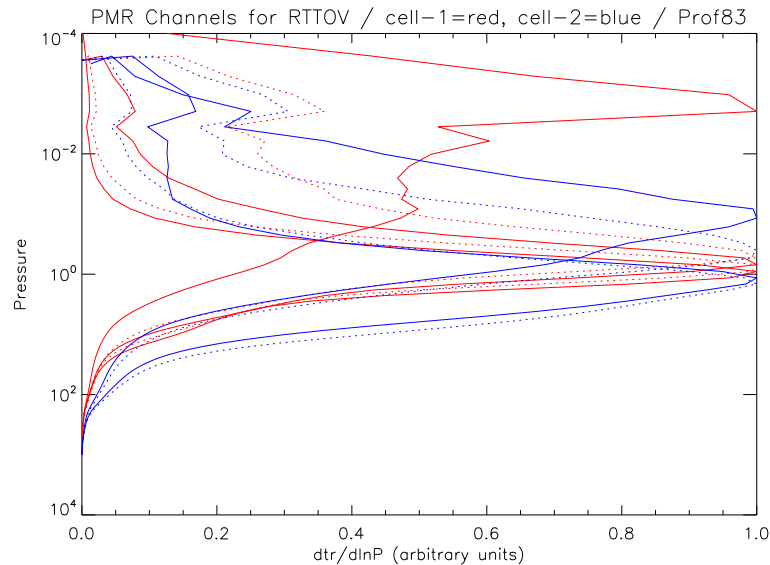


Figure 29. Weighting chosen to define RTTOV channels for PMR, each cell alternating solid and dotted.

For both PMR gas cells the nadir view offers the highest peaking weighting function, at 90 km (red solid) and 65 km (blue solid) respectively, and they provide channels 1 and 2 for sounding the upper and lower mesosphere. The weighting function for cell 1 has the suggestion of a lower lobe, and this becomes more pronounced a few degrees away from nadir. Such very broad, bimodal weighting functions were rejected. The other seven channels all sound in the upper stratosphere, between 55 km and 45 km, the lowest (blue dotted) offering a close comparison with channel 3 of SSU.

The historically adjusted profile set described in section 2.1.1 was not available for this work, but another procedure was used to provide profiles that cover the lower CO<sub>2</sub> abundances associated with the PMR operational period in the 1970s.

In a procedure essentially the same as that used for SSU in RTTOV-11 (R11REP2013), the standard set of 83 profiles on 101 levels were systematically stretched downwards at each level in respect of CO<sub>2</sub> abundance, the adjustment being larger for values further away from the maximum for that level. These profiles extend to 0.005 hPa, but for PMR, which sounds into the high mesosphere, values varying across the profile set were added to the existing top of atmosphere based on temperature values at 0.001 hPa and 0.0001 hPa from the six AFGL model atmospheres, and on CO<sub>2</sub> data at those levels from the Canadian ACE-FTS on SCISAT-I, which was launched in 2003 – with reference to Beagley *et. al.* (2010) and Garcia *et. al.* (2014). The augmented profiles were then interpolated onto a new 84 level pressure grid extending smoothly from 1050 hPa to 0.0001 hPa, this having been generated by an analytic formula originally introduced by the AIRS Science Team.

|   |   |   |   |
|---|---|---|---|
| <p>The EUMETSAT<br/>Network of<br/>Satellite Application<br/>Facilities</p> |  | <p>RTTOV-12 Science and<br/>Validation Report</p> | <p>Doc ID : NWPSAF-MO-TV-41<br/>Version : 1.0<br/>Date : 16/02/2017</p> |
|---|---|---|---|

When using the PMR coefficients, RTTOV should be run for the nadir view, whatever the actual viewing geometry. The angle-dependent Doppler shift must be regarded as fixed for a given PMR channel, and will be included with the LbL calculation – as will the airmass correction, which will be small for PMR scan angles. The correction for earth curvature is small for the same reason, and may be omitted. A more detailed report (Rayer, 2017) on the PMR coefficient generation is available from the NWP SAF on request.

### 2.13 Additional changes to internal calculations which affect RTTOV radiance calculations

Some additional changes have been made within RTTOV which have a small impact on RTTOV radiances. These have been implemented to keep RTTOV up to date with new science and to eliminate minor historical inconsistencies in the code. They are listed below.

- Values of some physical constants used by RTTOV have been updated with the latest values from the NIST website (<http://physics.nist.gov/cuu/Constants/>).
- In previous versions of RTTOV the 2m water vapour variable (*profiles(:)%s2m%q*) was never used with v9 predictor coefficient files. The 2m q variable is now used for any coefficient file if the *use\_q2m* option is set true.
- In previous versions of RTTOV the default behaviour when the input profile top is below the top of the coefficient pressure levels is to extrapolate the input profile at constant value to the top coefficient pressure level. This could often result in warnings where the extrapolated values exceeded the RTTOV regression limits. RTTOV v12 automatically clips all extrapolated profile values at the top of the profile to the regression limits where the limits are exceeded. This avoids unphysical and out-of-limit values being introduced into the interpolated profile by RTTOV and consequently also avoids any associated warning messages from RTTOV. For well-specified input profiles where the range of input pressure levels fully spans the vertical extent of the weighting functions of the channels being simulated this change has no significant impact. Larger differences are observed if this condition is not met, but in such cases the accuracy of the simulations will be compromised anyway.
- The calculation of the geopotential height has been modified to avoid numerical problems if the input profile has very thick layers near the top of the atmosphere. The geopotential height calculation involves evaluating the integral of the reciprocal of density with respect to pressure (from the hydrostatic equation) under the assumption that density varies linearly with pressure. Previously this integral was approximated using the trapezium rule. In RTTOV-12 the integral is evaluated analytically.

|   |   |   |   |
|---|---|---|---|
| <p>The EUMETSAT<br/>Network of<br/>Satellite Application<br/>Facilities</p> |  | <h2 style="text-align: center;">RTTOV-12 Science and<br/>Validation Report</h2> | <p>Doc ID : NWPSAF-MO-TV-41<br/>Version : 1.0<br/>Date : 16/02/2017</p> |
|---|---|---|---|

- The calculation of the local path angles along the surface-satellite path has been modified slightly to improve internal consistency: this is now consistent with the calculation of local angles along the sun-surface path which ensures that the local path angles on the two paths are identical for the same satellite and solar zenith angles (previously they differed slightly) and it ensures that the local path angle calculated in the layer at the surface is identical to the input satellite zenith angle (previously they differed slightly).

The impact of these changes is generally observed to be of the order of several hundredths of a Kelvin or less though the last of the changes listed above (related to local path angles) can in some cases result in differences of the order of tenths of a Kelvin at very high zenith angles (e.g. above 75°). For identically-configured simulations these changes are the only source of differences between RTTOV v11.3 and v12 (see Section 3 which compares the two models).

#### 2.14 Other changes to RTTOV behaviour which affects outputs

The following changes have been made in RTTOV-12 which cause differences in behaviour/outputs compared to v11.3:

- The *do\_lambertian* option which activates an approximation to Lambertian surface reflectance (as opposed to the default assumption of specular reflection) was originally implemented for MW sensors only and was not activated for channels where FASTEM was being used. In RTTOV v11.3 the option was also applied to IR channels over all surface types. In RTTOV-12 the *do\_lambertian* option, when activated, is applied to all MW and IR channels where an internal sea surface emissivity model is **not** being used as the option is not compatible with the assumptions behind the emissivity models.
- When calling the TL model for visible and IR sensors, if the input *emissivity\_tl(:)%emis\_in* or *reflectance\_tl(:)%refl\_in* is non-zero then this input perturbation will be used instead of any calculated emissivity/reflectance perturbation that would result from RTTOV's internal emissivity/reflectance calculations. This makes the behaviour for visible/IR sensors consistent with the FASTEM TL for MW sensors which has behaved this way in previous versions of RTTOV.

### 3. Testing and Validation of RTTOV-12

#### 3.1 Validation of top of atmosphere radiances

##### 3.1.1 Comparison of simulations

The primary outputs from RTTOV are the top of atmosphere radiance for each channel and so this is the main parameter for which the RTTOV-12 simulations are checked and compared with the corresponding RTTOV-11 values. The main reason for differences between RTTOV-11 and RTTOV-12 computed radiances are due to the changes listed in the previous section. Comparisons between RTTOV v11.3 and RTTOV v12.1 were made according to the parameters listed in Table 6 for calculations on a 83 diverse profile set. The mean differences were then plotted in the following figures.

| Parameters                                     | RTTOV-10  | RTTOV-11   | RTTOV-12   |
|--|---|--|--|
| Number of layers for optical depth calculation | 51 (0.005-1050hPa)<br>except for IASI:101 (0.005-1050hPa) | 54 (0.005-1050hPa)<br>except for IASI: 101 (0.005-1050hPa) | 54 (0.005-1050hPa)<br>except for IASI: 101 (0.005-1050hPa) |
| Input Profile set                              | 83 Profiles on 101L                                       | 83 Profiles on 101L  | 83 Profiles on 101L  |
| <b>IR Transmittances</b>                       |   |  |  |
| Spectroscopic data                             | LBLRTMv11.1/<br>HITRAN2006/GEISA                          | LBLRTMv12.2/<br>AER 3.2,<br>MTCKD2.5.2                     | LBLRTMv12.2/<br>AER 3.2,<br>MTCKD2.5.2                     |
| Surface emissivity                             | 0.98  | 0.98   | 0.98   |
| Optical depth predictors                       | Version 7 HIRS<br>Version 9 IASI                          | Version 7 HIRS<br>Version 9 IASI                           | Version 7 HIRS<br>Version 9 AH1<br>Version 7/8/9 IASI      |
| <b>MW Transmittances</b>                       |   |  |  |
| Spectroscopic data                             | Liebe 89/92   | Liebe 89/92  | Liebe 89<br>update/Tretyakov 05                            |
| Surface emissivity                             | 0.6   | 0.6  | 0.6  |
| Optical depth predictors                       | Version 7   | Version 7  | Version 7  |

Table 6. The parameters assumed for the RTTOV-10, RTTOV-11 and RTTOV-12 comparisons

The results are shown for NOAA-15 HIRS channels for a zenith angle of 50 deg in Figure 30 using version 7 predictors throughout and both using the same coefficient files (top panel) so the differences are just due to the code changes between both versions of

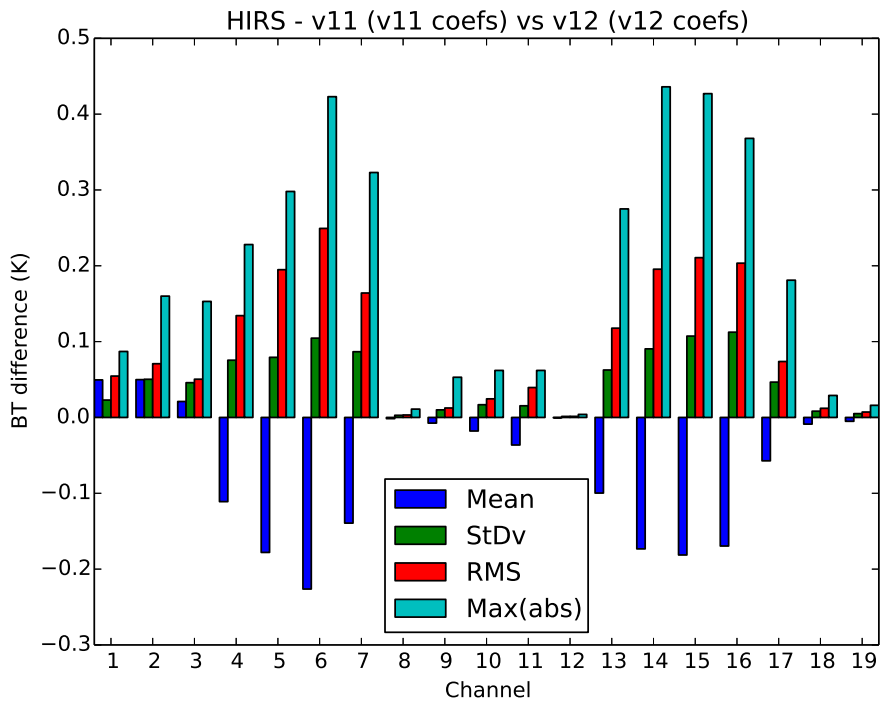
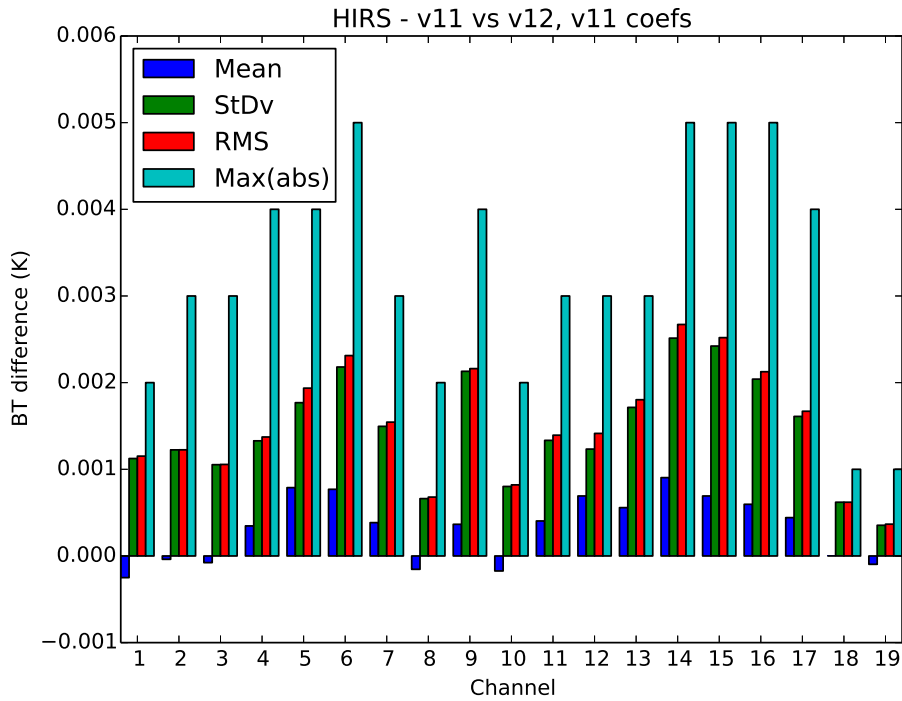


Figure 30. Differences in NOAA-15 HIRS channels between RTTOV-11 and RTTOV-12 due to code changes (upper panel) and coefficient changes (bottom panel) for a zenith angle of  $50^\circ$ .

|   |   |   |   |
|---|---|---|---|
| <p>The EUMETSAT<br/>Network of<br/>Satellite Application<br/>Facilities</p> |  | <h2 style="text-align: center;">RTTOV-12 Science and<br/>Validation Report</h2> | <p>Doc ID : NWPSAF-MO-TV-41<br/>Version : 1.0<br/>Date : 16/02/2017</p> |
|---|---|---|---|

RTTOV. For nadir views the results are identical between both model versions. The mean differences for 50 deg are all below 0.003K with the maximum difference around 0.005K. They are well below the instrument noise and demonstrate the model changes described in section 2 are not significantly changing the infrared radiances for clear sky radiances. When the new RTTOV-12 coefficients are used in RTTOV-12 the bottom panel of Figure 30 shows the impact of the latest coefficients plus the almost insignificant impact of the code changes in v12. In this case there are much bigger differences for the temperature sounding channels (up to 0.45K) which are due to several factors. These include updated spectroscopy, updated concentrations of CO<sub>2</sub> and CH<sub>4</sub> from 1995 values to current values in the mixed gas transmissions and different temperature and water vapour profiles in the diverse profile set. The change in the greenhouse gas concentrations is the main contributor to the differences.

A similar plot for the microwave instruments is shown in Figures 31 for NOAA-15 AMSU-A (upper panel) and AMSU-B (lower panel). For these plots the coefficients used are the same as they were not changed since the last version (May 2016) of the RTTOV-11 coefficients so only differences due to model code changes are seen. They are all close to or less than 0.01K well below the instrument noise. It is important to note that earlier RTTOV-11 MW coefficients (i.e. pre May 2016) may be subject to the bug reported in section 2.1.3 which can lead to large differences (>0.5 K) for some instruments and channels listed in that section.

For IASI there are 3 versions of optical depth predictors that can be used (versions 7, 8 & 9) depending on what variable gases you need. Version 7 is only for mixed gases, water vapour and ozone, version 8 adds carbon dioxide and version 9 adds several more traces gases (CH<sub>4</sub>, N<sub>2</sub>O, CO, SO<sub>2</sub>). Figure 32 compares the differences for all 3 predictor sets between RTTOV-11 and RTTOV-12 coefficients. As for HIRS the differences are mainly due to different diverse profiles and trace gas concentrations in the profiles used to train the coefficients. As for HIRS the mean differences are up to -0.2K for version 7 predictors which only have mixed gas transmittances and don't allow for changes in the trace gas concentrations. The differences for version 8 and 9 coefficients are smaller where the former allows for variable CO<sub>2</sub> and the latter also allows for all the trace gases except SO<sub>2</sub> to vary.

Finally a comparison was made for a high inclination angle (75 deg) for the Himawari-8 imager (AHI) as shown in Figure 33 where different versions of the RTTOV code are used (v11 vs v12) but the same coefficients are employed. The differences for these large incidence angles are due to the change in the computation of the local path in module `rttov_locpat` resulting in a maximum mean biases of  $-1.0 \times 10^{-3}$  in reflectance and up to 0.05 K in brightness temperature for the AHI channels.

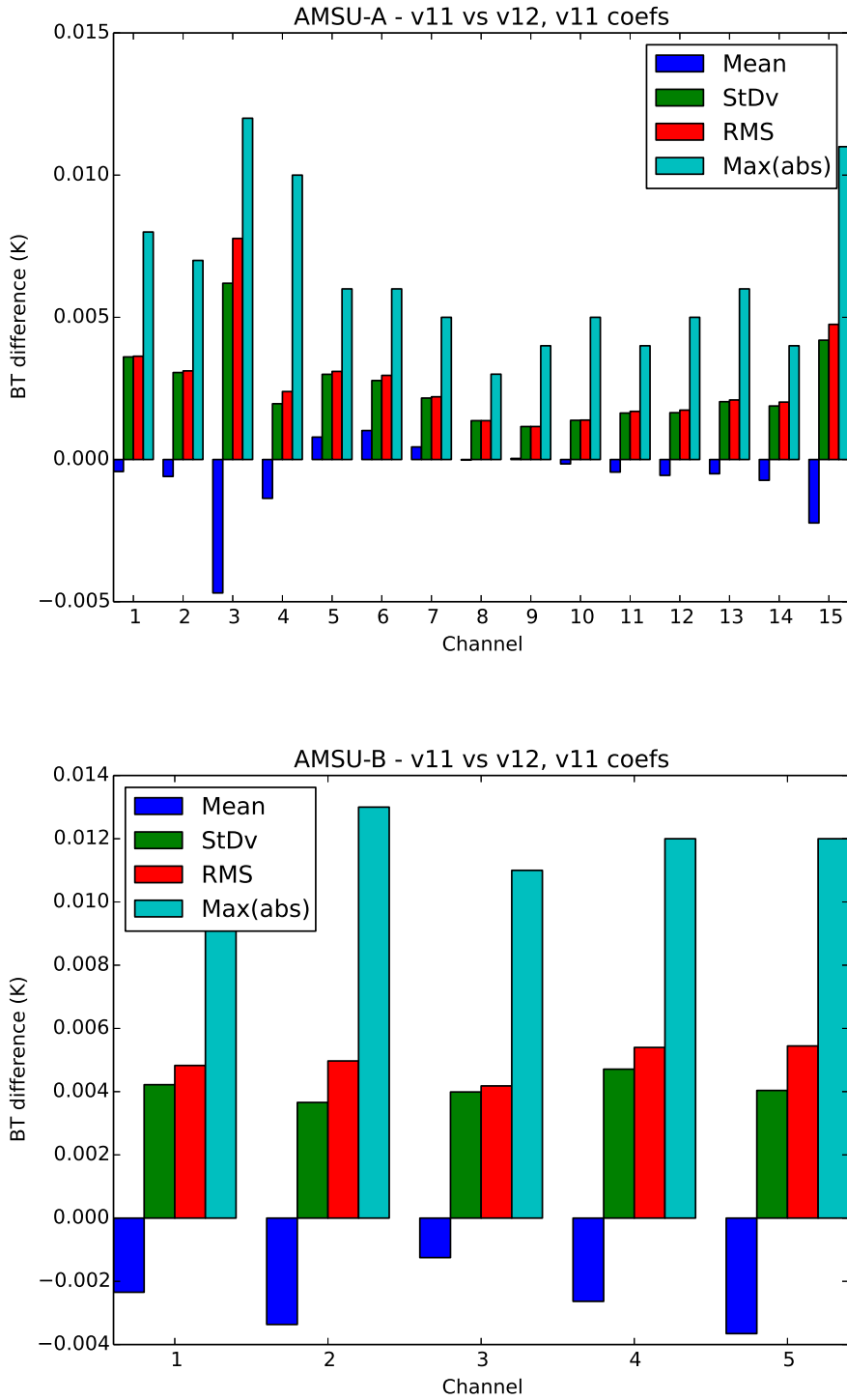


Figure 31. Comparison of RTTOV-11 and RTTOV-12 for a diverse profile dataset at 50 deg zenith angle for NOAA-15 AMSU-A top panel) and AMSU-B (bottom panel) using the same coefficients.

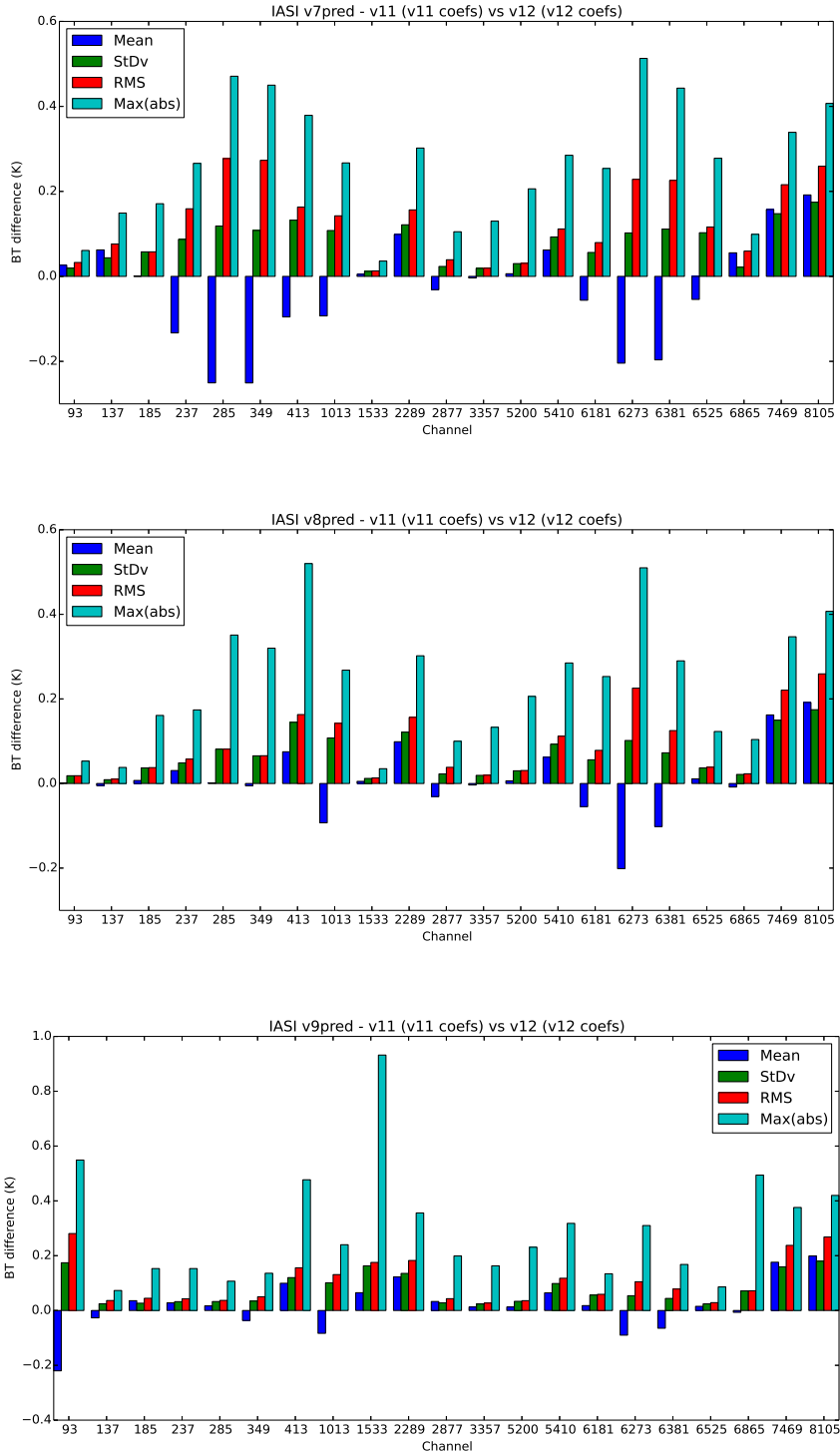


Figure 32. Comparison of IASI brightness temperature differences for version 7, 8 and 9 optical depth predictors between RTTOV-11 and RTTOV-12.

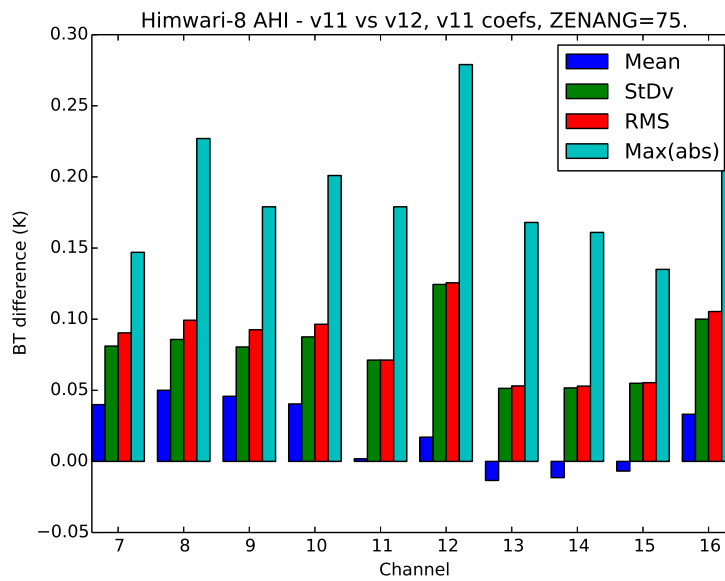
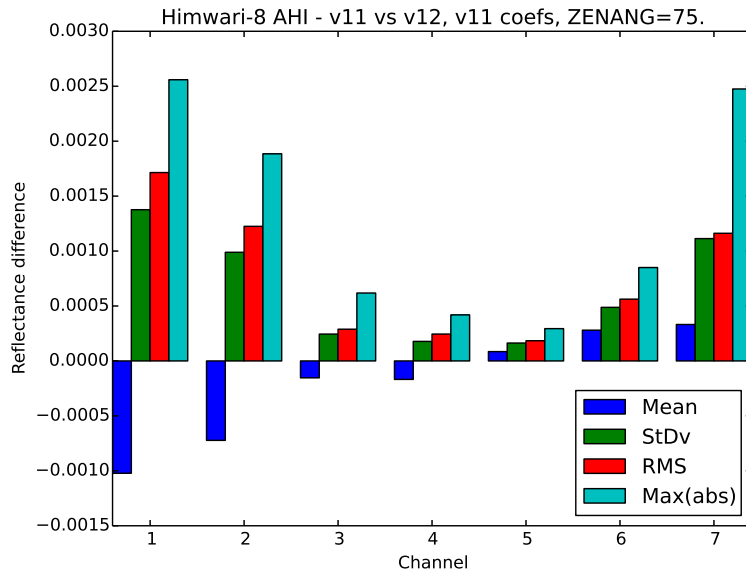


Figure 33. Comparison of Himawari-8 AHI reflectances (top panel) and brightness temperatures (bottom panel) for the RTTOV-11 and RTTOV-12 code using the same coefficients. Viewing angle was 75 deg, surface bidirectional reflectance was 0.1 and emissivity 0.98.

|   |   |   |   |
|---|---|---|---|
| <p>The EUMETSAT<br/>Network of<br/>Satellite Application<br/>Facilities</p> |  | <p>RTTOV-12 Science and<br/>Validation Report</p> | <p>Doc ID : NWPSAF-MO-TV-41<br/>Version : 1.0<br/>Date : 16/02/2017</p> |
|---|---|---|---|

### 3.1.2 Comparison with observations

A comparison of the RTTOV-11 and RTTOV-12 radiances with coincident observations has been made using the ECMWF IFS model fields.

#### 3.1.2.1 Experimental set-up

To characterise the impact in the IFS of RTTOV-12, released with a new set of regression coefficient files for MW and IR instruments, we conducted a set of two monitoring experiments in which the same FG is used to calculate model equivalents for different MW and IR observation types. This allows us to examine the FG departure statistics without the interaction between model fields and bias corrections otherwise present in the assimilation experiments which were:

- RTTOV-11: control ECMWF data assimilation and forecasting model with all operational observations and using RTTOV-11 and the IFS operational IR and MW coefficient files.
- RTTOV-12: Same system configuration, except that RTTOV-11 has been replaced by RTTOV-12 and the MW and IR coefficient files have been replaced by the new RTTOV-12 files. Version 7 of the optical depth predictors is used for all IR and MW observations, except for IASI, CrIS and AIRS where version 8 predictors are used.

The experiments have been run for one month period 2 May - 2 June 2016 at reduced TCo399 horizontal resolution and 137 vertical levels with the model top level pressure at 0.01 hPa.

#### 3.1.2.2 Bias characteristics and departure statistics

One of the main changes in the MW coefficient file upgrade is the new specification for the half width of the 183 GHz water vapor line and its temperature dependency. This leads to a reduction in the global mean bias corrections for sensors such as ATMS (channels 18-22), MHS (channels 3-5), SSMIS (channels 9-10) as illustrated in Figure 34. The results show better agreement with the observations and lower forward model error as result of using improved MW spectroscopy. In terms of improvement in the 12-h forecast as indicated by the reduction in the standard deviation of first guess departures, this leads to improved FG fit for MHS (channels 4-5, up to 1.8%) and ATMS (channels 18-19, up to 1% and a slightly degraded FG fit for ATMS channel 22 (Figure 35).

|   |   |   |   |
|---|---|---|---|
| <p>The EUMETSAT<br/>Network of<br/>Satellite Application<br/>Facilities</p> |  | <h2 style="text-align: center;">RTTOV-12 Science and<br/>Validation Report</h2> | <p>Doc ID : NWPSAF-MO-TV-41<br/>Version : 1.0<br/>Date : 16/02/2017</p> |
|---|---|---|---|

The correction of the ozone error in the MW coefficient files will impact on the temperature sounding channels (e.g., ATMS channels 6-15 in Figures 34 and 35). The standard deviations of FG-departures are significantly reduced for ATMS channels 6-9, but also significantly increased for the stratospheric channels 11-14.

Maps of the FG-departures before the bias correction for ATMS temperature sounding channel 6-13 are shown in Figures 36 and 37 for both experiments. Here, the mean of the first-guess departures has been computed before bias correction, but then the global mean bias has been removed to focus attention on the spatial patterns. Although the new ATMS coefficient file used with RTTOV-12 do reduce the mean global bias for several channels, the air-mass dependent biases look fairly similar between the two experiments. The standard deviation of the first-guess fits to AMSU-A observations results are consistent with the ATMS results and confirm temperature improvements through the troposphere up to around 100 hPa and temperature degradation for the higher AMSU-A channels (Figure 38).

For a number of IR sensors (e.g. IASI, AIRS), the regression coefficients used with RTTOV-11 have been computed using the kCARTA while the new released IR coefficient files with RTTOV-12 are based on LBLRTM. Other changes in the IR coefficient files include updated concentrations of CO<sub>2</sub> to current values in the mixed gas transmissions and a different training set of diverse atmospheric profiles. Figure 39 shows FG-departures statistics (mean and standard deviations) before bias correction for IASI on MetOp-A channels calculated from the two monitoring experiments with different versions of spectroscopy and line-by-line models. Statistics are shown for one day on 10 May 2016 for the same set of coincident clear IASI observations. The standard deviations of FG-departures increase in the RTTOV-12 experiment on both sides of the CO<sub>2</sub> Q-branch centred at approximately 720 wavenumbers and in the O<sub>3</sub> band centered at approximately 1020 wavenumbers (e.g. IASI channels numbers 222-410 and 1479-1671). Further investigations are required to understand the results with the latest LBLRTM coefficients.

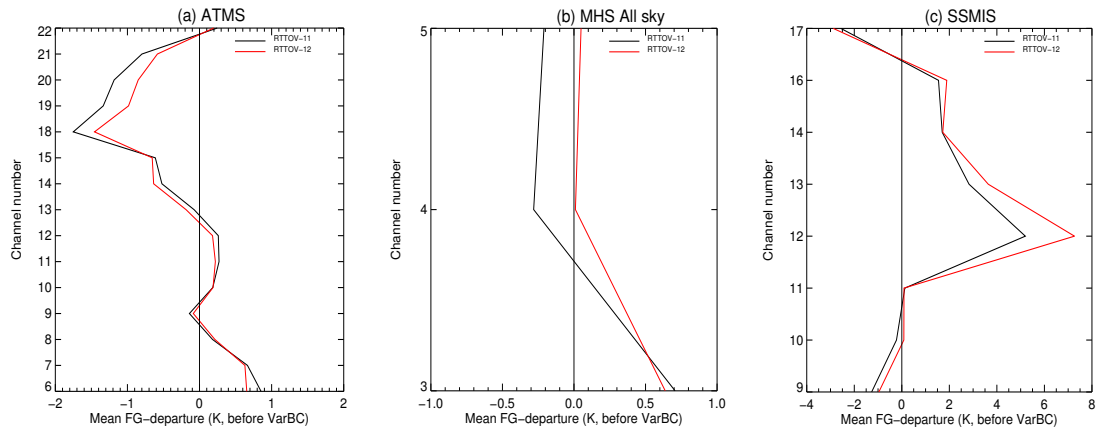


Figure 34. Mean global FG departures before VarBC for period 2 May-2 June 2016. (a) ATMS; (b) MHS all sky radiances from NOAA-18/19/MetOp-A/B; (c) SSMIS from DMSP F17/F18.

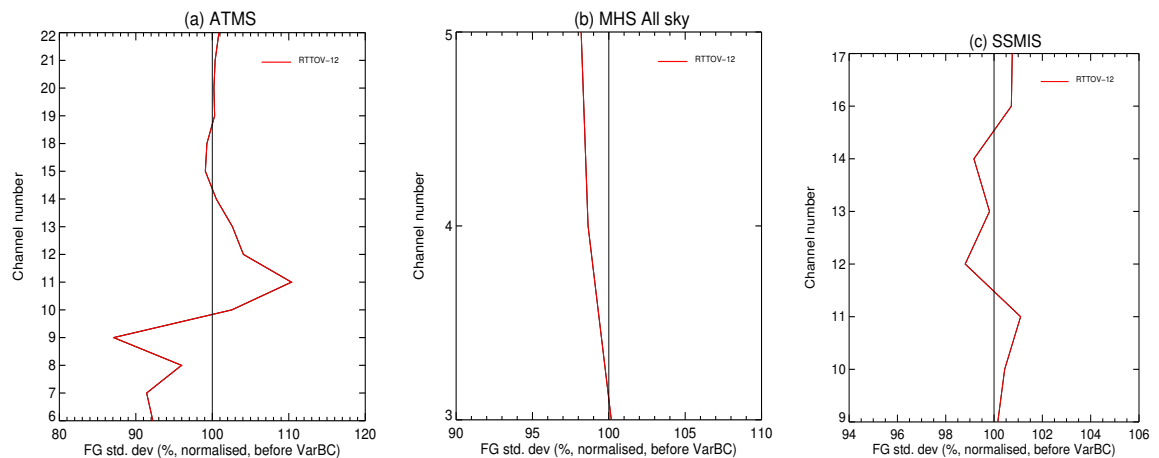


Figure 35. Normalised standard deviations of FG-departures for the period 2 May - 2 June 2016: a) ATMS; b) MHS All sky radiances from NOAA-18/NOAA-19/MetOp-A/MetOp-B; c) SSMIS from DMSP F17/F18. Statistics are calculated over the globe and the normalisation is with respect to the standard deviations of the RTTOV-11 experiment. Values below 100% indicate smaller standard deviations when improved MW spectroscopy has been incorporated into the RTTOV-12 radiative transfer modelling.

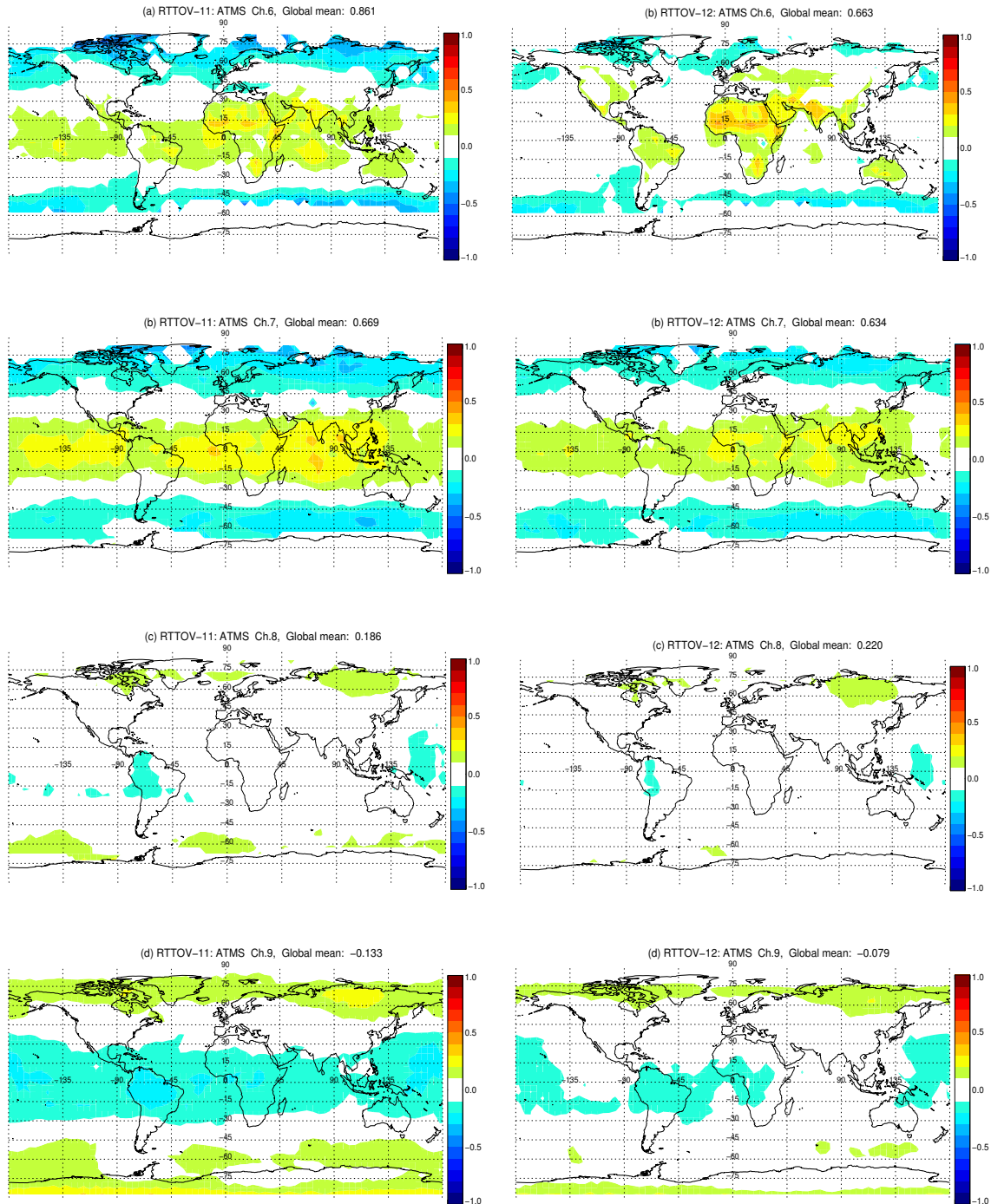


Figure 36. Mean of first-guess departures before bias correction, binned to a 5° latitude-longitude grid, but with the mean bias correction removed for ATMS channel 22 from the (a) RTTOV-11 and (b) RTTOV-12 experiments. The sample is based on the period 2 May to 2 June 2016.

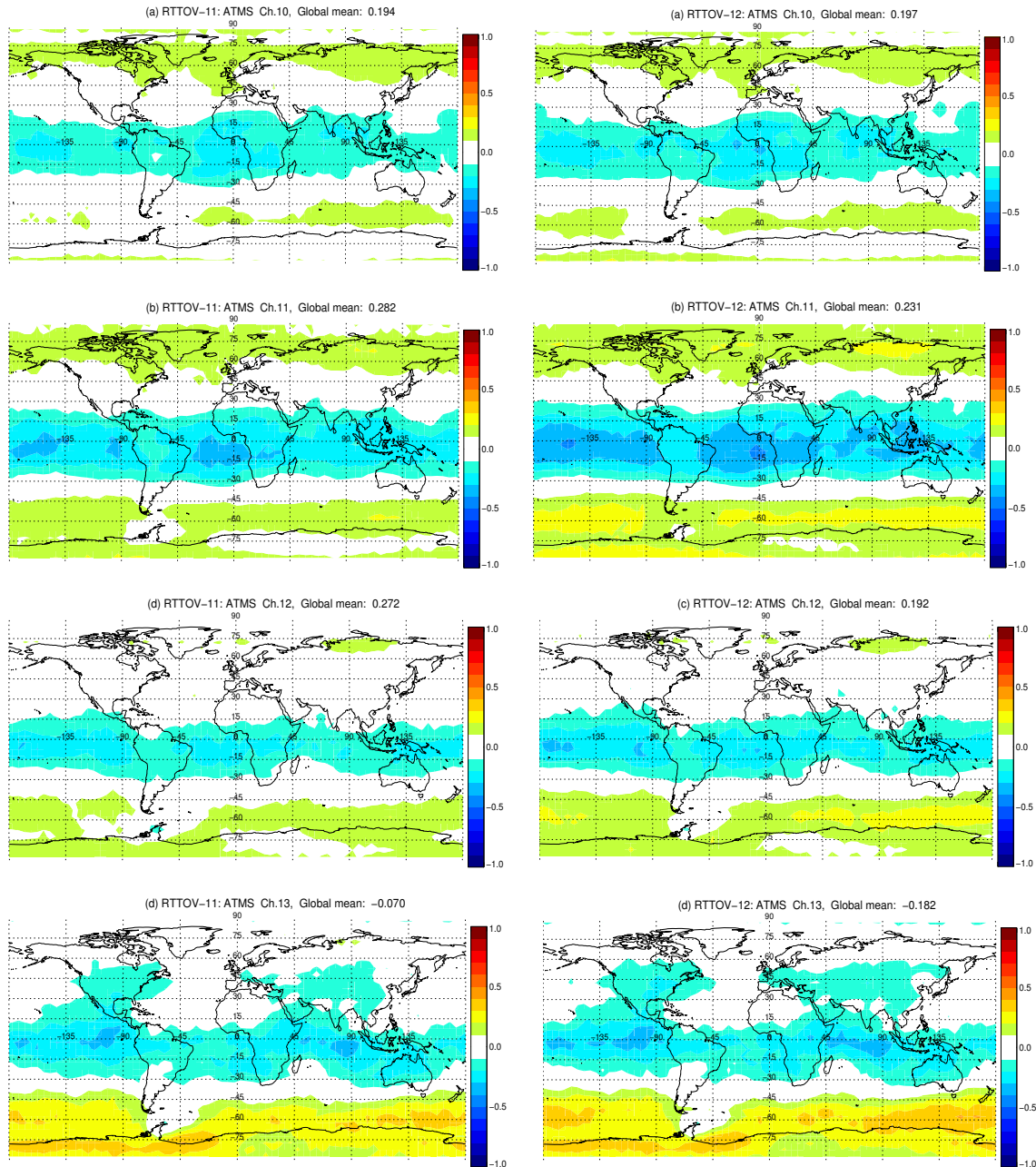


Figure 37. Mean of first-guess departures before bias correction, binned to a 5° latitude-longitude grid, but with the mean bias correction removed for ATMS channel 22 from the (a) RTTOV-11 and (b) RTTOV-12 experiments. The sample is based on the period 2 May to 2 June 2016.

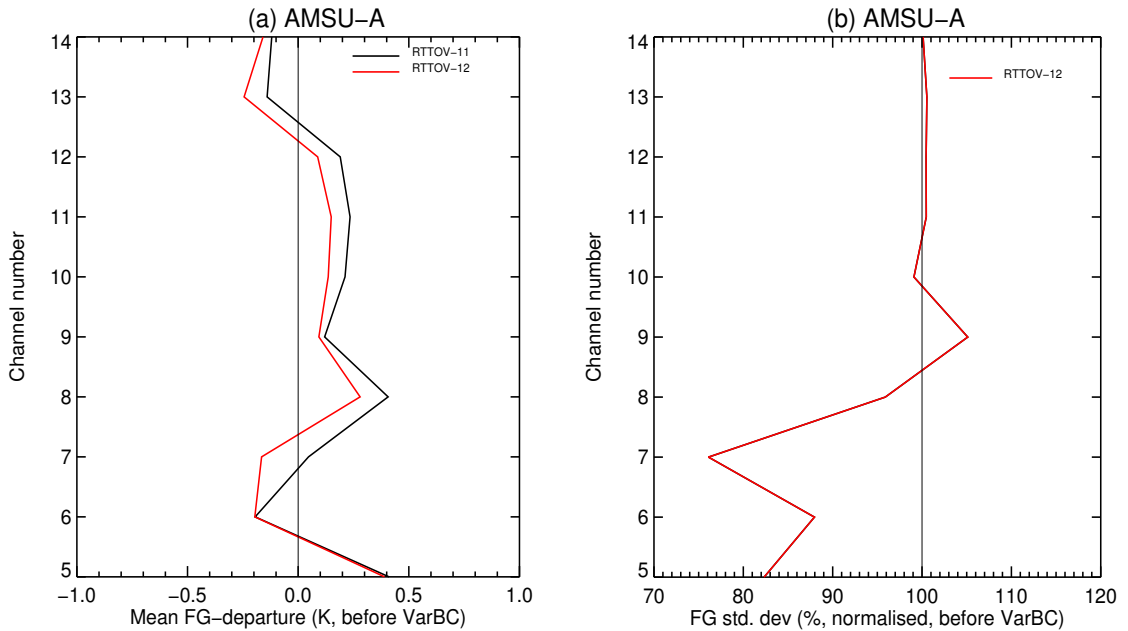


Figure 38. Mean (left) and normalised standard deviations (right) of global FG-dep before bias correction for all 6 AMSU-A's for the period 2 May - 2 June 2016.

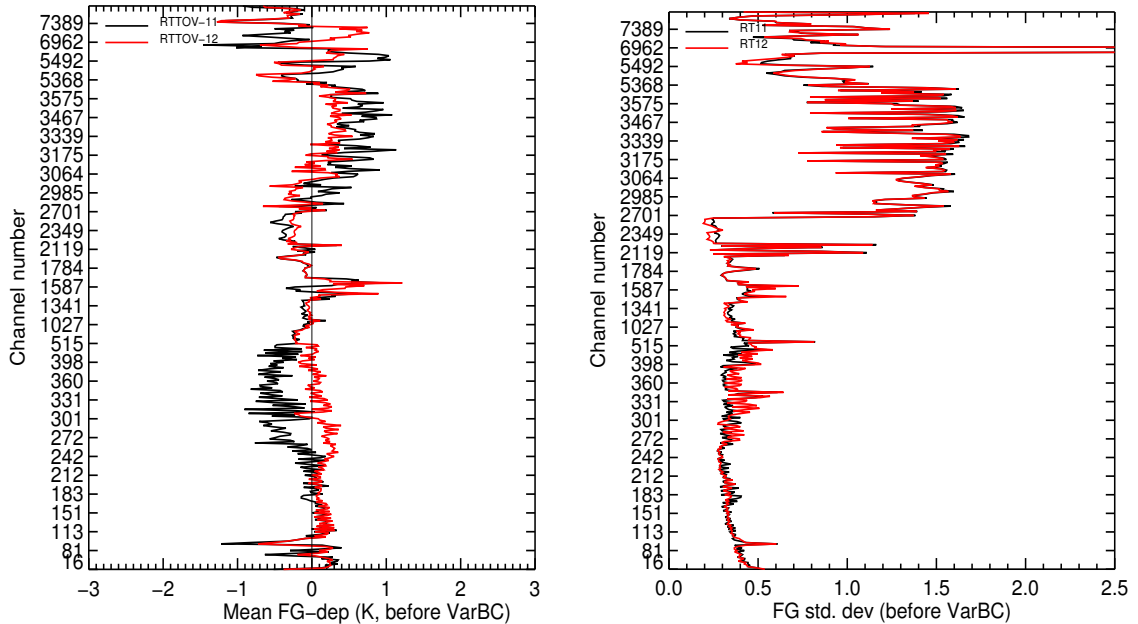


Figure 39. Mean (left) and standard deviations (right) of global FG-departures before bias correction for 420 IASI MetOp-A channels for 10 May 2016 for the two experiments with RTTOV-11 (black line) and RTTOV-12 (red line).

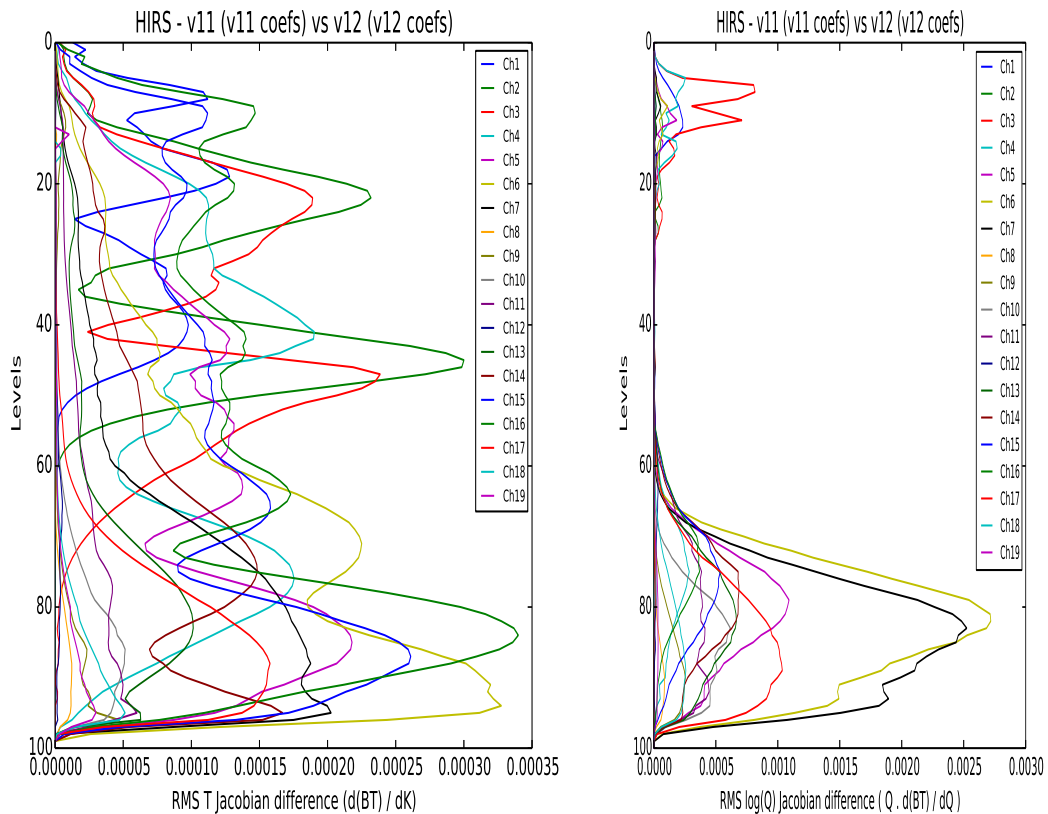


Figure 40. Comparison of differences in HIRS temperature (left) and water vapour (right) Jacobians for v11 and v12 coefficients using v7 predictors.

### 3.2 Comparison of Jacobians

The tangent-linear, adjoint and Jacobians computed in RTTOV are vital for data assimilation applications and so a comparison is made between the Jacobians computed by the old and new models. In order to emphasise all the differences a zenith angle of 50 deg was chosen for the comparisons to maximise any differences\*9 due to local path computations.

The differences for the temperature and water vapour Jacobians for HIRS channels are shown in Figure 40 due to using v11 and v12 coefficient files. As for the forward model the new profile datasets used to train the coefficients are the main cause of the differences. The differences due to the new version of the model are at least an order of magnitude smaller than this (not shown). For the water vapour Jacobians again the new training profiles are the main cause for the differences shown in Figure 40.

The temperature channel Jacobians for ASMU-A are shown in Figure 41. Again the differences are very small and in this case are only due to the code changes between

RTTOV-11 and RTTOV-12. These plots give confidence that the computation of Jacobians between the two versions of the model has not changed significantly.

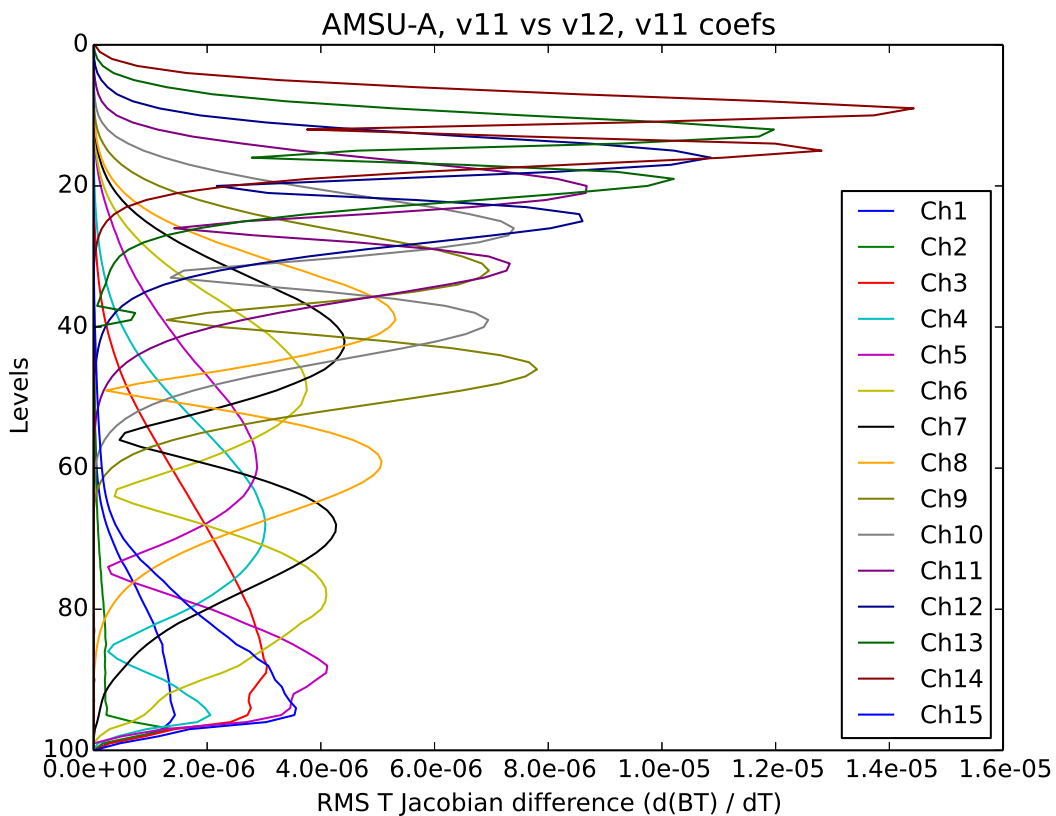


Figure 41. Comparison of differences in AMSU-A temperature jacobians for v11 and v12 coefficients using v7 predictors. This is for a 50 degree zenith angle and 0.6 surface emissivity.

#### 4. Summary

The latest version of RTTOV, RTTOV-12 has been validated in several ways to show the same or improved performance for the prediction of satellite top of atmosphere radiances both for clear air, cloudy, aerosol and precipitating profiles. It builds on previous versions of RTTOV. The changes have been validated as described in this document and the references given. Referring to the list of changes made between RTTOV-11 and RTTOV-12 given in section 2 the following comments can be made:

- Improvements to infrared and microwave line-by-line models and associated spectroscopic datasets from which the RTTOV coefficients are computed

|   |   |   |   |
|---|---|---|---|
| <p>The EUMETSAT<br/>Network of<br/>Satellite Application<br/>Facilities</p> |  | <h2 style="text-align: center;">RTTOV-12 Science and<br/>Validation Report</h2> | <p>Doc ID : NWPSAF-MO-TV-41<br/>Version : 1.0<br/>Date : 16/02/2017</p> |
|---|---|---|---|

*Updating to the latest line-by-line model using the most recent spectroscopic databases will reduce the forward model biases with observations originating from the radiative transfer calculations.*

- Inclusion of a new more accurate discrete ordinates scattering option for visible/near-infrared and infrared wavelengths

*This enhances the capabilities of RTTOV to more accurately compute scattering from clouds and aerosols at visible/near-infrared and infrared wavelengths although the computations are not as fast as for the pre-existing fast parameterisations for IR/MW scattering. The solvers used for solar and thermal (emitted) infrared radiation can be selected independently.*

- Improvements to ice cloud scattering

*The modelling of ice cloud has been improved with the latest optical properties databases.*

- New infrared surface emissivity and reflectance model over the ocean and updated atlas over land

*The sea surface reflectance model has also been updated. Over land the new CAMEL atlas has been added with improved values from ASTER.*

- New microwave surface emissivity model over ocean and updated atlases over land which now includes snow and sea-ice and extends the frequency range to 700GHz.

*The ocean surface emissivity uses FASTEM-6 with small changes made to better treat the relative wind direction. The TESSEM2 model has also been included now which extends the frequency range up to 700GHz. Over land the emissivity atlas (TELSEM) has been updated to extend to higher frequencies (700GHz). There is also the option of using the updated CNRM microwave emissivity atlas.*

- Addition of SO<sub>2</sub> as a new variable gas

*One more active trace gas has been added to RTTOV which is SO<sub>2</sub> for use with high resolution sounders to allow a retrieval of total column SO<sub>2</sub>.*

- Allow user to specify cloud/aerosol concentration units for input

*This gives users more flexibility on the units of the values they are inputting to RTTOV for cloud and aerosol concentrations*

- Improved model for non-LTE effects for advanced IR sounders

*This provides more accurate day time shortwave infrared (around 4.3µm) simulations by taking into account the non-LTE effects on the absorption lines in the stratosphere.*

|   |   |   |   |
|---|---|---|---|
| <p>The EUMETSAT<br/>Network of<br/>Satellite Application<br/>Facilities</p> |  | <p>RTTOV-12 Science and<br/>Validation Report</p> | <p>Doc ID : NWPSAF-MO-TV-41<br/>Version : 1.0<br/>Date : 16/02/2017</p> |
|---|---|---|---|

- Improved treatment of Zeeman effect for high peaking SSMIS channels  
*More accurate modelling of the Zeeman effect splitting the strong oxygen lines by the Earth's magnetic field for high peaking channels used by SSMIS has been introduced with specially computed coefficients.*
- Capability to simulate the pressure modulator radiometer  
*Coefficients for the NIMBUS-6 PMR instrument are now available.*
- Updates to the PC-RTTOV model  
*PC-RTTOV has been upgraded to allow simulations over all surface types and to incorporate the non-LTE effects described above.*
- Addition of capability to call the HT-FRTC model  
*A new fast radiative transfer model is being made available for use with RTTOV-12, HT-FRTC, which uses the principal components approach to rapidly compute a spectrum. This is mainly of interest for the advanced IR sounders with many channels. Users will be able to try out this new tool for their applications.*

## 5. Acknowledgements

The RTTOV-12 developments and validation described here were carried out as part of the EUMETSAT funded NWP-SAF activities by the Met Office, ECMWF and MétéoFrance. In addition contributions from several scientists, visiting and associate scientists are gratefully acknowledged. They are Eva Borbas (CIMSS/UW), Catherine Prigent (CNRS), Ben Ruston (NRL), Fabrizio Baordo (BoM) and Richard Larsson (Lulea Inst. Technology).

|  |  |   |  |
|--|--|---|--|
|  |  | <b>RTTOV-12 Science and Validation Report</b> | Doc ID : NWPSAF-MO-TV-41<br>Version : 1.0<br>Date : 16/02/2017 |
|--|--|---|--|

## 6. References

Baran, A. J., P. N. Francis, L.-C. Labonnote, and M. Doutriaux-Boucher 2001: A scattering phase function for ice cloud: Tests of applicability using aircraft and satellite multi-angle multi-wavelength radiance measurements of cirrus, *Q.J.Roy. Meteorol. Soc.*, **127**, 2395–2416.

Baran, A. J., Cotton, R., Furtado, K., Havemann, S., Labonnote, L.-C., Marengo, F., Smith, A. and Thelen, J.-C. 2014: A self-consistent scattering model for cirrus. II: The high and low frequencies. *Q.J.Roy. Meteorol. Soc.*, **140**: 1039–1057. doi:10.1002/qj.2193

Baum, B. A., P. Yang, A. J. Heymsfield, C. Schmitt, Y. Xie, A. Bansemer, Y. X. Hu, and Z. Zhang, 2011: Improvements to shortwave bulk scattering and absorption models for the remote sensing of ice clouds. *J. Appl. Meteor. Clim.*, **50**, 1037-1056.

Beagley, S.R., Boone, C.D., Fomichev V.I., Jin J.J., Semeniuk K., McConnell J.C. and Bernath P.F. 2010: First multi-year occultation observations of CO<sub>2</sub> in the MLT by ACE satellite: observations and analysis using the extended CMAM. *Atmos. Chem. Phys.* **10**, 1133–1153.

Borbas, E and Ruston B.C. 2010. `The RTTOV UWiremis IR land surface emissivity module,` *Report NWPSAF-MO-VS-042, 24pp.*

Borbas, E, 2014: Investigation into the angular dependence of IR surface emissivity. *Visiting Scientist Report. EUMETSAT NWPSAF-MO-VS-050.* [https://nwpsaf.eu/vs\\_reports/nwpsaf-mo-vs-050.pdf](https://nwpsaf.eu/vs_reports/nwpsaf-mo-vs-050.pdf)

Borbas E.E, G.Hulley, M. Feltz, B. Knuteson and S. Hook, 2017a: MEaSURES Unified and Coherent Land Surface Temperature and Emissivity (LST&E) Earth System Data Record (ESDR) for Earth Science: The Combined ASTER and MODIS Emissivity database over Land (CAMEL) *Algorithm Theoretical Basis Document, V001, not publicly available yet*

Borbas E.E, G.Hulley, M. Feltz, B. Knuteson and S. Hook, 2017b:MEaSURES Unified and Coherent Land Surface Temperature and Emissivity (LST&E) Earth System Data Record (ESDR) for Earth Science: The Combined ASTER and MODIS Emissivity database over Land (CAMEL), *Users guide V001, not publicly available yet*

Chandrasekhar, S. 1960: Radiative Transfer (*Dover, New York*).

Clark, R.N., Swayze, G.A., Wise, R., Livo, E., Hoefen, T., Kokaly, R., Sutley, S.J., 2007: USGS digital spectral library splib06a: *U.S. Geological Survey, Digital Data Series 231*, <http://speclab.cr.usgs.gov/spectral.lib06>

Cox, C. and W. Munk, 1954: Measurements of the roughness of the sea surface from photographs of the sun's glitter, *J. Opt. Soc. Am.* **44**, 838-850.

Curtis, P., J. Houghton, G. Peskett, and C. Rodgers 1973: Remote sounding of atmospheric temperature from satellites. The pressure modulator radiometer for Nimbus F. *Proc. R. Soc London A*, **337**, 135-150.

|   |   |   |   |
|---|---|---|---|
| <p>The EUMETSAT<br/>Network of<br/>Satellite Application<br/>Facilities</p> |  | <p>RTTOV-12 Science and<br/>Validation Report</p> | <p>Doc ID : NWPSAF-MO-TV-41<br/>Version : 1.0<br/>Date : 16/02/2017</p> |
|---|---|---|---|

DeSouza-Machado, S.G., Strow, L.L., Hannon, S.E., Motteler, H., Lopez-Puertas, M., Funke, B. and Edwards, D.P. 2006: Fast Forward Radiative Transfer Modeling of 4.3 um Non-Local Thermodynamic Equilibrium effects for the Aqua/AIRS Infrared Temperature Sounder, *Geophysical Review Letters*, **34**, L01802, doi:10.1029/2006GL026684.

Ebuchi, N. and S. Kizu, 2002: Probability distribution of surface wave slope derived using sun glitter images from geostationary meteorological satellite and surface vector winds from scatterometers, *J. Oceanography* **58**, 477-486

Eyre J.R. and H.M. Woolf 1988: Transmittance of atmospheric gases in the microwave region: a fast model. *Applied Optics* **27** 3244-3249

Eyre J.R. 1991: A fast radiative transfer model for satellite sounding systems. *ECMWF Research Dept. Tech. Memo.* **176** Available at [http://www.ecmwf.int/publications/library/ecpublications/\\_pdf/tm/001-300/tm176.pdf](http://www.ecmwf.int/publications/library/ecpublications/_pdf/tm/001-300/tm176.pdf)

Friedman, D., 1969: Infrared characteristics of ocean water (1.5-15µm), *Appl. Opt.* **8**, 2073-2078.

Funke, B., López-Puertas, M., García-Comas, M., Kaufmann, M., Höpfner, M., and Stiller G.P. 2012: GRANADA: A Generic RAdiative traNsfEr AnD non-LTE population algorithm, *J. Quant. Spectrosc. Radiat. Transfer*, **113(14)**, 1771-1817.

Funke, B. and López-Puertas, M. 2015:, *personal communication*.

Garcia R.R., Lopez-Puertas M., Funke B., Marsh D.R., Kinnison D.E., Smith A.K. and Gonzalez-Galindo F. 2014:, 'On the distribution of CO<sub>2</sub> and CO in the mesosphere and lower thermosphere', *JGR Atmospheres*, **10.1002/2013JD021208**.

Hale, G. M. and M. R. Querry, 1973: Optical constants of water in the 200nm to 200µm wavelength region, *Appl. Opt.* **12**, 555-563.

Han, Y. 2007:, 'Incorporation of the JCSDA Zeeman RT model in RTTOV-9', *NWP SAF Visiting Scientist Report*, available from the Met Office.

Hess M., P. Koepke, and I. Schult (1998) Optical Properties of Aerosols and Clouds: The Software Package OPAC. *Bull. Amer. Meteor. Soc.*, **79**, 831–844, doi:10.1175/1520-0477(1998)079<0831:OPOAAC>2.0.CO;2

Hocking, J., 2015: A visible/infrared multiple-scattering model for RTTOV. *NWP SAF report*. [http://nwpsaf.eu/publications/tech\\_reports/nwpsaf-mo-tr-031.pdf](http://nwpsaf.eu/publications/tech_reports/nwpsaf-mo-tr-031.pdf)

Jacobson M. Z. 2005: Fundamentals of atmospheric modelling, *Cambridge Eds*.

Jurado-Navarro, Á. A., López-Puertas, M., Funke, B., García-Comas, B., Gardini, A., Stiller, G.P. and Clarmann, T.V. 2015: Vibrational-vibrational and vibrational-thermal energy transfers of CO<sub>2</sub> with N<sub>2</sub> from MIPAS high-resolution limb spectra. *J. Geophys. Res. Atmos.*, **120**, 8002–8022. doi: 10.1002/2015JD023429.

|   |   |   |   |
|---|---|---|---|
| <p>The EUMETSAT<br/>Network of<br/>Satellite Application<br/>Facilities</p> |  | <h2 style="text-align: center;">RTTOV-12 Science and<br/>Validation Report</h2> | <p>Doc ID : NWPSAF-MO-TV-41<br/>Version : 1.0<br/>Date : 16/02/2017</p> |
|---|---|---|---|

Karbou, F., E.G rard, and F. Rabier, 2006: Microwave land emissivity and skin temperature for AMSU-A and -B assimilation over land, *Q.J.R. Meteorol. Soc.* **132**, No. 620, Part A, pp. 2333-2355(23), doi :10.1256/qj.05.216

Karbou, F., E. G rard, and F. Rabier, 2010: Global 4DVAR assimilation and forecast experiments using AMSU observations over land. Part I: Impacts of various land surface emissivity parameterizations. *Wea. Forecasting*, **25**, 5–19.

Kazumori, M., and S.J. English 2015: Use of the ocean surface wind direction signal in microwave radiance assimilation. *Q.J. Roy. Meteorol. Soc.* **141**, 1354-1375.

Liebe H.J., Rosenkranz P.W. and Hufford G.A. 1992: Atmospheric 60 GHz oxygen spectrum: new laboratory measurements and line parameters, *J.Quant.Spectrosc.Radiat.Transfer* **48**, 629-643.

Masuda, K., T. Takashima, and Y. Takayama, 1988: Emissivity of pure and sea waters for the model sea surface in the infrared window regions, *Remote Sens. Environ.* **24**, 313-329.

Masuda, K., 2006: Infrared sea surface emissivity including multiple reflection effect for isotropic Gaussian slope distribution model, *Remote Sens. Environ.* **103**, 488-496.

Matricardi, M., 2003: RTIASI-4, a new version of the ECMWF fast radiative transfer model for the infrared atmospheric sounding interferometer. *ECMWF Tech. Memo* **425**.

Matricardi, M., Chevallier F, Kelly G, Thepaut J-N 2004: An improved general fast radiative transfer model for the assimilation of radiance observations. *Q. J. Roy. Meteorol. Soc.* **130** 153-173

Matricardi, M. 2005: The inclusion of aerosols and clouds in RTIASI, the ECMWF fast radiative transfer model for the infrared atmospheric sounding interferometer. *ECMWF Tech. Memo.* **474**.

Matricardi M. 2008: The generation of RTTOV regression coefficients for IASI and AIRS using a new profile training set and a new line-by-line database. *ECMWF Tech. Memo.* **564**.

Matricardi M. 2010: A principal component based version of the RTTOV fast radiative transfer model. *Q. J. Roy. Meteorol. Soc.* **136** 1823-1835.

Matricardi, M. and A.P. MacNally 2014: The direct assimilation of principal components of IASI spectra in the ECMWF 4D-VAR and the generation of RTTOV and PC\_RTTOV new regression coefficients for AIRS, IASI, and IASI-NG. *Contract report n EUM/CO/07/460000475/PS*

Matricardi, M., M. L pez Puertas and B. Funke 2017: Modeling of nonlocal thermodynamic equilibrium effects in the principal component based version of the RTTOV fast radiative transfer model. *Submitted to J. Geophys Res.*

McNally A.P., Watts P.D. 2003: A cloud detection algorithm for high-spectral-resolution infrared sounders. *Q. J. Roy. Meteorol. Soc.*, **129** 3144-3423.

Meissner, T. and F. J. Wentz. 2012: The emissivity of the ocean surface between 6 and 90 GHz over a large range of wind speeds and earth incidence angles. *IEEE Transactions on Geoscience and Remote Sensing* **50**, no. 8 (2012): 3004-3026.

|  |  |   |  |
|--|--|---|--|
|  |  | <h2>RTTOV-12 Science and Validation Report</h2> | Doc ID : NWPSAF-MO-TV-41<br>Version : 1.0<br>Date : 16/02/2017 |
|--|--|---|--|

Newman, S. M., J. A. Smith, M. D. Glew, S. M. Rogers, and J. P. Taylor, 2005: Temperature and salinity dependence of sea surface emissivity in the thermal infrared, *Q. J. R. Meteorol. Soc.* **131**, 2539-2557.

Payne, V.H., Delamere J.S., Cady-Pereira K.E., Gamache R.R., Moncet J-L, Mlawer E.J and Clough S. 2008: 'Air-broadened half-widths of the 22 GHz and 183 GHz water vapour lines', *IEEE TGRS* **46**, 3601-3617.

Pinkley, L. W. and Williams, D., 1976: Optical properties of sea water in the infrared, *J. Opt. Soc. Am.* **66**, 554-558.

Prigent, C., Aires, F., Wang, D., Fox, S. and Harlow, C., 2016: Sea surface emissivity parameterization from microwaves to millimeter waves. *Q.J.Roy. Meteorol. Soc. Accepted Author Manuscript. doi:10.1002/qj.2953.*

Rayer, P.J. 2017: RTTOV coefficients for PMR. *Satellite Applications Working Paper available on request from the NWP SAF.*

Rosenkranz P.W. and Staelin D.H. 1988: Polarized thermal microwave emission from oxygen in the mesosphere, *Radio Science* **23**, 721-729.

R7REP2002 RTTOV-7 science and validation report available at:  
[http://nwpsaf.eu/oldsite/deliverables/rm/rttov7\\_svr.pdf](http://nwpsaf.eu/oldsite/deliverables/rm/rttov7_svr.pdf)

R8REP2006 RTTOV-8 science and validation report available at:  
[http://nwpsaf.eu/oldsite/deliverables/rm/rttov8\\_svr.pdf](http://nwpsaf.eu/oldsite/deliverables/rm/rttov8_svr.pdf)

R9REP2008 RTTOV-9 science and validation report available at:  
[http://nwpsaf.eu/oldsite/deliverables/rm/rttov9\\_files/rttov9\\_svr.pdf](http://nwpsaf.eu/oldsite/deliverables/rm/rttov9_files/rttov9_svr.pdf)

R10REP2010 RTTOV-10 science and validation report available at:  
[http://nwpsaf.eu/oldsite/deliverables/rm/docs\\_rttov10/rttov10\\_svr\\_1.11.pdf](http://nwpsaf.eu/oldsite/deliverables/rm/docs_rttov10/rttov10_svr_1.11.pdf)

R11REP2013 RTTOV-11 science and validation report available at:  
[http://nwpsaf.eu/deliverables/rm/docs\\_rttov11/rttov11\\_svr.pdf](http://nwpsaf.eu/deliverables/rm/docs_rttov11/rttov11_svr.pdf)

Saunders R.W., M. Matricardi and P. Brunel 1999a: A fast radiative transfer model for assimilation of satellite radiance observations - RTTOV-5. *ECMWF Research Dept. Tech. Memo.* **282** (available from <http://www.ecmwf.int/publications/library/do/references/list/14> ).

Saunders R.W., M. Matricardi and P. Brunel 1999b: An Improved Fast Radiative Transfer Model for Assimilation of Satellite Radiance Observations. *Q. J. Roy. Meteorol. Soc.* , **125**, 1407-1425.

Scheck, L., 2016: Comparison of MFASIS and RTTOV-DOM. *NWP SAF report.*  
[http://nwpsaf.eu/vs\\_reports/nwpsaf-mo-vs-054.pdf](http://nwpsaf.eu/vs_reports/nwpsaf-mo-vs-054.pdf)

Sherlock, V., 1999: ISEM-6: Infrared surface emissivity model for RTTOV6. *Forecasting Research Technical Report No.299, Met. Office NWP Division United Kingdom*, 17 pp

|   |   |   |   |
|---|---|---|---|
| <p>The EUMETSAT<br/>Network of<br/>Satellite Application<br/>Facilities</p> |  | <p>RTTOV-12 Science and<br/>Validation Report</p> | <p>Doc ID : NWPSAF-MO-TV-41<br/>Version : 1.0<br/>Date : 16/02/2017</p> |
|---|---|---|---|

Stamnes, K., S.-C. Tsay, W. Wiscombe and K. Jayaweera, 1988: Numerically stable algorithm for discrete-ordinate-method radiative transfer in multiple-scattering and emitting layered media. *Applied Optics*, **27**, 2502-2509.

Tretyakov M. Yu., Koshelev M.A., Dorovskikh V.V., Makarov D.S. and Rosenkranz P.W. 2005: 60 GHz oxygen band: precise broadening and central frequencies of fine structure lines, absolute absorption profile at atmospheric pressure, and revision of mixing coefficients, *J.Mol.Spectrosc.* **231**, 1-14.

U.S. Standard Atmosphere, 1976: *U.S. Government Printing Office, Washington, D.C., 1976*

Vidot, J., A. J. Baran, and P. Brunel 2015: A new ice cloud parameterization for infrared radiative transfer simulation of cloudy radiances: Evaluation and optimization with IIR observations and ice cloud profile retrieval products. *J. Geophys. Res. Atmos.*, **120**, 6937–6951. doi: [10.1002/2015JD023462](https://doi.org/10.1002/2015JD023462).

Wang, D., C. Prigent, L. Kilic, S. Fox, R. C. Harlow, C. Jimenez, F. Aires, C. Grassotti, and F. Karbou, 2016: Surface emissivity at microwaves to millimeter waves over Polar Regions: parameterization and evaluation with aircraft experiments. *Submitted to J. Atmos. Oceanic. Tech.*

Wu, X. and W.L. Smith, 1997: Emissivity of rough sea surface for 8-13 $\mu$ m: modeling and validation, *Appl. Opt.* **36**, 1-11

## End of Report